1-1-2016

Fe3o4 Nanoparticles For Magnetic Hyperthermia And Drug Delivery: Synthesis, Characterization And Cellular Studies

Maheshika Palihawadana Arachchige
Wayne State University,

Fe_3O_4 NANOPARTICLES FOR MAGNETIC HYPERTHERMIA AND DRUG DELIVERY; SYNTHESIS, CHARACTERIZATION AND CELLULAR STUDIES

by

MAHESHIKA PALIHAWADANA ARACHCHIGE

DISSERTATION

Submitted to the Graduate School

of Wayne State University,

Detroit, Michigan

in partial fulfillment of the requirements

for the degree of

DOCTOR OF PHILOSOPHY

2016

MAJOR: PHYSICS

Approved By:

Advisor	Date
Advisor	Date

DEDICATION

To

My parents,

Husband Lalith and Son Maleesh

ACKNOWLEDGEMENTS

This thesis and the related research work were made possible by the guidance and assistance of a group of remarkable people during my time at the Wayne State University. First and foremost, I'm truly grateful to my former advisor Dr. Gavin Lawes, for all his invaluable support during the early part of my PhD career (August. 2010 – Dec. 2013). Secondly, I am deeply thankful to Dr. Ratna Naik, my current advisor, for her constant guidance during the final years of my doctoral studies. After the untimely death of Dr. Lawes, she encouraged me, guided me to finish my work for the successful completion of the degree. I'm also grateful to Prof. Bhanu P. Jena (from Physiology), my co-advisor, for his constant encouragement and suggestions that helped me in completion of my thesis work. Special thanks go to Dr. Stephanie Brock from Chemistry, our research collaborator and also my external committee member for her support and guidance. I would also like to express my sincere gratitude Dr. Vaman Naik for his guidance on both the experimental work and data analysis towards the completion of my thesis. I would like thank Prof. Boris Nadgorny for his support and advice as my dissertation committee members, as well as allowing me to use the facilities in his labs for some of the sample preparations and characterization.

I'd also like to thank Prof. Jo Wadehra his guidance as a Graduate advisor throughout the PhD program. My teachers at WSU Physics, Drs. Paul Keyes, J. J. Chang, Caroline Morgan, William Rolnick, Ashis Mukhopadhay and Zhixian Zhou who taught me the fundamentals of physics and its related disciplines deserve a special mention.

I am deeply grateful to Dr. Rajesh Regmi and Dr. Ambesh Dixit who helped me immensely in learning new techniques and adapting to new instruments when I started out my research in the lab. I am also thankful to Drs. Indika Wanniarachchi, Akila Kumarasiri, Suneetha

Devpura and Punya Talagala for their support in both the professional and personal level from the first day in Wayne State University. I would also like to thank all my colleagues at Wayne State University, including Drs. Suvra Laha, Kulwinder Dhindsa, Rupam Mukherjee and Hemeshkar Nemala who have graduated recently as well as my current colleagues, Ehab and Ajay for all their valuable support over the last few years.

I am immensely grateful to my parents for all their support, encouragement and unconditional love. They were always there looking out for me regardless of the situation. I am deeply thankful to my husband, Lalith, who has been my strength, encouraging me at every step of this journey. This achievement would not have been possible without the sacrifices made by him and my loving son, Maleesh. Finally I would like to express my sincere gratitude to all my friends and family members for their support throughout this journey.

TABLE OF CONTENTS

LIST OF TABLES

LIST OF FIGURES

CHAPTER 1 INTRODUCTION

1.1: Nanotechnology and Magnetic Nanoparticles

Nanotechnology is an emerging field of science, which includes the study of materials with size ranging from few nanometers to several hundred nanometers and their applications to various fields. Nanomaterials are of great scientific interest as they are effectively a bridge between bulk materials and atomic or molecular structures and interestingly, the properties of materials can change as their size approaches the nanoscale. In recent years, nanoparticles have attracted a great deal of attention due their potential applications in biomedicine [1-5]. Among nanoparticles for such use, magnetic nanoparticles have the potential to be delivered to a specific region in the body with an external magnetic field manipulation. This requires large magnetization for the magnetic nanoparticles so that they respond to externally applied magnetic field at physiological temperatures. Iron oxide nanoparticles (Fe_3O_4), with relatively higher saturation magnetization values are therefore suitable for this purpose. Furthermore, low toxicity, biocompatibility, surface functionalization capabilities combined with excellent magnetic resonance imaging (MRI) contrast property make them ideal for use in noninvasive disease targeting, detection, and treatment. Therefore, superparamagnetic Fe_3O_4 nanoparticles are currently used as one of the most important and acceptable candidates for magnetic resonance imaging (MRI) [6-8],targeted drug delivery [9-11], magnetic hyperthermia [12-14], and cell separation [15,16].Nanoparticles have higher surface energy due to their smaller sizes hence tend to form agglomerates which is not favorable for their use in clinical applications. Therefore, these nanoparticles are often coated with a surfactant making them a stable colloidal suspension which is called a “Ferrofluid”.

1.2: Magnetic Hyperthermia

Over the past decade, the topic of “cancer therapy” has attracted a great deal of attention due to the huge impact it has on human life. The principle of cancer treatment is to kill the malignant cells with the least of damage to normal cells. Distinguishing cancer cells from normal cells is difficult, making the existing treatments such as chemotherapy and radiation therapy less effective and fraught with various side effects Hyperthermia or heating therapy has great potential as a complimentary cancer treatment method. It is known that the blood flow in tumor is lower and the reduced blood flow causes the lack of oxygen which leads to the formation of lactic acid making the cells more acidic [17]. The acidic cells which are more sensitive to temperature, have lower thermal resistance than normal cells and the decreased blood flow in the tumor limit their ability to dissipate heat. As a result, cancer cells can be damaged and killed by increasing the local temperature to the range of 42 ºC to 46 ºC with little detriment to healthy cells. Depending on the nature of the heating source and the heated target, hyperthermia is categorized into 3 types: local, regional, and whole body hyperthermia [18] .Whole body hyperthermia is used only when the disease has spread throughout the body and can be achieved using hot wax, hot air, hot water suits, or infrared radiation. Regional hyperthermia where heat is subjected to a smaller area such as a whole tissue or organ is accomplished by utilizing ultrasound, radio frequency (RF) fields, or microwaves. Local hyperthermia involves heating a small area of interest such as a tumor. Different approaches for inducing hyperthermia as discussed above are illustrated in the Figure 1.1. The effectiveness of the treatment is judged by how much of the tumor is heated to a therapeutic level and often this is very low due to lack of heat transfer to the tumor site.

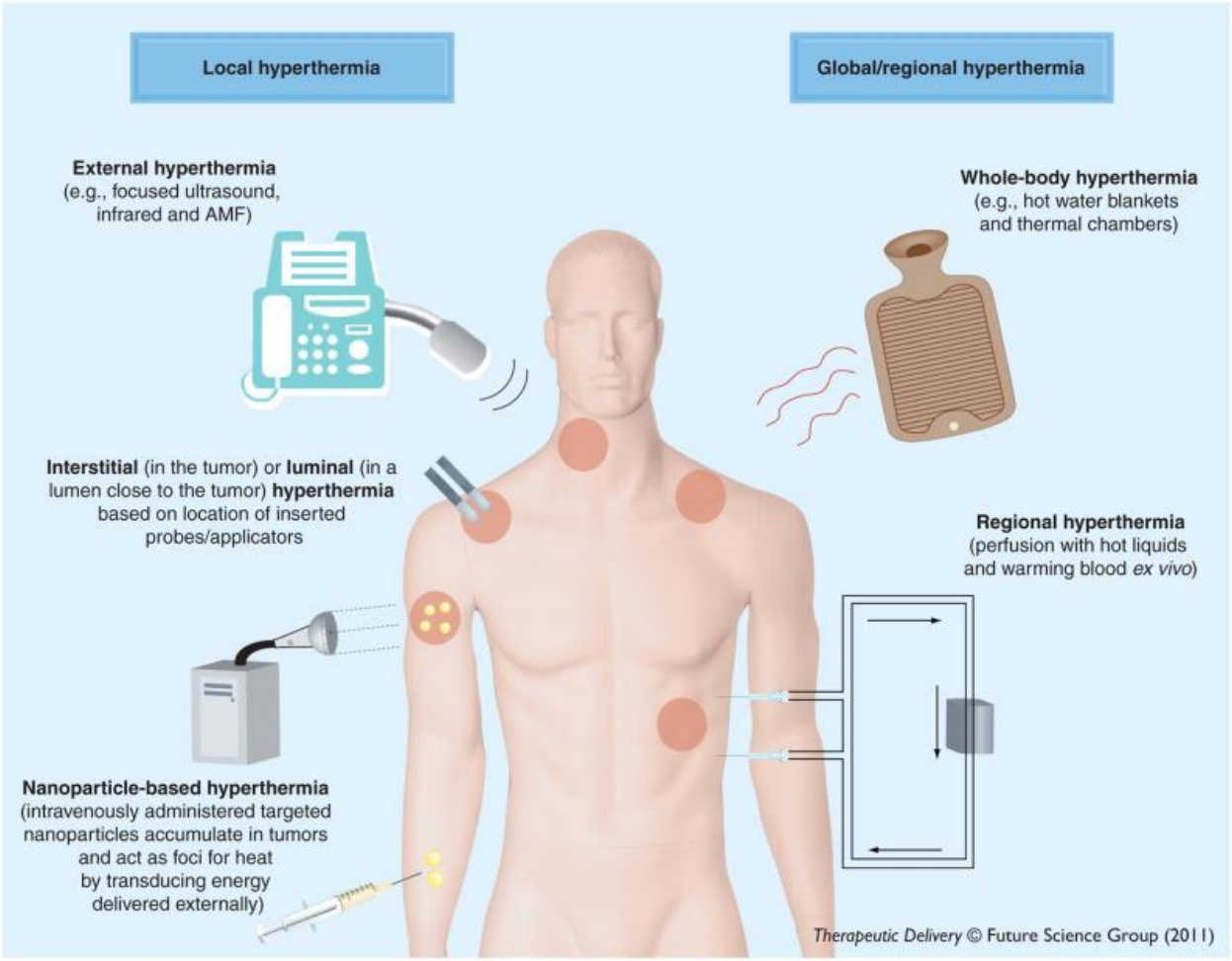

Figure 1.1: Methods of achieving hyperthermia for cancer treatment [19].

Various nanoparticles have been used as heat mediators in local hyperthermia technique. The most common types of nanoparticles which have been investigated for hyperthermia therapy are listed in Table 1.1.

The idea of utilizing magnetic nanoparticles for hyperthermia was first proposed by Gilchrist et al. in 1950s and since then many types of nanoparticles show promising results [19]. Magnetic hyperthermia, where electromagnetic energy is converted into heat by applying an external alternating magnetic field on magnetic nanoparticles, is of particular interest as the nanoparticles can be guided and localized specifically at a tumor site by external magnetic field

guidance and can also be directed to the cancer cells by tagging a targeting ligand such as antibody or peptide, without reducing its efficiency [20,21]. For example, Fabio et al. have reported that conjugation of folate receptors enhances the targeting for magnetic hyperthermia in solid tumors [22].

Table 1.1: Commonly studied nanoparticles for hyperthermia

Meterial	**Structure**	**Hyperthermia type**
Au	Nanorods [23,24], Nanoshells [25,26]	Photothermal heating (NIR)
Carbon	Nanotubes (CNT) [27-30], Graphene oxide sheets[31]	Photothermal heating (NIR)
Quantum dots (CdTe, dSe)	[32,33]	Photothermal heating (Radiofrequency)
Fe_3O_4	Nanosheres [34-36] Nanocubes [37-39], Coreshell [40,41]	Magnetic heating

Magnetite (Fe_3O_4) and maghemite (γ-Fe_2O_3) have been extensively studied and are promising candidates due to their biocompatibility and relative ease to functionalize. Figure 1.2 illustrates an example of strategy for using magnetic nanoparticles as a potential Theranostic (Diagnostic + Theraputic) agent. Recent studies have reported the heating efficiencies in Fe_3O_4/γ-Fe_2O_3 core-shell structures as well [42]. Additionally, iron oxide nanoparticles doped with other magnetic dopants such as Co, Mn and Ni [43-45] are under investigation to achieve a high heating efficiency by tuning the magnetic anisotropy and saturation magnetization of the material. However, among numerous complications, with a high curie temperature of Fe_3O_4 -850K and γ-Fe_2O_3- 750 K, overheating is one of the drawbacks of utilizing these nanoparticles and as a

solution for those complex magnetic oxides with low Curie temperature are being investigated [46-48].

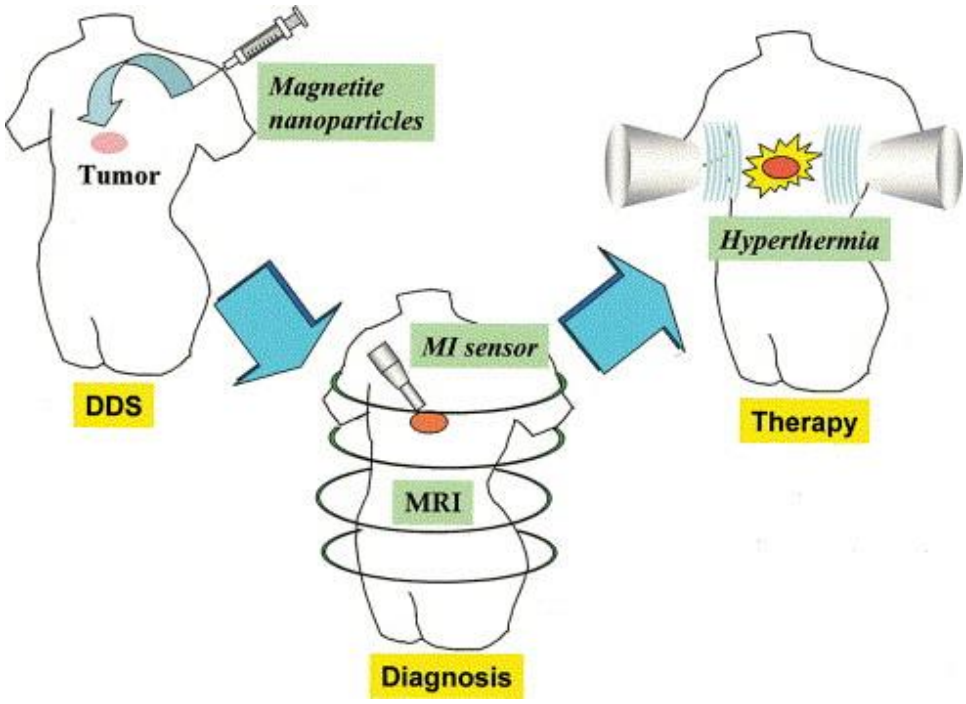

Figure 1.2: Schematic illustration of the therapeutic strategy using magnetic particles. Functionalized magnetic nanoparticles accumulate in the tumor tissues via the drug delivery system (DDS). Magnetic nanoparticles can be used as a tool for cancer diagnosis by magnetic resonance imaging (MRI) or for magnetoimpedance (MI) sensor. Hyperthermia can then be induced by AMF exposure [49].

1.3: Magnetic nanoparticles based drug delivery

Over the last two decades, magnetic nanoparticles have been increasingly exploited as platforms for transport of drugs and genes [50,51]. In magnetic drug delivery, a drug or therapeutic reagent is conjugated to the nanoparticle and introduced in the body, and concentrated in the target area by means of a magnetic field gradient (using an internally implanted permanent magnet or an externally applied field) [52]. Using a targeting ligand the targeting specificity can be enhanced. These anti-cancer drugs carried by the nanoparticles can then be released at the tumor site via enzymatic activity, or via changes in the physiological

conditions such as temperature and pH. Drug release can also be magnetically triggered from the drug-conjugated magnetic nanoparticles [52-54]. For example, Hayashi et al [55] reports a study done on superparamagnetic iron oxide nanoparticles conjugated with folic acid (well-known as a targeting ligand for breast cancer cells), β-Cyclodextrin (which act as drug container)and tamoxifen (anti-cancer drug). By means of an AC magnetic field, heat is generated which triggers drug release - a behavior that is controlled by switching the high frequency magnetic field on and off. This is capable of performing drug delivery and hyperthermia simultaneously. Among various other anti-cancer drugs doxorubicin is widely used as a model drug. There are several methods that can be used to load doxorubicin into nanoparticles such as by adsorption on the nanocarrier inorganic core [56-58], by diffusion [59,60] or entrapment [61,62] in the coating materials and by chemical bonds [63,64] with the coating of the nanocarrier. Even though magnetic drug delivery shows a great promise in cancer treatment avoiding the side effects of conventional chemotherapy, the designing and fabrication of an efficient nanoparticle based drug delivery system is still a challenge.

1.4: Surface modification of magnetic nanoparticles

Nanoparticles have larger surface to volume ratio and hence possess high surface energies. Moreover magnetic nanoparticles which are of interest for biomedical applications such as magnetite (Fe_3O_4) have hydrophobic surfaces. Therefore, these particles tend to aggregates forming large clusters resulting in increased particle size and in addition, exhibit high chemical activity which causes them to easily oxidize in air (especially magnetite)generally resulting in loss of magnetism and dispersibility. Therefore, providing a proper surface coating to keep the stability of the nanoparticles is crucial. Additionally, in order to expand the scope of biological application of nanoparticles, some molecules/surfactants are also employed to enhance its

biocompatibility. The stable colloidal suspensions of surfactant coated iron oxides nanoparticles are called “Ferrofluids” which are magnetizable fluids that remain as liquids in the most intense magnetic fields and in biological media. Stabilization of the ferrofluid can be achieved by the presence of one or both of the two repulsive forces (see Fig. 1.3): electrostatic and steric repulsion between the particles [51]. The steric force is difficult to predict or quantify and mostly depend on the weight and the density of the polymer used for the coating. The electrostatic repulsion can be understood through the knowledge of the diffusion potential and mainly depends on the ionic strength and the pH of the solution.

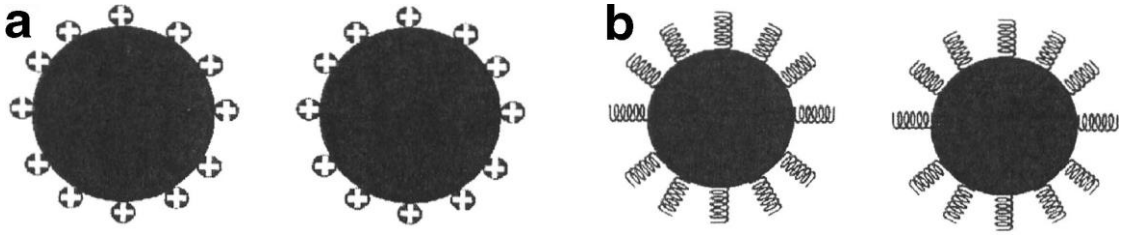

Figure 1.3: (a) Particles stabilized by the electrostatic layer and (b) Particles stabilized by steric repulsion [51].

Over the years, researchers have developed various surface modification strategies comprised of grafting of or coating with both organic and inorganic materials. In addition to the stabilization, these protecting shells also provide a platform for further functionalization depending on the desired application. The coating process can be done during the nanoparticles synthesis referred to as “in situ” coating or can be done after the nanoparticle synthesis referred as “post-synthesis”. Organic molecules include small organic molecules, macromolecules or polymer and biological molecules. They provide various highly reactive functional groups such as carboxyl groups, aldehyde groups and amino groups. Moreover, organic compounds

functionalized nanoparticles preserve the basic magnetism characteristics of magnetic nanoparticles as well as possess good biocompatibility and biodegradability.

Based on their surface characteristics functionalized nanoparticles can be divided into three main types; water soluble, oil-soluble, and amphiphilic. Nanoparticles with surfaces containing hydrophobic group, such as the fatty acid, alkyl phenol are referred to as oil-soluble. Examples for such surfactants are oleic acid, myristic acid, lauric acid, hexadecylphosphonic acid, dihexadecylphosphonic acid etc [65,66]. Nanoparticles with chemical groups which are hydrophilic on the surface are called water-soluble and some examples are citric acid [67],amino acid [68]. Amphiphilic type refers to the nanoparticles with surfaces containing both hydrophilic and hydrophobic chemical groups, such as cyclodextrin [69], sulfuric lycine [70] which make the functionalized nanoparticles both oil-soluble and water-soluble. Polymer coated nanoparticles are also of great interest for their use in biomedical applications. Polymer coating materials can be classified into synthetic and natural and some commonly used polymers are listed in Table 1.2 along with their advantages.

Table 1.2: Commonly studied Organic polymers and their advantages.

Polymer		**Advantages and applications**	**References**
Natural	Dextran	Stability, Biocompatibility, Enables optimum polar interactions with iron oxide surfaces, Enhances the blood circulation time.	[15,76-80],
	Starch	Improves the biocompatibility, good for MRI, and drug target delivery	[81,82]
	Chitosan	Biocompatible and hydrophilic large abundance in nature, biocompatibility, and ease of functionalization. widely used as non-viral gene delivery system	[83-86]
Synthetic	Poly(ethyleneglycol) (PEG)	Enhance the hydrophilicity and water-solubility, improves the biocompatibility, blood circulation times and internalization	[87-89]

		efficiency of the nanoparticles. Used in target-specific cell labeling, Magnetic hyperthermia, targeted drug delivery	
	Alginate	Improves the stability and biocompatibility. Used in drug delivery applications.	[90-92]
	Poly-N-isopropylacrylamide (PNIPAM)	Generally used as thermosensitive drug delivery and cell separation	[93-96]
	Polyethyleneimine (PEI)	Ability to complex with DNA, guide intracellular trafficking of their cargo into the nucleus, used for gene delivery cell transfection with either DNA or siRNA nucleotides.	[97-100]

Also depending on the properties and the structure, coating arrangement of polymers on the surface of nanoparticles can be different as well (Fig. 1.4).

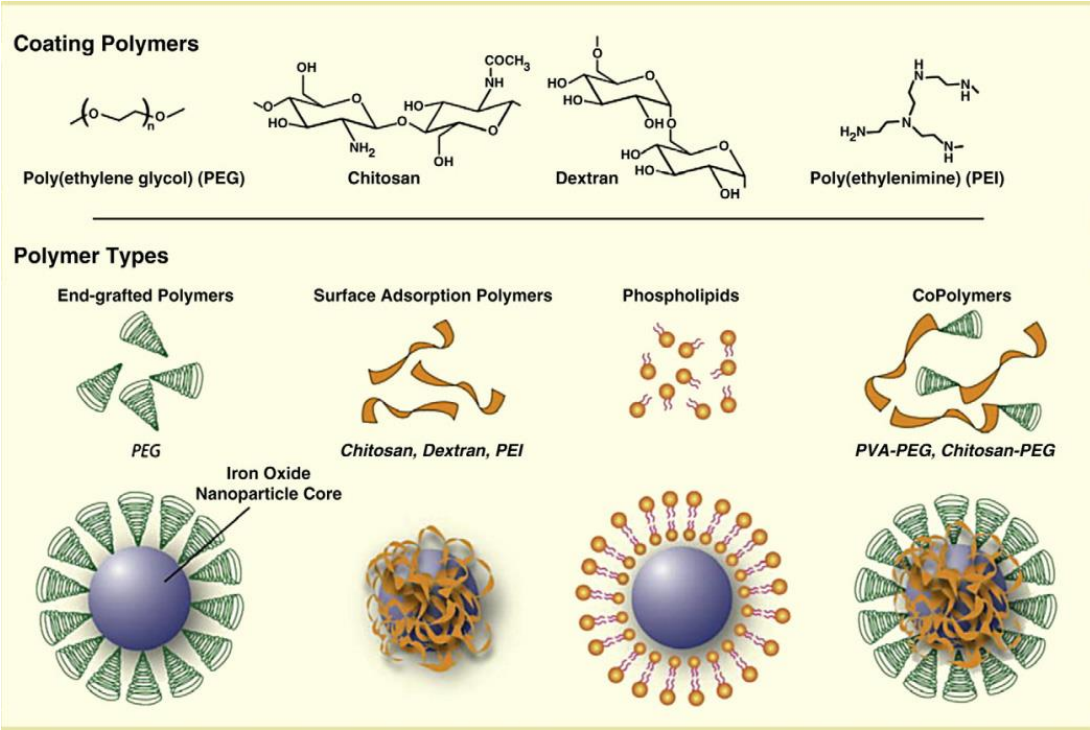

Figure 1.4 : Illustration depicting the assembly of polymers onto the surface of magnetic nanoparticle cores [75].

Depending on the desired application, these nanoparticle can be further modified by functionalizing them with various biological molecules such as antibodies, proteins, targeting ligands, etc. [71-74].These may be bound to the polymer surfaces of the nanoparticles directly or indirectly by chemically coupling via some functional end groups such as amide or ester bonds to make the particles target specific. Inorganic materials are used for surface coating of the nanoparticles, mainly iron oxide nanoparticles. These inorganic materials include silica [101-104], metal or nonmetals [105-108] (gold, silver, platinum, palladium, iron, carbon), and metal oxides (Al_2O_3) or metal sulfides. The coating with inorganic materials produces "core-shell" structure with the nanoparticle core and coating shell. These coatings not only provide stability to the nanoparticles in solution but also help in binding various biological ligands to the nanoparticle surface. The surface modified magnetic nanoparticles which are stabilized against clustering and sedimentation, with enhanced biocompatibility can be further modified such as the addition of specific targeting ligands, dyes or therapeutic agents providing the particles a wide ranging potential in the biomedical area. Among these various surface modification possibilities the right choice of functionalization should be carefully chosen to obtain a desired structure suitable for the intended application.

1.5: Scope of the thesis

This thesis includes the synthesis characterization and two major applications of superparamagnetic Fe_3O_4 nanoparticles in the field of biomedicine; magnetic hyperthermia and drug delivery. Based on the experimental data and analysis on Fe_3O_4 nanoparticles, we are able to determine the effect of particle size, polydispersity, anisotropy and dipolar interactions on the temperature dependent SAR, qualitatively and quantitatively. The cellular studies done on human pancreatic cancer cells include the cytotoxicity, time dependent cellular uptake and

distribution of Dextran coated Fe_3O_4 nanoparticles. A novel drug-dye –nanoparticle conjugation was designed and fabricated and its cellular entry and time dependent drug release were investigated as well. Chapter 2 describes the detailed background on nanoparticle magnetism and magnetic hyperthermia, and their relation to linear response theory. It also provides theoretical framework used to analyze and interpret the experimental data. Chapter 3 describes various synthesis methods and functionalization strategies and introduces the working principles of the key characterization techniques used throughout this research. In Chapter 4, the results of our investigation on the effect of magnetic dipolar interactions and size distribution of Fe_3O_4 nanoparticles on temperature dependent magnetic hyperthermia of ferrofluids are discussed. Chapter 5 explores the effect of Gd-doping and Chapter 6 on the effect of biocompatible coating of Fe_3O_4 nanoparticles with dextran and citric acid on magnetic and temperature dependent magnetic hyperthermia properties. Chapter 7 describes our study on time dependent cellular uptake and intracellular distribution of dextran coated Fe_3O_4 nanoparticles functionalized with fluorescent dye, FITC. Chapter 8 describes our study on the dual conjugation of doxorubicin and FITC on dextran coated Fe_3O_4 nanoparticles and its cellular internalization and drug release. The summary and prospects for future study are described in Chapter 9.

CHAPTER 2 MAGNETIC NANOPARTICLES AND MAGNETIC HYPERTHERMIA

2.1: Magnetism in materials

The origin of magnetism in materials is due to both spin and orbital angular momentum of electrons in atoms/ions/molecules and interactions between them. The magnetic property of a material is described by a quantity called "magnetization" (M), defined as net magnetic dipole moment per unit volume of the material. The magnetic response of a material to an external magnetic field (H) is further defined by *Magnetic Susceptibility*,

$$\chi = \Delta M/\Delta H \quad \textbf{(2.1)}$$

In the absence of any magnetic ordering, magnetic materials can be divided into two categories; diamagnetics with small and negative χ (-10^{-6} to -10^{-3}) and paramagnetic with small positive χ (10^{-6} - 10^{-1}). Diamagnetism occurs when the atom has completely filled shells leading to a zero orbital angular momentum and zero spin. When an external field is applied, it alters the electron kinetic energy and thus their angular momentum. This leads to a net magnetic moment opposite to the applied field, while the spin remains zero. On the other hand, in a paramagnetic material, atoms have a permanent magnetic moment due to the net spin from the unpaired electrons. In the absence of external magnetic field H, all the magnetic moments are aligned randomly in different directions due to thermal fluctuation, resulting in a net zero magnetic moment. However, when an external magnetic field is applied, there will be anon-zero net magnetic moment, but returns to zero upon the removal of the external magnetic field. The temperature dependent behavior of paramagnetic susceptibility is explained using the Curie-Weiss law [109].

Below a critical temperature, even in the absence of an external field, magnetic materials can develop long range magnetic order due to exchange coupling of spins (a quantum

mechanical effect) leading to a non-zero net magnetization. There are three types of basic magnetic ordering namely, ferromagnetic, antiferromagnetic, and ferrimagnetic. Figure 2.1 shows the three simplest types of magnetic ordering. The critical temperature below which this long range order presents is known as the Curie temperature (for ferromagnets) or Neel temperature (for antiferromagnets and ferrimagnets).

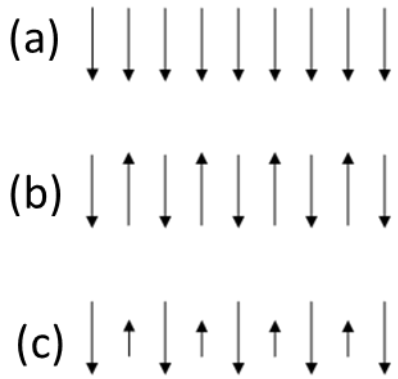

Figure 2.1: Arrangements of moments in magnetic systems (a) Ferromagnetic ordering (b) Antiferromagnetic ordering (c) Ferrimagnetic ordering

It is well known that a bulk ferromagnetic material is composed of magnetic domains, regions in which all of the local spins are aligned parallel to each other, due to exchange coupling. The formation of magnetic domains is a result of balancing several energy terms: the exchange energy which tries to align all the magnetic moment along the same direction, the magnetocrystalline energy which arises from spin-orbit coupling and energetically favors alignment of the moments along specific direction, and the magnetostatic energy. The direction of the ferromagnetic spin alignment varies from one domain to another, and is randomly oriented in samples cooled through the transition temperature in zero fields so that the net magnetization is zero or small. The different domains in a ferromagnet are separated by domain walls in which the magnetization rotates from one direction to another. Magnetic behavior of bulk ferromagnetic materials is governed by the dynamics of these domains. Unlike the paramagnets,

ferromagnets will not relax back to zero magnetization upon removal of the external magnetic field since the domain wall motion process is not reversible which is known as “hysteresis”. One characterizes this *M-H* curve using three parameters; the saturation magnetization (M_s), the coercivity (H_c) and the remnant magnetization (M_r) (Figure 2.2).

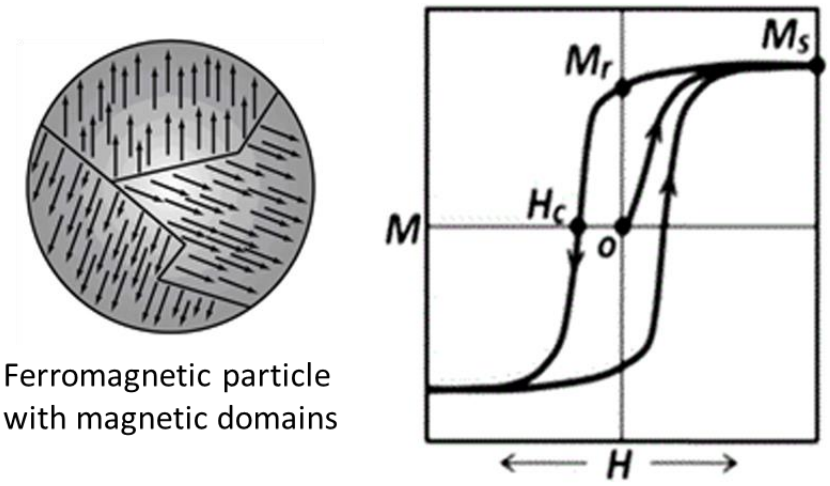

Figure 2.2: M-H curve for a collection of ferromagnetic particles showing hysteresis

2.2: Magnetic nanoparticles and superparamagnetism

As mentioned in chapter 1, magnetic nanoparticles refer to materials with size ranging from few nanometers to several hundred nanometers which are ferromagnetic or ferrimagnetic in its solid bulk form. As the particle size decreases below a critical value, the formation of domain walls become energetically unfavorable and particles become single domain particles in which all the spins are aligned, called “superspins” with a large magnetic moment (~ 10,000 Bohr Magneton) on each particle. At temperatures above a characteristic temperature, T_B, called Blocking temperature (described in Section 2.2.1), the moments on individual nanoparticles will tend to align an external applied field, similar to a paramagnetic material, but with a large magnetization. Figure 2.3 shows magnetic behavior of a collection of such nanoparticles under

an external magnetic field, without any hysteresis. This phenomenon is called "superparamagnetism" and is important to understand the magnetic behavior of nanoparticles.

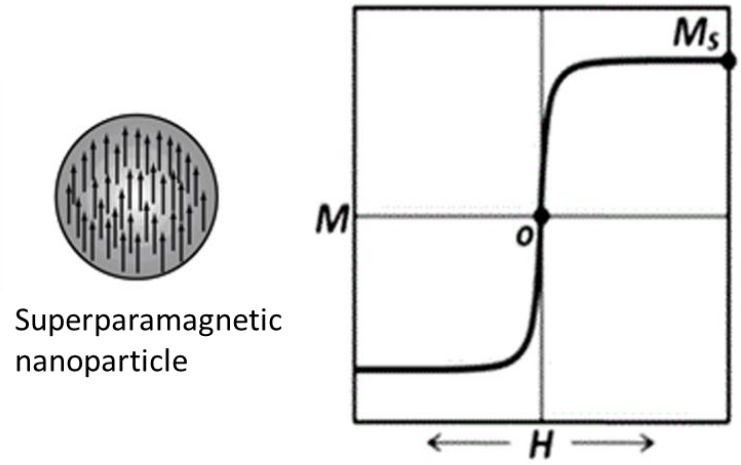

Figure 2.3: M-H curve for a collection of superparamagnetic nanoparticles

For an assembly of non-interacting superparamagnetic particles, the magnetization (M) as a function of applied magnetic field (H) is explained by the Langevin function,

$$L(x) = \coth x - \frac{1}{x} \qquad \textbf{.2)}$$

where $x=M_sVH/k_BT$, M_s is the saturation magnetization and V is the volume of the particle given by $V=\pi D^3/6$ in terms of diameter of the particle (D). When the particle size distribution is taken into account the magnetization can be written as,

$$M(H) = M_s \frac{\int_0^\infty f(D)VL(x)dD}{\int_0^\infty f(D)VdD} \qquad \textbf{(2.3)}$$

where *f*(D) if the log-normal distribution given by,

$$f(D) = \frac{1}{\sqrt{2\pi}\sigma D} \exp\left\{ - \frac{\left[\ln\left(\frac{D}{D_0} \right) \right]^2}{2\sigma^2} \right\} \quad \textbf{(2.4)}$$

Here, D_o is the most probable particle diameter and σ is the width of the distribution.

2.2.1: Magnetic Anisotropy in Nanoparticles

The magnetic properties of an ensemble of single domain particles are determined by the thermal energy and the magnetic anisotropy of the particle. In bulk magnetic materials, usually there is an energetically favorable direction along which the magnetic moments are typically aligned, referred to as the easy axis. The difference in magnetic energy to produce saturation in a hard direction is called the anisotropy energy. The most common types of anisotropy that affects the magnetic behavior of the material are magnetocrystalline anisotropy, surface anisotropy, shape anisotropy, exchange anisotropy, and induced anisotropy (for example, by stress) [110]. In nanoparticles, shape, surface and magneto crystalline anisotropies are the most important. Shape anisotropy arises from the long range dipolar interactions within the particle and causes magnetization to depend on the shape of the sample. For an example, in long thin needle shaped particles, it is easier to magnetize along its long axis compared with that along any of its short axes. A perfectly spherical nanoparticle having symmetry along all possible directions will have no shape anisotropy. As the size of the nanoparticle decreases, the surface to the volume ratio is increased and the surface effects become more significant. Therefore surface magnetic anisotropy is expected to contribute to the total magnetic anisotropy and the effective anisotropy is given by the following expression [111];

$$K = K_V + \frac{6K_S}{D} \quad \textbf{(2.5)}$$

Where, K_V is the magnetocystalline anisotropy constant of the core, K_S is the surface anisotropy energy constant, and D is the size of spherical particles.

Magnetocrystalline anisotropy arises from the symmetry of the lattice, the shape of the electron orbitals and from spin-orbit coupling. The actual direction of the magnetization can be either of two opposite directions along the easy axis. More precisely, this represents "uniaxial anisotropy", but this is normally sufficient for understanding the magnetic response of nanoparticles. The magneto-crystalline anisotropy (E) is given by,

$$E_\theta = KVSin^2(\theta) \quad \textbf{(2.6)}$$

where, K is the uniaxial anisotropy energy density and V is the volume of the particle and θ is the angle between the magnetization and the easy axis. As the particle size is reduced, the anisotropy energy decreases. In sufficiently small particles, thermal energy K_BT is comparable or larger than the anisotropy energy. If the thermal energy K_BT is large compared to the anisotropy energy, the direction of the nanoparticle moment can flip freely between the two directions defined by the easy axis. Magnetic moments are randomly oriented leading to a zero net magnetization behaving as a superparamagnetic system. The relaxation time (τ), which is the average time it takes the magnetic moment to jump from one minimum to the other is given by the Neel-Brown relation:

$$\tau = \tau_0 \exp\left(\frac{KV}{k_BT}\right) \quad \textbf{(2.7)}$$

In this equation, $\tau_0$is a microscopic time scale for the transitions, which are typically taken to be 10^{-9}-10^{-13} s, k_B is the Boltzmann's constant and T is the temperature. As the thermal energy of the particle is reduced by lowering the temperature, the fluctuations slow down and the relaxation time increases.

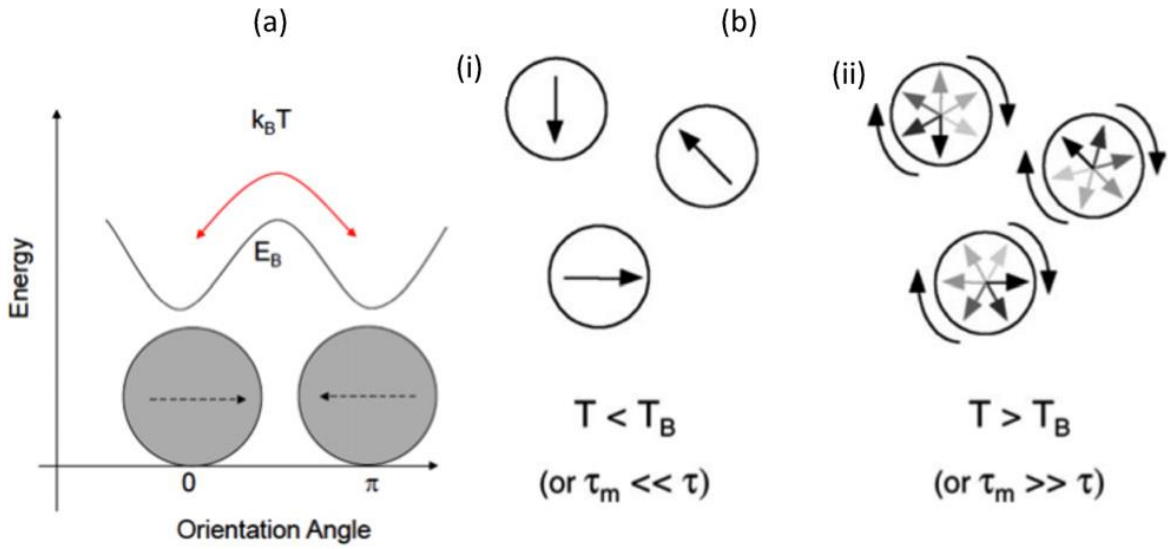

Figure 2.4: (a) Energy barrier between two easy axes in a magnetic nanoparticle (b) (i) at temperatures below the T_B of the particles, the net moments are quasi-static. (b) (ii). At temperature well above T_B, the moment reversals are so rapid that the net magnetic moment is zero [112].

The critical temperature, at which the relaxation time matches with the experimental measuring time,τ, is known as the blocking temperature (T_B) and is a characteristic of the particle. The value of τ_m is given by the type of the measurement being performed. It is typically of the order of 10^2 seconds for DC measurements and 10^{-1}–10^{-5}s for AC susceptibility measurements. At the blocking temperature,

$$T_B \approx KV/k_B \, ln(\tau_m/\tau_0) \quad \textbf{(2.8)}$$

Below this blocking temperature the spins are frozen over the timescale of each measurement. Above the blocking temperature, the moments possess enough energy to flip and particles behave like simple paramagnets. The above ideas are illustrated in Figure 2.4. By measuring the temperature dependent DC magnetization of the material, the T_B can be estimated to determine the magnetic anisotropy constant, K.

2.3: Magnetic dipolar interactions

Magnetic dipole interaction between two magnetic dipoles $\overrightarrow{\mu 1}$ and $\overrightarrow{\mu 2}$separated by a distance $\vec{r}$ is described as,

$$E_d = \frac{\mu_0}{4\pi r^3}\left[\overrightarrow{\mu_1}.\overrightarrow{\mu_2} - \frac{3}{2}(\overrightarrow{\mu_1}.\vec{r})(\overrightarrow{\mu_2}.\vec{r})\right] \quad \textbf{(2.9)}$$

where μ_0 is the permeability of free space. The atoms in a crystal have magnetic moment of a few Bohr magnetons. Therefore magnetic dipole interactions between atoms are very small and have a negligible influence on the magnetic ordering at finite temperatures compared to exchange interactions which are responsible for magnetic ordering in materials. However, ferromagnetic/ferrimaagnetic nanoparticles with dimensions around 10 nm can have magnetic moments as large as 10,000 Bohr magnetons, and therefore, dipole interactions between nanoparticles can have a significant influence on the magnetic properties. In a sample of randomly distributed nanoparticles having an average magnetic moment μ the dipole interaction energy of a particle can be written as, $E_d \approx \frac{\mu_0 \mu^2}{4\pi r^3}$ [113] .

Over the past years, there are many studies that report the effect of dipolar interactions on the magnetic properties of nanoparticles. For example, Vargas et al [114]investigated the effect of dipolar interactions on magnetic properties of Fe based nanoparticles by tuning the strength of interactions by changing the concentrations of the particles. It is clearly shown that for increasing the particle concentration, the maximum of the ZFC curve shift to higher temperatures, indicating an increase in the blocking temperature, T_B. A similar trend has been observed in many reported studies [115,116]. Dormann et al [115], analyzed the frequency dependence of the blocking temperature for a series of ɤ-Fe_2O_3 nanoparticles with different strengths of inter-particle interactions. He suggests that interparticle interactions simply lead to a progressive increase of the energy barrier. The model suggested by Dormann is based on a statistical

calculation of the dipolar energy for a collection of disordered particles with a non-zero size distribution and easy directions in random orientation. The interparticle interactions are described by an energy term, E_{int} with uniaxial symmetry hence added to the anisotropy energy for the particle alone. This leads to an increase in magnetocrystalline energy barrier, E_B, and the modified relaxation time is given by,

$$\tau_N = \tau_0 \exp\left[\frac{E_B + E_{int}}{K_B T}\right] \quad \textbf{(2.10)}$$

This model has been used to explain the similar results observed in other studies such as Fe particles embedded in an alumina matrix [117], γ-Fe_2O_3 particles dispersed in a polymer [116], magnetite particles dispersed in dispersed in calcium silicate glasses [118] and as well as Ni NPs embedded in an amorphous SiO2/Cmatrix [119].The same observation, the increased relaxation time with increasing dipolar interactions, is explained by different approach in the study reported by Landi et al. [120].He defines an effective energy barrier based on a random mean field approximation. The dipolar interactions produced by an ensemble of particles are interpreted as random field acting on a reference particle resulting in a new term in the free energy of the reference particle, expressed as a cumulant expansion of the random field, carried up to fourth-order. In this model, the dipolar interactions increase the effective anisotropy barrier rather than inciting some degree of order into the system.

In addition to above models, there are other studies that employ Langevin function for better understanding of the role of dipolar interactions on the magnetic properties of nanoparticles. This theory, known as T^* model, is proposed by Allia et al. [121] in his study on Granular Cu-Co alloys. He considers the particle moments to be interacting through long range dipolar random forces and pictures the effects in terms of a temperature T^* added to the actual temperature T in the denominator of the Langevin function argument which explains all features

of the experimental M(H) curves. His argument is justified as follows; the direction, sign, and magnitude of the dipolar field acting on any magnetic moment randomly changes at a sufficiently high rate which enhance the disorder of magnetic moments. This exerted disorder opposes the ordering effect of the external magnetic field which is similar to the role played by the temperature and hence strengthens its effects. The apparent temperature is written as $T_a=T+T^*$, T^* is not an arbitrary quantity, but is related to the rms dipolar energy ε_D through the relation, $\varepsilon_D = kT^*$.The experimental magnetization M, with modified Langevin function can now be written as,

$$M(H) = M_S \frac{\int_0^\infty f(D)VL\left(\frac{M_S VH}{K_B\left(T+T^*\right)}\right)dD}{\int_0^\infty f(D)VdD} \qquad \textbf{(2.11)}$$

By fitting the experimental magnetization data to the above expression, an estimation of the strength of dipolar interaction can be obtained. Even though this model explains the complex, collective effects of dipolar interactions in a simplified, but effective way, this has some limits which are addressed as well by the authors. Firstly, the ‘‘interaction’’ temperature T^* may be much higher, larger than the measurement temperature. According to the authors, the T^* obtained by best-fit procedure reflects not only changes in the spatial distribution of particles or in their degree of correlation, but also the presence of additional interactions among particles such as indirect interactions of RKKY type which are presence in metallic granular systems. When T increases towards T_c, T^* drops, vanishing when $T=T_c$. On cooling, the T^* becomes stronger, to finally become dominant without changing the functional form of the M (H) curve. When the temperature is lowered towards the blocked regime, the moments are expected to be frozen in random directions. Therefore, the argument of dynamic disorder provided by

interactions is no longer valid in the blocked regime. But as long as the measurements are taken at superparamagnetic regime, this model provides adequate understanding of the effects of dipolar interactions.

2.4. Magnetic hyperthermia and linear response theory

The cyclic increase of internal energy of a magnetic system in adiabatic process is equal to the magnetic work done on the system and can be expressed as [122]:

$$\Delta U = -\mu_0 \oint M dH \quad \textbf{.12)}$$

where M is the magnetization and μ_0 is the permeability of free space and *H* is magnetic field intensity. The power dissipation in the magnetic system during several cycles is equal to the internal energy multiplied by the frequency, $P = Uf$. As described by Rosensweig [122], the response of a magnetic system to an alternating external applied magnetic field , $H(t) = H_0 cos(\omega t)$, where ω is the angular frequency and H_0 is the amplitude of the field, can be explained as follows. The magnetic susceptibility, χ_{ac}, which describes the full dynamic response of a system to an external stimulus, can be written in terms of real and imaginary parts,

$$\chi_{ac} = \chi' - i\chi'' \quad \textbf{(2.13)}$$

Therefore, the resulting magnetization, M (t) is,

$$\mathrm{M(t)} = \mathrm{Re}\left(\chi_{ac} H_0 e^{i\omega t}\right) = H_0(\chi' \cos \omega t + \chi'' \sin \omega t) \quad \textbf{(2.14)}$$

Substituting M and H in Eq.1.14 yields,

$$\Delta U = 2\mu_0 H_0^2 \chi'' \int_0^{\frac{2\pi}{\omega}} sin^2\, \omega t\, dt \quad \textbf{(2.15)}$$

Integrating the above equation and multiplying the result by the cyclic frequency f =ω/2π gives the power dissipation,

$$P = \mu_0 \pi \chi'' f H_0^2 \quad \textbf{(2.16)}$$

The frequency dependence of the complex susceptibility is given by the following expression.

$$\chi = \frac{\chi_0}{1+i\omega\tau} \tag{2.17}$$

The real and imaginary parts of the susceptibility can therefore be expressed as:

$$\chi' = \frac{\chi_0}{1+(\omega\tau)^2} \tag{2.18}$$

$$\chi'' = \frac{\omega\tau}{1+(\omega\tau)^2}\,\chi_0 \tag{2.19}$$

Here χ_0 is the equilibrium susceptibility, which is expressed as,

$$\chi_0 = \chi_i\left(\coth\xi - \frac{1}{\xi}\right) \tag{2.20}$$

where $\chi_i = (\mu_0 \Phi M_d^2 V_m)/3k_BT$,initial susceptibility , $\xi = (\mu_0 M_d H_0 V_m)/k_BT$ with M_d, the domain magnetization of the nanoparticle, and Φ is the volume fraction of the magnetic nanoparticles in the ferrofluid. Under the influence of an external alternating magnetic field, nanoparticles generate heat due to relaxation losses (Neel and Brownian relaxations) and hysteresis losses. In superparamagnetic particles, with negligible /zero coercivity, the contribution from the latter is not significant at all and the relaxation losses are the prominent mechanisms. The relaxation mechanisms are illustrated in Figure 2.5.

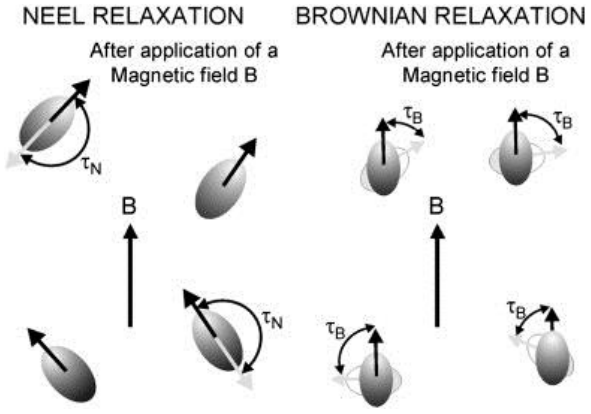

Figure 2.5: Left: Neel relaxation showing the rotation of magnetic moment (white arrow). Right: Brownian relaxation where the physical rotation of the nanoparticle takes place to align the moments along the magnetic field [36].

In case of the Brownian relaxation, heating of the particles in liquid suspension occurs due to viscous drag between the particles and liquid, where the entire particle physically rotate to align the magnetic moment with the applied field. The Brownian relaxation time is given by the equation 2.22,

$$\tau_B = \frac{4\pi\eta R_H^3}{k_B T} \tag{2.21}$$

Here η is the viscosity of the suspension and R_H is the hydrodynamic radius of the surfactant coated nanoparticle. For Neel relaxation, the moments of the particles fluctuate with the applied field and the relaxation time is given by the following equation.

$$\tau_N = \frac{\sqrt{\pi}}{2}\tau_0 \exp\left(\frac{KV}{k_B T}\right)\sqrt{\frac{KV}{k_B T}} \tag{2.22}$$

Since the Brownian and Neel processes take place in parallel, the combined relaxation of the particle is characterized by the effective relaxation time τ_{eff} ,defined as: $1/\tau_{eff} = (1/\tau_N) + (1/\tau_B)$.

By substituting the Eq 2.19 in the power dissipation expression given by Eq. 2.16, and taking the polydispersity of the particles into account by incorporating the log normal distribution given by Eq.2.4, the temperature dependent power dissipation in the sample can be expressed as,

$$P(T) = \int_0^\infty \frac{\mu_0 \chi_0 H_0^2 \omega}{2} \frac{\omega\tau_{eff}}{1+(\omega\tau_{eff})^2} f(D)d(D) \tag{2.23}$$

Depending on the value of $\omega\tau$, two regime can be identified; the high frequency limit in which $\omega\tau \gg 1$ and the low frequency limit where $\omega\tau \ll 1$.In high frequency limit Eq 2.24 reduces to the following expression which clearly shows that at higher frequencies the generated power is independent of the frequency ω.

$$P = \mu_0 H_0^2 \chi \frac{1}{2\tau} \tag{.24}$$

On the other hand, in the low frequency limit where $\omega\tau << 1$, the power is proportional to the square of the frequency as shown below.

$$P = \mu_0 H_0^2 \chi \frac{\omega^2 \tau}{2} \quad \textbf{(2.25)}$$

The linear response theory described above assumes the magnetic response of the system to be linear with the applied magnetic field. To be more specific this theory is valid in the superparamagnetic regime where $H_0 < k_B T / \mu_0 M_s V$.

Finally, in order to incorporate the dipolar interactions in this model, we replaced the temperature term *T* in in the above equations with the apparent temperature *(T+T*)*, as done in the analysis of M-H data using Langevin model.

CHAPTER 3 SYNTHESIS AND CHARACTERIZATION METHODS OF MAGNETIC NANOPARTICLES

3.1: Synthesis of Fe_3O_4 nanoparticles

Over the past years many research works have been done to develop efficient synthesis approaches to produce the size/shape controlled, stable, biocompatible, and monodispersed iron oxide nanoparticles (NPs) [123-126]. The most common methods include co-precipitation [51,127], thermal decomposition [128], hydrothermal synthesis [129,130], microemulsion [131] and sonochemical [106] synthesis. The most conventional method for obtaining Fe_3O_4 or ɤ-Fe_2O_3 is by co-precipitation which consists of mixing ferric and ferrous salts in highly basic solutions at room temperature or at elevated temperature. The size and shape of the iron oxide nanoparticles depends on the type and amount of salt used (Fe^{2+}:Fe^{3+} ratio), the reaction temperature, the pH value, ionic strength of the media, and the other reaction parameters such as stirring rate, dropping speed of basic solution. Co-precipitation method results in the production of water-soluble magnetic nanoparticles and is relatively cost-effective compared to other synthesis techniques. However, this method leads to nanoparticles with wide particle size distribution due to lack of control over hydrolysis reactions of the iron precursors and the nucleation and growth steps causing a wide range of their blocking temperatures. Thermal decomposition technique, decomposition of organo-metallic iron precursors at higher temperatures in organic solvents, involves complicated operation and generates high quality monodisperse particles because of separate nucleation and growth processes. But the resulting nanoparticles are hydrophobic and thus cannot be directly used for bio-applications. In order to make them water soluble, laborious post-synthesis ligand exchange procedures are necessary, which may result in aggregation and loss of magnetic properties. The other common, recently developed, method is hydrothermal synthesis which generates nanoparticles with excellent

crystallinity with controllable size and shape in aqueous phase. The properties of the nanoparticles can vary with the synthesis method due to the differences in cationic distribution and vacancies, spin canting, or surface contribution.

For the synthesis of nanoparticles studied in this thesis work, chemical co-precipitation and hydrothermal method were used as standard methods of synthesis because of the simplicity, and ability to produce superparamagnetic iron oxide nanoparticles of reasonable size (10-15 nm). Moreover, these techniques are compatible with different approaches we are using for functionalizing the nanoparticles.

3.1.1: Co-precipitation synthesis

The reagent precursor chemicals, $FeCl_2 \cdot 4H_2O$ and $FeCl_3 \cdot 6H_2O$ were obtained from Merck and were used without further purification. Aqueous solutions of $FeCl_2.4H_2O$ and $FeCl_3.6H_2O$ were mixed in 1:2 molar ratios. For a typical synthesis, 5.4 g of $FeCl_3.6H_2O$ in 20 mL of 2 M HCl was mixed with 2.0 g of $FeCl_2.4H_2O$ in 5 mL of 2 M HCl in a 1 L beaker. After stirring the mixture with magnetic stirrer for about 5 min, 250 mL of 1 M NH_4OH was added dropwise into the mixture under constant magnetic stirring, which resulted in a brown precipitate that became black eventually upon the formation of Fe_3O_4 nanoparticles (Figure 3.1).

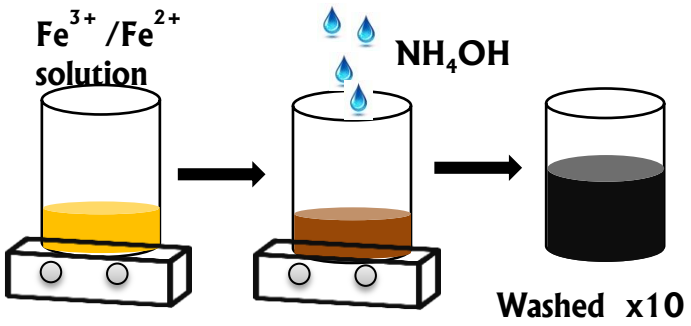

Figure 3.1: Synthesis of Fe_3O_4 nanoparticles by chemical co-precipitation technique.

The chemical reaction may be written as follows;

$$Fe^{2+} + 2Fe^{3+} + 8\mathrm{OH}^{-} \rightarrow Fe_3O_4 + 4H_2O + 8HCl$$

The nanoparticles were stirred for another 10 minutes, isolated with a magnet and washed several times with deionized water until a neutral pH was reached which was confirmed by a litmus paper.

The particle size of the nanoparticles obtained from the co-precipitation method can be varied in the range of 6-13 nm by changing the different experimental parameters such as the RPM rate, rate of adding the base to the reaction mixture, concentrations of the salts and the base etc. For example, using 2 M NH_4OH added rapidly to the reaction mixture under 1000 rpm of stirring rate resulted in generating nanoparticles of 6-7 nm size whereas using 1 M NH_4OH added dropwise to the reaction mixture under a stirring rate of 350rpm produces 11-12 sized nanoparticles.

3.1.2: Hydrothermal synthesis

The Hydrothermal synthesis of Fe_3O_4 nanoparticles was carried out by precipitating $FeCl_2.4H_2O$ and $FeCl_3.6H_2O$ (1:2 molar ratio) in alkaline medium (NH_4OH) followed by the hydrothermal treatment. 2.0 g of $FeCl_2.4H_2O$ and 5.4 g of $FeCl_3.6H_2O$ were mixed in 50 ml of 2M HCl solution 10 ml of NH_4OH solution was then added dropwise into the mixture under constant magnetic stirring. After 10 minutes of stirring, the mixture, which contains the precipitated black product, was immediately added into a Teflon-lined stainless steel autoclave with 60 ml capacity and subsequently placed in a furnace at 134 °C for 1 h. The autoclave was cooled naturally after the hydrothermal treatment and the precipitate was recovered and washed several times with DI water by means of a magnet.

After the synthesis of the nanoparticles they were washed to remove the excess ions which resulted in wet slurry. Several portions of the slurry were then used to quantify the amount

of iron oxide in each gram of the slurry. This estimation was used to determine the concentration of the prepared ferrofluid. This method of calibration at the beginning of the preparation of the ferrofluid, provides an accurate method of reporting the concentration of the ferrofluid with a narrow window of uncertainty.

3.2: Surface functionalization of Fe_3O_4 nanoparticles

In our research, we used dextran, a natural polysaccharide, and citric acid for the preparation of ferrofluid. Both the materials have different moieties which allow us the further functionalization with anti-cancer drugs, dyes and targeting ligands. Dextran has the hydroxyl groups which could be attached to the amine group or concerted into carboxyl groups whereas citric acid contains carboxyl groups providing many possibilities of functionalization.

3.2.1: Dextran coated Fe_3O_4 nanoparticles

In order to coat the Fe_3O_4 nanoparticles with dextran, synthesized nanoparticles (from the wet slurry)and 60-90 kDa dextran (1:1 wt.) were dispersed in 25 ml of 0.5 M NaOH separately. The dextran solution was kept under sonicating and the iron oxide nanoparticles solution was added drop wise into the dextran solution over 30 minutes period. The resulting mixture was sonicated for 24 hours to get the well suspended ferrofluid which was stable over 6 month's period.

3.2.2: Citric acid (CA) coated Fe_3O_4 nanoparticles

Citric acid stabilized nanoparticles were prepared by direct addition method [132]. Simply, 5ml of 0.1mg/ml citric acid solution was added to 0.5g of Fe_3O_4 nanoparticles dispersed in 20ml of 0.5 M NaOH solution. The mixture was heated to 90 ºC and stirred for 60 minutes. After that the solution was cooled down to room temperature and was dialyzed using 8-10 kDa cutoff membrane to remove excess citric acid.

3.2.3:Cross-linking of Fe_3O_4 nanoparticles

Cross-linking of Dextran coated Fe_3O_4 nanoparticles, which endows a greater stability of nanoparticles, was carried out using an established published procedure [80]. Dextran coated Fe_3O_4 were cross-linked using epichlorohydrin (ECH). The solution containing 1 ml of dextran coated Fe_3O_4 nanoparticles; 5 ml of 5 M NaOH, 2 ml of DI water and 2 ml of ECH was prepared. The mixture was incubated at room temperature with continuous shaking to promote the interaction between aqueous and organic phase. After 24 hours of incubation, the black colloidal suspension was dialyzed several times against DI water to remove the excessive ECH and ions.

3.2.4: FITC functionalized Fe_3O_4 nanoparticles

Fluoro isothiocyanate (FITC) is a widely used fluorescent dye, frequently used for cellular imaging. The functional group of FITC, isothiocyanate group, is reactive towards amine group which makes it possible for conjugation. To graft the surface of Fe_3O_4nanoparticles with required amine group, 1.25 ml of concentrated NH_4OH was added to the cross linked Fe_3O_4 nanoparticles solution and the mixture was left for continuous sonication overnight. To label dextran coated Fe_3O_4 with FITC, 1 ml of 0.01 M FITC (10 μmol) in phosphate buffer saline (PBS) at pH 7.4 was added to 1 ml of amino functionalized cross linked Fe_3O_4. The mixture was allowed to stand for 1 hour at room temperature and excess FITC was removed by dialysis.

3.3: Cell culture protocol

All the in-vitro cell studies done in this research were conducted on human pancreatic cancer cells, Mia PaCa 2.The cell culture experiments were carried out inside a cell culture hood.

MIA PaCa-2 human pancreatic cancer cells were cultured on poly L-lysine-coated petri dishes in Cell Growth Medium (CGM) made of Dulbecco's modified essential medium (DMEM)

containing 10% fetal bovine serum (FBS) and 1% Penicillin-Streptomycin. To continue the cell line, the confluent plate is split and cells are re-cultured on a new plate as described below. Cell culture plate which was stored in the incubator was taken out and growth media was carefully aspirated. The cells were washed twice with 10 ml of sterile 1X phosphate buffered saline (PBS) at pH 7.4 followed by exposure to 0.25% trypsin in PBS for 3-4 minutes inside the incubator which detaches the cells from the surface of the plate. CGM was then added to terminate the trypsin activity. The resulting cell suspension was centrifuged for 4 minutes at 1,500 rpm (300g), and the pellet re-suspended in 6 ml of cell growth medium. Then 1 ml of this suspension was added to a new culture plate containing 9 ml of fresh CGM. To keep the cells healthy splitting was done twice a week.

3.4: Structural characterization methods

In order to confirm that the synthesized samples have the required properties for intended applications we have utilized different characterization techniques as described in the rest of the chapter. X-ray diffraction is mainly and commonly used to identify the crystal structure of the material, to estimate the crystalline size and to identify the crystalline impurities in the sample whereas transmission electron microscopy is a great tool to investigate the morphology and determine the particle size distribution accurately. Colloidal parameters such as hydrodynamic size and zeta potential are determined using dynamic light scattering.

3.4.1: X-ray diffraction (XRD)

X-rays are electromagnetic radiation with the wavelength of 0.01 to 10 nm corresponding to energies in the range of 100 eV to 100 keV. X-rays with short wavelengths that are comparable to the size of atoms can be used to probe the arrangement of atoms and molecules inside the crystalline materials. Generally, Cu and Mo targets are used in diffractometers which

produce x- rays of wavelength 1.54 Å and 0.8 Å respectively. When x-rays interact with atoms of the materials, waves diffracted from different layers of atoms interfere with one other to produce sharp maxima in the intensity (constructive interference) if atoms are arranged periodically (Figure 3.2).The basic principle of XRD is described by Bragg's Law,

$$2d_{(hkl)} \sin\theta = n\lambda \tag{3.1}$$

where, $d_{(hkl)}$ is the spacing between the atomic planes with the Miller indices hkl, θ is the angle between the incident rays and the atomic planes, n is any positive integer and λ is the wavelength of the incident rays.

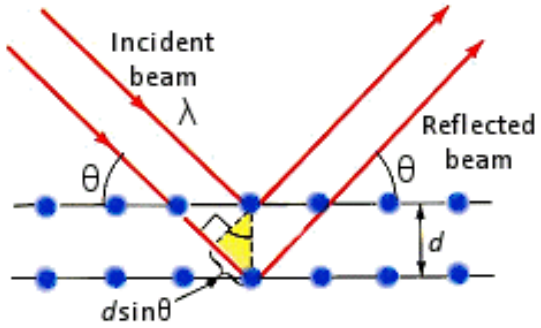

Figure 3.2: The diffraction of x-rays from atomic planes

A typical powder x-ray diffractometer consists of an x-ray source, a sample stage, a detector. The x-ray is focused on the sample at an angle θ, while the detector opposite the source reads the intensity of the x-ray it receives at 2θ away from the source path (Figure 3.3). The incident angle is increased over time always keeping the detector angle 2θ above the source path. For our XRD measurements nanoparticle powder samples, we used a Rigaku MiniFlex 600 X-ray diffractometer with a θ-2θ scanning mode operating at a voltage of 40 kV and current of 150 mA. The average crystalline size of the particles, d_{avg}, can be estimated by the Debye-Scherrer equation,

$$d_{avg} = \frac{k\lambda}{\beta_{FWHM} \cos\theta} \tag{3.2}$$

where, λ is the x-ray wavelength, k is the shape factor which is roughly equal to 0.94 for spherical particles, β_{FWHM} is the full width at half mamixa measured in radians and θ is the diffraction angle.

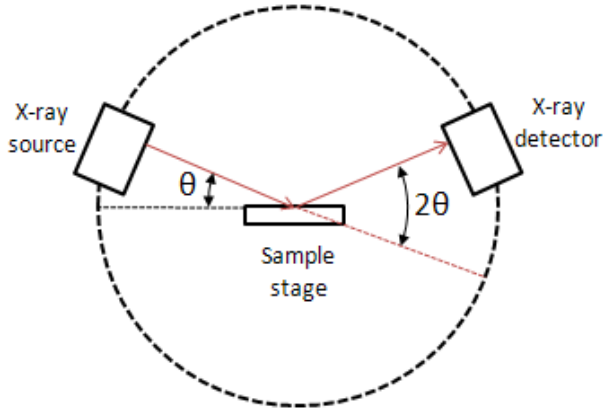

Figure 3.3: The powder x-ray diffractometer geometry

3.4.2: Transmission electron microcopy (TEM)

TEM is a powerful imaging tool used in medical, biological, and materials research. The basic principle of operation is similar to that of optical microscope, the difference being that TEM uses electrons instead of light. The wavelength of the electrons is much smaller (in the order of 10 to 100 pm) than the wavelength of light hence its resolution is many orders of magnitudes higher than an optical microscope which allow us to "see" the particles sized in nano range. The electrons that are emitted from an electron gun at the top of the microscope travel through the vacuum in the column of the microscope. This traveling electron beam is focused into very thin beams by means of electromagnetic lenses and the concentrated beam is then incident on the thin sample specimen of interest. These electrons are absorbed, scattered and transmitted through the sample. Transmitted electrons strike the fluorescent or photographic

screen at the bottom of the microscope generating a shadow image of the specimen which is visualized by means of a sophisticated camera. These images contain useful information about the morphology and crystal structure of the sample. A JEOL 2010 FasTEM transmission electron microscope operated at 200 kV was used to obtain the TEM images of our nanoparticles. The sample preparation for TEM was done by mounting one or two drops of diluted solution of nanoparticles dispersed in ethanol on a carbon coated copper grid followed by drying.

3.4.3: Dynamic light scattering (DLS)

Dynamic light scattering and photon correlation spectroscopy are widely used to determine the hydrodynamic size and size distribution of colloidal particles. When a monochromatic beam of light, such as laser, passes through a solution, time dependent fluctuations in the intensity of scattered light occur due to the Brownian motion of the particles in the solution. An autocorrelation analysis of these intensity fluctuations provides an estimation of the diffusion coefficient (*D*) which relates to the hydrodynamic size or diameter, d_H, The autocorrelation function is given by a single exponential function, where A is the baseline at infinite decay and β is the amplitude at zero decay.

$$C(\tau) = A + \beta exp(-2\tau\Gamma) \quad \textbf{(3.3)}$$

The above equation can be used to determine Γ which relates to the diffusion constant *D* through $D = \Gamma/q^2$ where q is the scattering wave vector, a quantity that is related to the scattering angle, wave length of the laser and the refractive index of the solution. The hrdrodynamic size or diameter, d_H , can be then estimated using Stokes-Einstein relation (Eq 3.4),

$$D = \frac{k_B T}{6\pi\eta d_H} \quad \textbf{(3.4)}$$

η, k_B,T being the viscosity of the medium, boltzman constant and absolute temperature respectively.

Both the hydrodynamic size distribution and zeta potential measurements (described in the next section) were done using a Nano ZS90 (Malvern Instruments). Ferrofluids were diluted using DI water and the pH of the dilute solution was measured using pH meter. The concentration of the nanoparticle dispersions used for these measurements was kept in the range of 50-100 μg/ml.

3.4.4: Zeta potential measurements

The particles in a colloidal suspension carry an electrical charge and the amount of charge on the particle surface is an important characteristic which determines stability of the particles in a suspension. This surface charge creates a countercharge in the surrounding solution screening the electric surface charge forming an electrical double layer. The magnitude of the net electric charge in this screening diffused layer is equal that of net surface charge, but has the opposite polarity. As a result the overall structure is electrically neutral. The charges on the particle surface are normally considered to be attached rather firmly and the outer boundary of this layer is defined as the Stern layer. The surrounding charge, by contrast, is much more loosely associated with the particle and diffuses with the charged particle. The boundary of this layer is defined as the slipping plane (Fig. 3.4). The electrostatic potential changes very quickly (and linearly) through the surface- layer whereas it changes more or less exponentially through the diffuse layer. The charge or electrostatic potential at the slipping plane is defined as the zeta potential (ξ) and is the key indicator of the stability of colloidal suspensions. It depends on the properties of the dispersive medium such as pH as well as on properties of the surface.

Electrostatic repulsion between particles depends on the value of zeta potential hence higher the absolute value of the zeta potential would lead to a more stable the system.

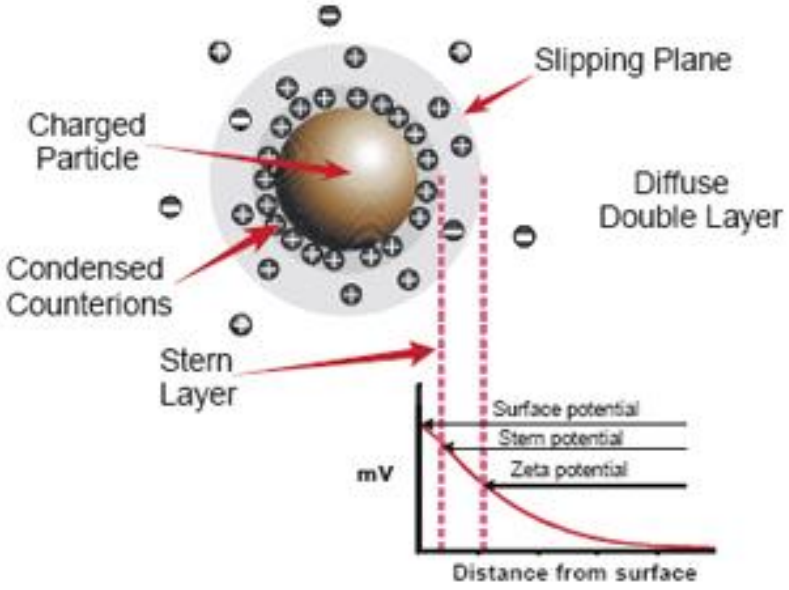

Figure 3.4: Distribution of charges around a charged particle in a colloidal suspension

3.5: Magnetic characterization

The magnetic properties (saturation magnetization, magnetic core radius, coercivity, etc.) of the synthesized powder as well as the ferrofluid samples were determined using a Quantum Design Model 6000 Physical Property Measurement System (PPMS). It can be used to take measurements in the temperature range from 1.8 to 400 K with magnetic fields up to 9 T. The PPMS consists of a cryostat unit having superconducting magnetic coil. The sensitivity of AC and DC measurements are 10^{-8} and 10^{-5} emu, respectively. Sample preparation for the measurements of powder samples was done as follows: Approximately, 20-30 mg of nanoparticles was placed in a gelatin capsule, packed with cotton to restrict the motion of the sample and mounted in a straw with proper stitching. For the ferrofuid samples, we used a sealed

liquid sample holder purchased from Quantum Design. However using this holder limits our ferrofluid measurements at 300 K.

In order to investigate the dynamic relaxation of the synthesized particles, AC magnetization measurements on the powder samples under a 10 Oe excitation were taken in the entire temperature range T = 10 K to 300 K using PPMS .The measurements were done at different frequencies ranging from 350 Hz to 2000 Hz.

3.6: Magnetic hyperthermia measurements

The schematic of experimental set up for a typical hyperthermia set up (Fig. 3.5.a) consist of a parallel LC tank circuit. The coil carrying the current provided by the amplifier essentially acts as an inductor of inductance *L*. It is connected to a capacitor of capacitance C and this arrangement generates and oscillating magnetic field of a particular frequency. The ferrofluid sample is positioned inside the coil with an insulation cover to prevent heat exchange with the surroundings (adiabatic system). For the magnetic hyperthermia measurements, we used an Ambrell Easy heat station coupled with a solenoid (Fig. 3.5.b).

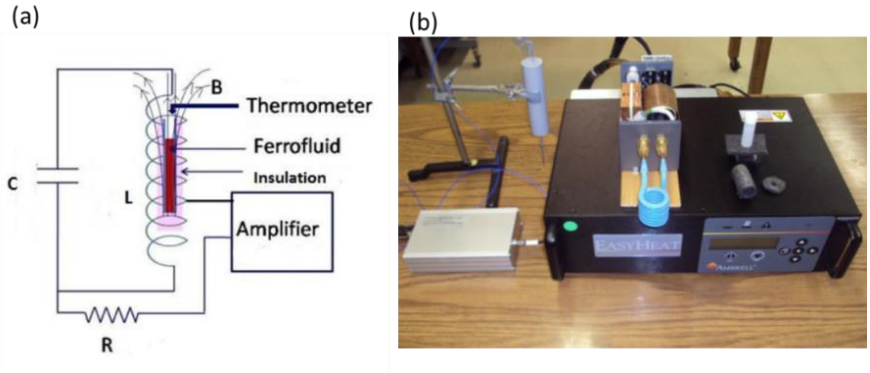

Figure 3.5: (a) The experimental set up for a typical hyperthermia set up (b) Ambrell Easy Heat System and OPTOCON fiber optic thermometer. The coil, sample holder and insulating cotton padding are shown as well.

The temperature of the sample was measured using an Optocon P/N FOTEMP1-OEM fiber optic thermometer interfaced to the computer for automatic data collection every 2 or 5 seconds. The current passing through the circuit gives estimation on the amplitude of the magnetic field while the values of *L* and *C* determine the magnitude of the frequency. The higher SAR value can be achieved by increasing the amplitude (H) and frequency (f) of the applied field. But to prevent unwarranted side effects and nerve stimulation, magnitude and frequency need to be within safety limit set to H. f=5×10 $^{-9}$ $Am^{-1}s^{-1}$. Therefore, all our measurements had been recorded under ac magnetic field amplitude of 235 Oe and at a frequency of 375 kHz which are within the required limit.

CHAPTER 4 EFFECT OF MAGNETIC DIPOLAR INTERACTIONS ON TEMPERATURE DEPENDENT MAGNETIC HYPERTHERMIA IN Fe_3O_4 FERROFLUIDS

4.1: Introduction

As described in the earlier chapters, superparamagnetic Fe_3O_4 nanoparticles have attracted a great deal of attention because of their potential applications in biomedicine and Magnetic hyperthermia (MHT) is one of the extensively studied applications. In MHT an external alternating magnetic field is applied to a tissue containing MNPs, which serve as the heat centers producing heat by relaxation losses thereby heating the tissue. As the MHT can be used for heating small regions selectively, it offers the potential for being highly selective and non-invasive technique for therapeutic treatment of cancers and as a consequence it has advantage over other treatment methods such as chemotherapy and radiation therapy.

Specific absorption rate (SAR), which measures the efficiency of heat generation, depends on magnetic properties of the particles such as saturation magnetization, magnetic anisotropy, particle size distribution, magnetic dipolar interactions, and the rheological properties of the target medium. Therefore, the applications of the Fe_3O_4 nanoparticles often require controllable synthesis methods to produce particles with desired size, shape and magnetic properties. Different synthesis methods often yield systems consisting of polydisperse ensemble of MNPs of different sizes as seen in transmission electron microscopy (TEM) images, with size distribution usually describable by a log-normal distribution function. MHT investigations are often done on colloidal suspensions of MNPs, called ferrofluids, where the nanoparticles are coated with surfactants to avoid agglomeration and minimize the effects magnetic dipolar interactions. Some ferrofluid preparations yield a mixture of isolated nanoparticles and nanocluseters [133], with varying degree of magnetic dipole-dipole interactions present in

ferrofluids. It is shown that the dipolar interactions among the MNPs affects the SAR value drastically hence that can be exploited to optimize SAR [133-136]. For a nanoparticle system consisting of polydisperse particles, a phenomenological theory was proposed to take into account the effects of magnetic dipolar interactions resulting from the magnetic moments/superspins of the superparamgnetic nanoparticles [121]. In this, so called the T^* model, dipolar interaction is taken into account by replacing the temperature, T, appearing in the argument of the Langevin function, by $T + T^*$, where T^* is a phenomenological parameter. The model was used to explain all the features of the observed M vs. H curves in granular Cu-Co alloys. Effects of dipolar interactions on SAR for a collection of monodisperse MNPs has been described Landi [120,135] by using mean-field approximation by modifying the relaxation time. As mentioned earlier, synthesis method is a key factor that determines the properties of the NPs. Over the years, many methods have been developed for synthesizing size/shape controlled, stable, biocompatible iron oxide nanoparticles as described in Chapter 3.

In this study, we have synthesized Fe_3O_4 nanoparticles using two different synthesis methods: co-precipitation (CP) and hydrothermal (HT) techniques, yielding very similar x-ray crystallite size ~ 12 nm, which were coated with dextran to obtain a well suspended, biocompatible ferrofluids. We noted that both CP and HT prepared ferrofluids show very similar saturation magnetization ~ 70 emu/g and yet exhibit very different SAR values of ~ 110 Watt/g and 40 Watt/g, respectively, at room temperature. We explain this observed reduction in SAR value by taking into account the dipolar interactions, using the phenomenological T^* model (Chapter 2.3), to fit the observed M vs. H data using Langevin function, and the temperature dependent SAR data using linear response theory. The values of the magnetic anisotropy constant, obtained as a fitting parameter in the temperature dependent SAR calculations, are in

good agreement with the values determined by frequency dependent magnetic susceptibility vs. temperature data of powder samples.

4.2: Experimental details

Preparation of the Fe_3O_4 nanoparticles by CP and HT method was done using procedure described in chapter 3. The synthesized nanoparticles were coated with dextran to obtain well suspended ferrofluid following the experimental procedure described in section 3.2.1.

The x-ray diffraction patterns of Fe_3O_4 nanoparticles (CP and HT) were measured with a Rigaku MiniFlex 600 x-ray diffractometer using CuKα radiation. Transmission electron microscopy images were obtained using a JEOL 2010 transmission electron microscope (TEM). The samples for TEM imaging were prepared by suspending the magnetic nanoparticles in water followed by sonication for several minutes and adding a drop of that solution onto a carbon-coated TEM copper grid and subsequently drying in air. The magnetic properties of ferrofluid samples were investigated by measuring *M* vs. *H* curves at 300 K using a Physical Property Measurement System (PPMS). We also measured both frequency (350 Hz to 2000 Hz) and temperature dependent (10 K to 300 K) magnetic susceptibility curves of powder samples at a field amplitude of 10 Oe to investigate their blocking behavior.

The magnetic hyperthermia measurements were carried out using an Ambrell Easy Heat system, which consists of a simple solenoid, a capacitor and a power amplifier as described in chapter 3. Small glass vials were used to hold the ferrofluid samples and the vials were padded with a cotton sleeve to minimize the heat loss to the surrounding. The magnetic hyperthermia measurements were made by applying an ac magnetic field of amplitude 240 Oe (19.1 kA/m) at 375 kHz. The temperature of the sample was monitored using an Optocon P/N FOTEMP1-OEM fiber optic thermometer, which was inserted through a small hole at the center of the top cover of

the vial to make contact with the ferrofluid. The thermometer was connected to a computer and the heating curve (temperature vs time) readings were logged at a regular interval of 2 s. To account for the heat loss to the environment the cooling curves were recorded immediately after the magnetic field was turned off, as described elsewhere (chapter 3).

4.3: Results and discussion

The XRD patterns of the as-prepared CP and HT Fe_3O_4 nanoparticles are shown in Fig.4.1.

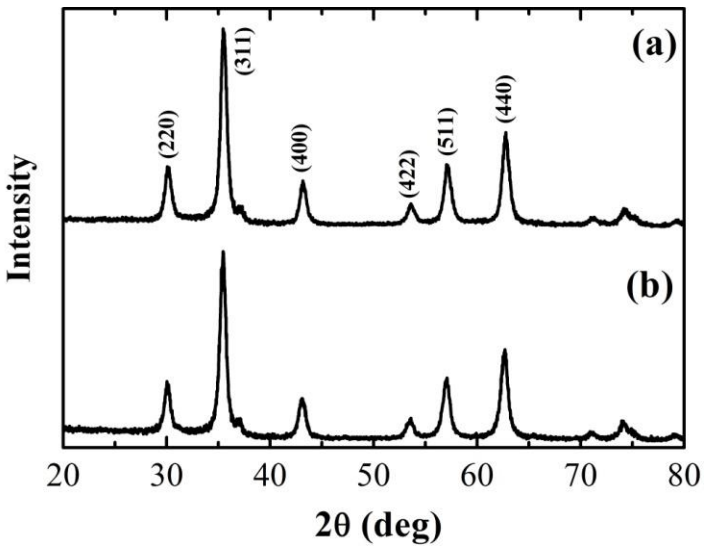

Figure 4.1: X-ray diffraction patterns of as prepared Fe_3O_4 nanoparticles (a) by hydrothermal (HT), and (b) by co-precipitation (CP) methods.

All the observed peaks in the diffraction patterns are consistent with those of standard XRD pattern of Fe_3O_4 (reference JCPDS No. 82-1533) confirming cubic crystalline structure and the absence of any impurities within the XRD detection limits. The average crystallite size of the CP and HT samples using Debye-Scherer equation was determined to be 11.7±0.6 nm and 11.8±0.5 nm. TEM images (Fig. 4.2) clearly show that the samples contain nearly spherical particles with a distributed particle sizes (polydispersed).

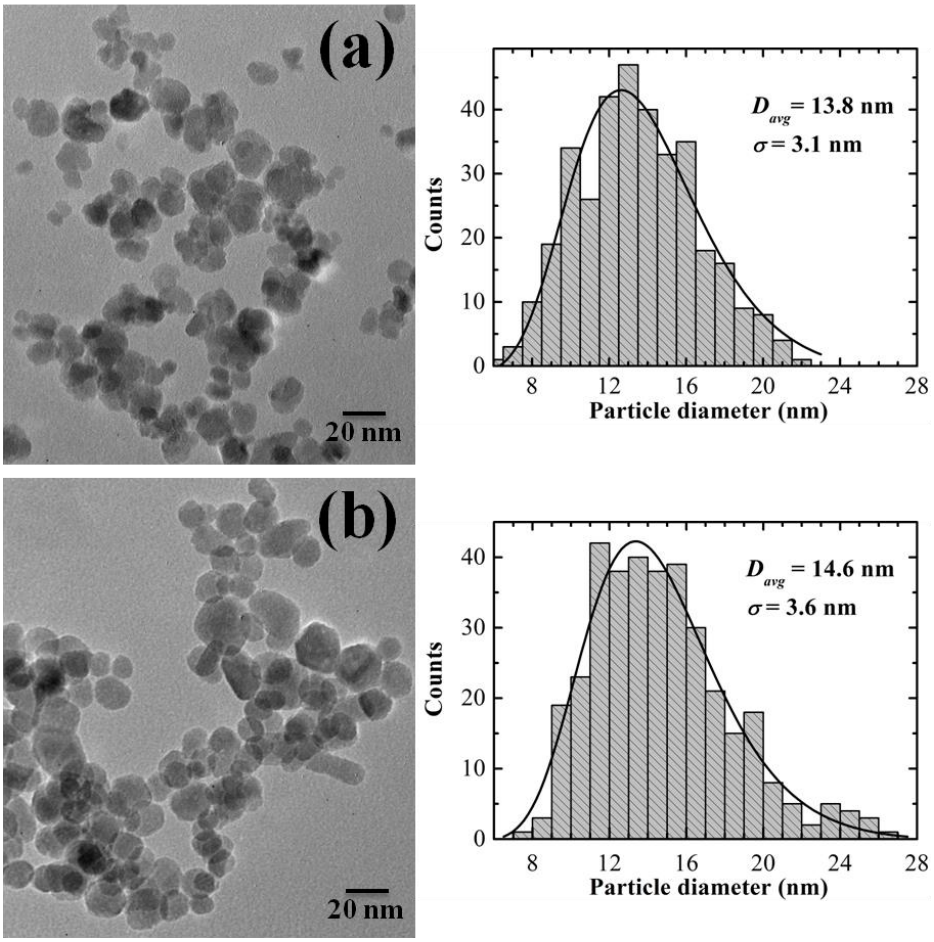

Figure 4.2: TEM images of the as prepared Fe_3O_4 nanoparticles prepared by (a) CP method, (b) HT method, and their histograms of the particle size distribution. The solid lines in the histograms represent the log-normal fits.

The particle size distributions of two samples were determined by measuring the sizes of at least 200 particles from the TEM images and fitting the histogram with a log-normal distribution function, Eq.2.4, $f(D) = \frac{1}{\sqrt{2\pi}\lambda D}\exp\left\{-\frac{\left[\ln(D/D_\circ)\right]^2}{2\lambda^2}\right\}$, where, D_o is the most probable particle diameter and λ is the width of the distribution. The histogram and the log-normal fits are shown in Fig. 4.2. Interestingly, the average particle sizes of the CP and HT nanoparticles are calculated to be 13.8±3.1 nm and 14.6±3.6 nm, which are slightly larger than their corresponding estimated XRD crystallite sizes. The previous studies done on Fe_3O_4

nanoparticles also have reported a larger TEM size than their XRD crystallite size similar to this observation [133], and the observed difference is attributed to existence of an amorphous layer of 1-2 nm thickness on the surface of the nanoparticles [137].

Figure 4.3 shows the field dependent DC magnetization, $M(H)$, curves of CP and HT prepared Fe_3O_4 nanoparticle ferrofluids at room temperature.

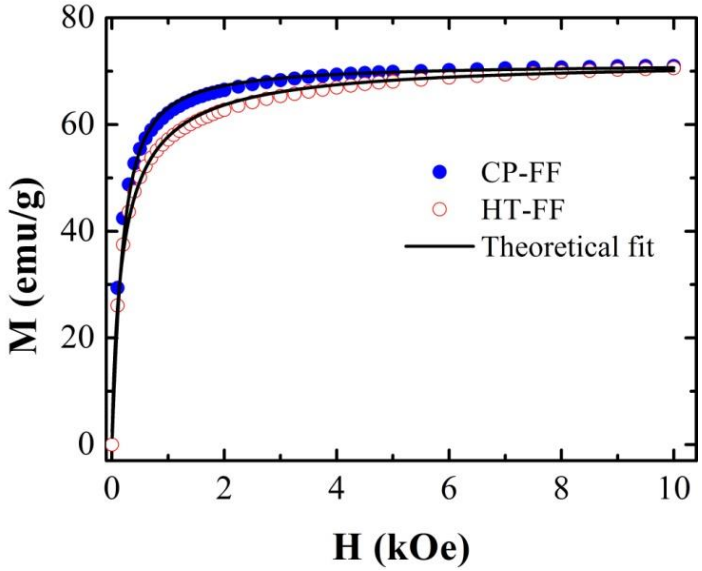

Figure 4.3: Room temperature M vs. H curves of the ferrofluid samples of Fe_3O_4 nanoparticles prepared by CP and HT methods. The solid lines are the theoretical fits.

Both the systems show superparamagnetic behavior with zero coercivity and a very similar saturation magnetization of ~ 70 ± 2 emu/g. This value is lower than the value reported for bulk Fe_3O_4 ~ 92 emu/g, which is attributed to the surface disorder such as the existence of magnetic dead layer, spin canting at the particle surface or the spin-glass like behavior of the surface spins modifying the anisotropy and the magnetic moments of the surface atoms [138,139]. It has also been shown in the literature that the saturation magnetization of the particles, in general, increases with the crystallite size [140]. The observation of similar value of saturation magnetization in our CP and HT samples is consistent with our XRD/TEM results showing similar crystallite/physical size.

However, the *M* (*H*) curves differ at lower fields (see Fig. 4.3), perhaps indicative of a difference in magnetic core size distribution. Assuming the superparamagnetic particles are non-interacting, M-vs-H data can be fitted using Eq. 2.3,

$$M(H) = M_s \frac{\int_0^\infty f(D)VL(x)dD}{\int_0^\infty f(D)VdD}$$

Using the particle size (D_o) and the width of the distribution (λ) as fitting parameters, we found the best fitting yielded the average particle diameters to be 10.8±2.0 nm and 7.6±3.2 nm for CP sample and HT samples. However, these parameters are not consistent with the measured values from XRD analysis and in particularly, the deviation is significant for the HT sample. We attribute this discrepancy due to the presence of magnetic dipolar interactions among nanoparticles in the ferrofluid samples. We have accounted for the dipolar interactions by introduced a phenomenological temperature, T^*, in the modified the Langevin function, $L(x) = \coth x - \frac{1}{x}$, with $x = \frac{M_s VH}{k_B(T + T^*)}$ as described in section 2.3. The solid lines in Fig. 3 show the best fits for CP and HT ferrofluids using the modified Langevin function in Eq. (2), and using T* as an additional fitting parameter while constraining the average particle diameter close to their XRD crystallite size. Table 4.1 gives a summary of the fitting parameters.

Table 4.1: Fitting parameters obtained from the Langevin fitting for CP and HT ferrofluid samples

Sample	**D_0 (nm)**	**λ**	**T^* (K)**	**D_{avg} (nm)**
CP-Ferrofluid	10.6 11.6	0.19 0.19	0 70	10.8 ± 2.1 11.8 ± 2.3
HT-Ferrofluid	7.0 10.9	0.40 0.35	0 550	7.6 ± 3.2 11.6 ± 4.2

Clearly, the M (H) fitting shows the presence of dipolar interaction in both samples with interaction being much stronger in HT sample compared to the CP sample. Nanoparticles in CP ferrofluid exhibit nearly non-interacting superparamgnetic behavior with a smaller T* ~ 75 K, corresponding to an interaction energy of ~ 6 meV. One would expect this as the nanoparticles are small and are coated with polymer surfactants which form a thick layer on the particles increasing the interparticle distance (hydrodynamic size ~ 100 nm) in ferrofluid, resulting in decreased dipolar interactions. On the other hand, HT sample shows an order magnitude higher T* value compared to the CP sample indicating the presence of strong dipolar interactions among nanoparticles in HT ferrofluid. We also notice that the polydispersity in the particle size is much broader in HT prepared samples. We believe that the HT method of synthesis which involves heating at 140 ^{o}C leads to particle agglomeration and an increased fraction of clustered nanoparticles in the surfactant coated ferrofluid particles.

The results of magnetic hyperthermia measurements of CP and HT ferrofluid samples are shown in Fig. 4.4 with the inset showing the heating curves. Specific absorption rate, (SAR), of the ferrofluid samples were determined according to, [122]

$$SAR(T) = \frac{M_{sample}}{m_{Fe_3O_4}} C \left(\frac{\Delta T}{\Delta t} \right)_T \qquad (3)$$

where, M_{sample} is the mass of the sample, $m_{Fe_3O_4}$ is the mass of Fe_3O_4 nanoparticles in the sample, C is the specific heat capacity of the sample, and $\left(\frac{dT}{dt} \right)_T$ is the time rate of change of temperature at T. The details of the measurements of heating and cooling curves, and the analyses of data to extract the temperature dependant SAR by fitting the heating and cooling curves to obtain $\left(\frac{dT}{dt} \right)$ as a function of temperature is reported in Nemala et al [137]. The heat

capacity of the sample was assumed to be close to that of the carrier liquid (water) due to low concentration of nanoparticles in the samples. Clearly, the SAR data of the two samples are strikingly different although they both have similar average particle size. As discussed below, we have used the linear response theory to fit the entire temperature dependent SAR using the *T** model to take the dipolar interactions into account and investigate the effect of magnetic anisotropy as described below.

For an ensemble of polydisperse particles, the temperature dependent average power dissipation in the sample isgiven by the Eq.4.3,

$$\overline{P}(T) = \int_0^\infty \frac{\mu_0 \chi_0 H_0^2 \omega}{2} \frac{\omega \tau_{eff}}{1 + (\omega \tau_{eff})^2} f(D) d(D) \qquad \textbf{(4.3)}$$

Here, H_o and $\omega$are the amplitude and angular frequencyof the applied ac magnetic field, μ_o is the vacuum permeability. τ_{eff} is effective relaxation time involving Néel relaxation, Brownian relaxation times and χ_o is equilibrium susceptibility and defined as $\frac{1}{\tau_{eff}} = \frac{1}{\tau_N} + \frac{1}{\tau_B}$. When dipolar interactions are taken into account using *T** model, the Néel and Brownian relaxation times can be modified as $\tau_B = \frac{4\pi\eta R_H^3}{k_B(T+T^*)}$ and $\tau_N = \frac{\sqrt{\pi}}{2}\tau_0 \exp\left(\frac{KV}{k_B(T+T^*)}\right)\sqrt{\frac{KV}{k_B(T+T^*)}}$. In these expressions, $\eta$is the viscosity of the suspension and R_H is thehydrodynamic radius of the coated nanoparticle, K is the anisotropy constant, V_m is the magnetic volume of the nanoparticles, τ_o ~ 10^{-9}s and T is the sample temperature. χ_o is given by $\chi_o = \chi_i\left(\coth\xi - \frac{1}{\xi}\right)$, where, $\chi_i = \frac{\mu_\circ \phi M_d^2 H_\circ V_m}{3k_b(T+T^\circ)}$, is the initial susceptibility, $\xi = \frac{\mu_\circ M_d H_\circ V_m}{k_b(T+T^\circ)}$where M_d, the domain magnetization of the nanoparticle, and ϕ is the volume fraction of the magnetic nanoparticles in

the ferrofluid. SAR in units of W/g is obtained using Eq. (4) as $\bar{P}(T)/m_{Fe_3O_4}$, where, $m_{Fe_3O_4}$ is the mass of Fe_3O_4nanoparticles in ferrofluids. The results of magnetic hyperthermia measurements of CP and HT ferrofluid samples are shown in Fig. 4.4 with the inset showing the heating curves.

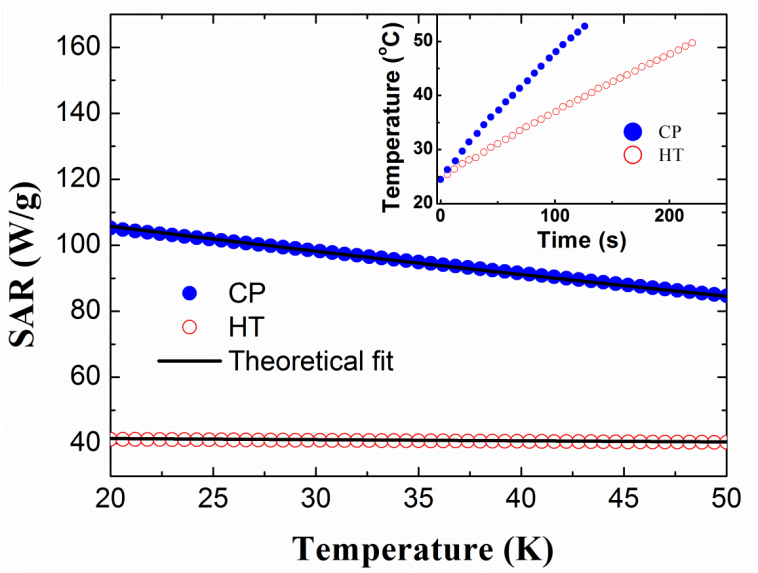

Figure 4.4: Temperature dependent specific absorption rates (SAR) estimated for CP and HT ferrofluid samples of 12mg/ml concentration at 375 kHz ac field of amplitude 235 Oe). The fitted data are represented by the black line. Inset shows the obtained heating curves for two samples.

Clearly, the SAR data of the two samples are strikingly different although they both have similar average particle size. The solid lines in Fig. 4 are the best fits to the experimental SAR data using Eq. (4), the particle size distribution parameters and T^* values given in Table 4.1, and treating the anisotropy constant, *K*, as a fitting parameter. The SAR fitting yields similar anisotropy constants for HT (~ 26 kJ/m^3) and CP (~ 22 kJ/m^3) ferrofluid samples. Clearly, the dipolar interactions play an important role in magnetic hyperthermia and reduce the value of SAR.

We have generated SAR (room temperature) curves with and without the dipolar interactions. Figures 4.5 and 4.6 show the simulated SAR as a function of particle size (D_o) using

Eq. (4.3), and λ obtained from the M (H) fitting (Table 4.1), and the K obtained from the fitting the experimental SAR data (Fig. 4.4).

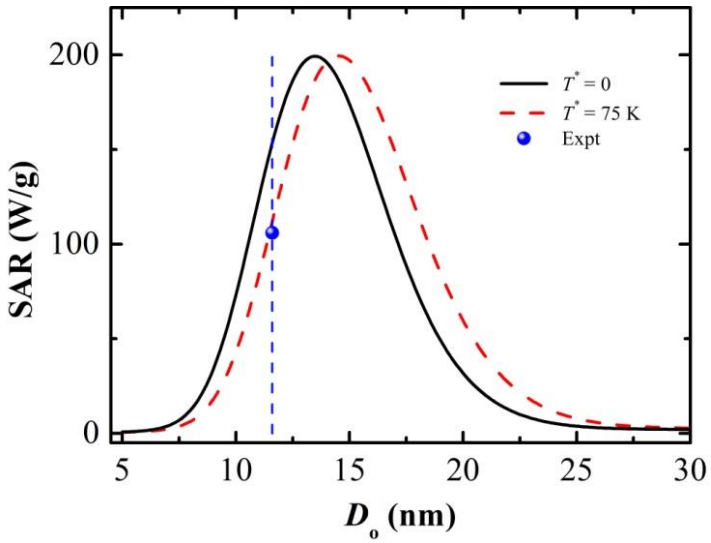

Figure 4.5: Theoretically generated SAR as function of particle size (K_{eff} = 22 kJ/m^3 and λ = 0.19) using Eq. (4) for the CP ferrofluid with and without the dipolar interaction. The symbol represents the experimental value for the CP ferrofluid, showing SAR would be higher in the absence of dipolar interactions for the same particle size distribution.

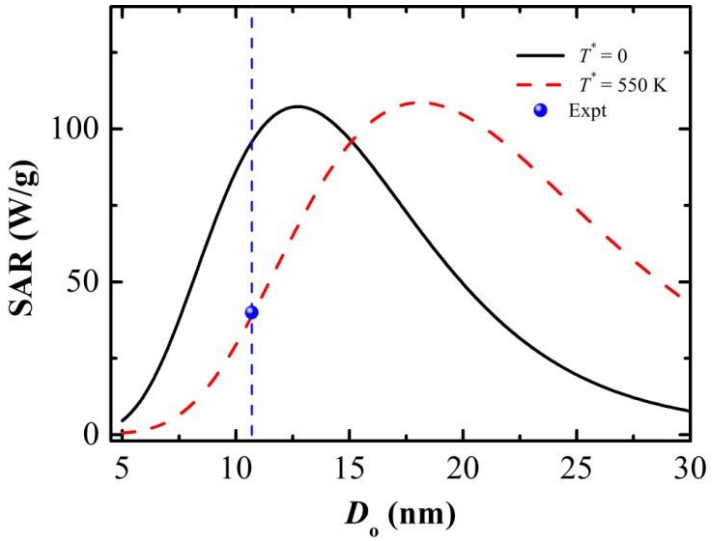

Figure 4.6: Theoretically generated SAR as function of particle size (K_{eff} = 26 kJ/m^3 and λ = 0.35) using Eq. (4) for the HT ferrofluid with and without the dipolar interaction. The symbol represents the experimental value for the HT ferrofluid, showing SAR would be much higher in the absence of dipolar interactions for the same particle size distribution.

The calculations show that SAR increases with increasing particle size showing a peak at a critical size, beyond which SAR decreases with increasing particle size. Further, the peak in SAR shifts to higher particle size when the dipolar interactions are included in the simulation, and the curve becomes positively skewed as the value of λ increases (Fig. 4.6). For our CP sample, the particle size is below the critical size and the dipolar interactions reduce SAR value by a small amount (Fig. 4.5).

On the other hand, although the HT sample has a somewhat larger value of *K*, the peak SAR value is smaller (Fig. 4.6) than that of the CP sample (Fig. 4.5). This is attributed to much larger size distribution (λ) of MNPs in HT sample. When the dipolar interactions are introduced for this sample, the SAR value decreases further making it even smaller compared to that of the CP sample. We also note that the HT prepared particles have their size very close to the critical size needed to produce the maximum SAR, but the dipolar interactions reduce their magneto-thermal heating efficiency.

To understand the dynamic relaxation of the CP and HT prepared nanoparticles and to independently determine their effective magnetocrystalline anisotropy, we have measured the ac susceptibility of the powder samples as a function of temperature at different frequencies ranging from 350 Hz to 2 kHz. Figure 4.7 shows the imaginary part, χ'', of the ac susceptibility vs. temperature data for the samples. The ac magnetization curves of HT sample are broader compared to those of the CP samples, indicating a wider size distribution in the former sample. This is also in agreement with the magnetization data as discussed earlier. Further, the data clearly shows that the blocking temperature, T_B, is frequency dependent and shifts towards higher temperatures with increase in frequency in both CP and HT samples implying thermally activated blocking process. The frequency dependence of T_B for a collection of non-interacting

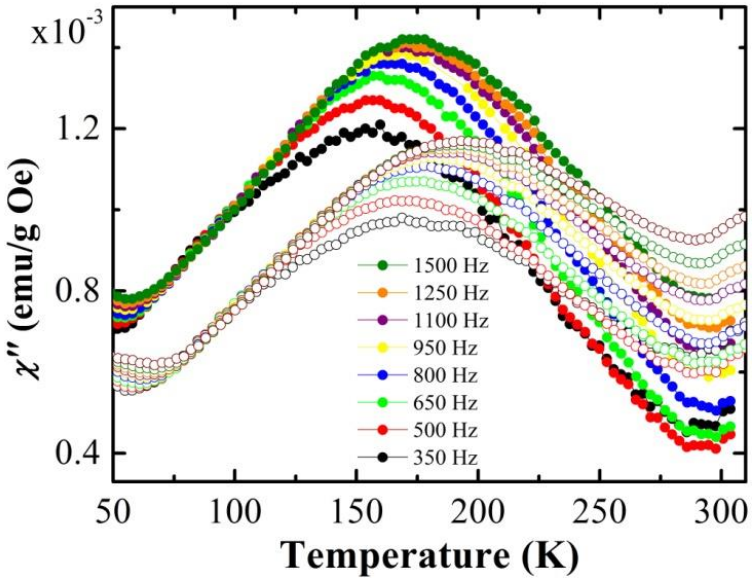

Figure 4.7: Temperature dependent out-of-phase susceptibility of powder samples at different frequencies (closed circles represent the data for CP sample and the open circles represent HT sample data). HT data has also been measured at 2 kHz in addition to the frequencies mentioned and the data is shown.

particles is given by the Néel-Brown model given by equation 2.7, $\tau = \tau_0 \exp\left(\frac{KV_m}{k_B T_B}\right)$ described in Section 2.2.1. In the absence of an external field, KV_m is the energy barrier for the reversal of the magnetic moment. For a system of particles with dipolar interactions the energy barrier can be replaced by an effective anisotropy energy barrier, $E_{eff} = K_{eff} \langle V_m \rangle$. Figure 4.8 shows the plots of ln (τ) versus $1/T_B$ for the two samples exhibiting the linear behavior. The results of the analyses are given in Table 4.2. The observed linear relationship with $\tau_o \sim 10^{-9}$ s imply that Néel model correctly describes the superparamagnetic behavior of these MNPs. We note that the anisotropy energy barrier is somewhat larger in HT prepared sample compared to that of the CP sample due to the presence of strong dipolar interactions. It is gratifying to note that the anisotropy constant determined from the ac susceptibility measurements are in close agreement with those determined from the hyperthermia measurements.

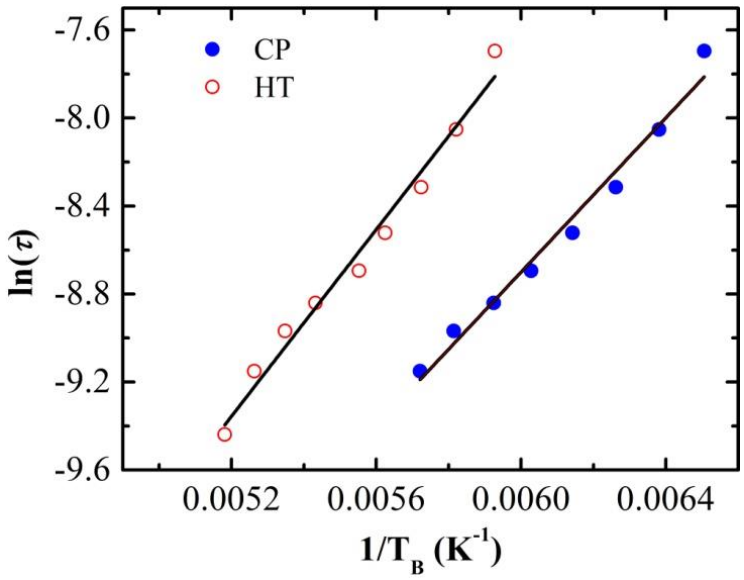

Figure 4.5: The plot of ln (τ) vs. $1/T_B$ for the CP and HT Fe_3O_4 powder samples.

Table 4.2: Estimated values of magnetic anisotropy constant from the plot of ln (τ) versus $1/T_B$

Sample	τ_o (s)	$K_{eff} <V_m>$ (J)	K_{eff} (kJ/m^3)
CP-Powder	4.5×10^{-9}	2.4×10^{-20}	25.2± 4.3
HT-Powder	1.4×10^{-9}	2.9×10^{-20}	24.9± 4.2

4.4: Conclusions

In summary, we have prepared Fe_3O_4 nanoparticles by two different methods, co-precipitation (CP) and the hydrothermal (HT) synthesis and measured their magnetic and magnetothermal properties. Although both the samples have similar particle size (~ 12 nm) and saturation magnetization (~ 70 emu/g), yet they show drastically different heating rates (SAR) at room temperature ~ 110 W/g (CP sample) and ~ 40 W/g (HT sample). We have explained this observed reduction in SAR by taking into account the dipolar interactions and the distribution of magnetic core size of MNPs in ferrofluids. The HT ferrofluid shows nearly an order of

magnitude higher effective dipolar interaction and a wider distribution of magnetic core size of MNPs compared to that of CP ferrofluid. We have fitted the temperature dependent SAR data using linear response theory, incorporating an effective dipolar interaction, to determine the magnetic anisotropy constant of the magnetic nanoparticles prepared by CP (22 ± 2 kJ/m^3) and HT (26 ± 2 kJ/m^3) synthesis methods. These values are in good agreement with the magnetic anisotropy constant determined using frequency and temperature dependent ac magnetic susceptibility data obtained on the powder samples. Based on the analyses of the experimental data, we conclude that the HT method of synthesis leads to clustering of nanoparticles with strong dipolar interaction. The observed decrease in SAR of the HT sample, despite its somewhat larger anisotropy constant, is explained by taking into account the effects of magnetic dipolar interactions using the so called T^* model.

CHAPTER 5 GADOLINIUM DOPED Fe_3O_4 NANOPARTICLES FOR MAGNETIC HYPERTHERMIA

5.1: Introduction

Integration of diagnostic imaging and therapeutic function into a single platform, so-called "Theranostics", is of great research interest as a new direction in nanomedicine research [1]. Theranostics refer to agents that allow the combined diagnosis, treatment and follow up of a disease, and are expected to contribute to personalized medicine. Superparamagnetic Fe_3O_4 is considered as an ideal vehicle in the development of theranostic nanomedicines as they can be multi-purposely used for magnetic resonance imaging (MRI) and targeted delivery of therapeutic agents such as anticancer drugs, siRNA and magnetic hyperthermia (MHT). Several different approaches of developing Fe_3O_4-based theranostic agent for multimodal and multifunctional applications are shown in the figure 5.1.

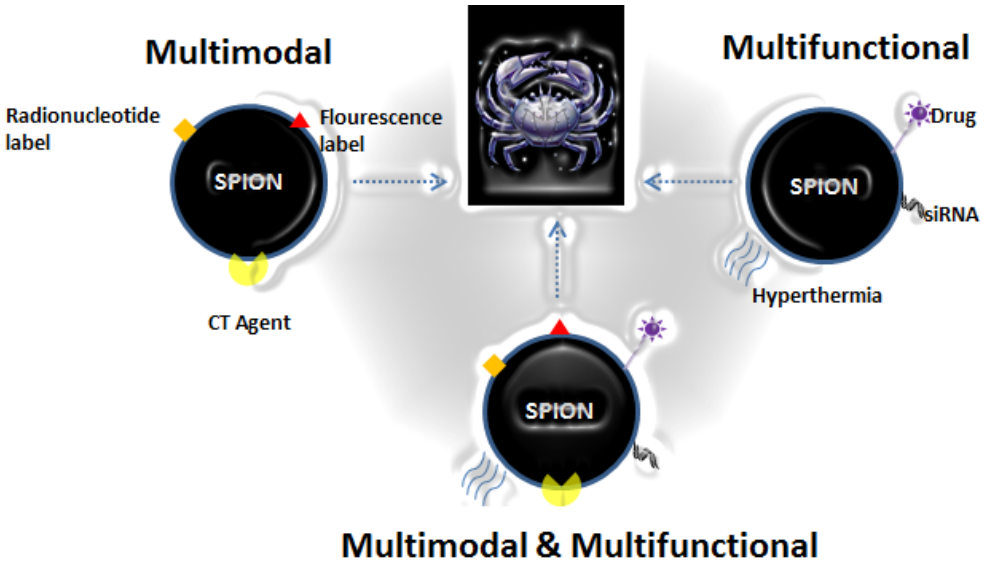

Figure 5.1: Different approaches adopted in developing a SPION-based theranostic agent [141].

The application of superparamagnetic Fe_3O_4 in magnetic hyperthermia is well described in the earlier chapters. Another attractive application of superparamagnetic nanoparticles is to be

used as next generation of imaging probes in Magnetic resonance imaging (MRI). MRI is one of the most powerful and noninvasive medical diagnostic tools by monitoring the change in magnetization of hydrogen-protons in water molecules contained in a tissue, when placed in a magnetic field and exposed to a pulse of radio frequencies. This mapping provides a picture of anatomical structure due to the fact that protons in different tissues with varying water concentration and magnetic resonance properties react differently.

Contrast agents are used to enhance the images as they affect the behavior of the protons in their vicinity sharpening the contrast. Contrast agents used in MRI are divided into two categories; T_1 and T_2 contrast agents based on their effect on the magnetic relaxation processes of the protons [142]. The reduction in the T_1relaxation time (higher rate $1/T_1$), enhances the signal resulting a brighter image whereas the reduction in T_2 relaxation time (higher relaxation rate, $1/T_2$) decreases the signal, darkening the image. Most commonly used T_1 contrast agents are paramagnetic compounds that are composed of metal ion with permanent magnetic moment due to unpaired electrons [gadolinium (Gd^{3+}) or manganese (Mn^{2+})] and a chelating ligand, such as diethylene triamine pentaacetic acid, DTPA [142,143]. The chelate prevents the lanthanide from binding to chelates in the body making the paramagnetic lanthanide ion less toxic. T_1 contrast agents mainly reduce the longitudinal (T1) relaxation which is due to energy exchange between the spins and surrounding lattice (spin-lattice relaxation) and result in a brighter signal. The second class, T_2contract agents, consists of superparamagnetic nanoparticles, such as Fe_3O_4, have a strong effect on the transversal (T_2) relaxation properties. In an external magnetic field, nanoparticles are magnetized and generate induced magnetic fields locally. These induced fields perturb the magnetic relaxation processes of the protons in the water molecules, especially the spin-spin relaxation (transverse relaxation). The transversal (T_2) relaxation time decreases which

results in darkening of MR images. The role of superparamagnetic nanoparticles as T_2 contrast agent explained above is depicted in figure 5.2.

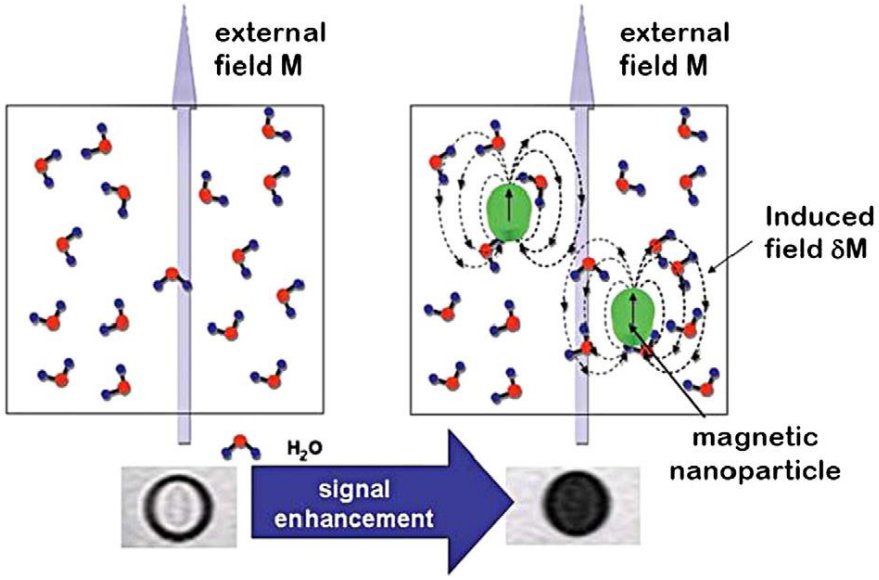

Figure 5.2: Magnetic nanoparticles as T_2contrast agent for MRI. [144]

When using nanoparticles as contrast agents for MRI, it is crucial that they are captured into the cells efficiently upon the exposure. There are various research studies done on enhancing the MRI signal for cancer detection using superparamagnetic Fe_3O_4nanoparticles as T_2 contrast agents [145-147]. For example, Jun et al. [148] have successfully synthesized superparamagnetic iron oxide nanoparticles of 9 nm size as magnetic probes for the in-vivo detection of cancer cells implanted in a mouse. In their research work, 2, 3-dimercaptosuccinic acid (DMSA) ligand is attached to the nanoparticles surface to obtain hydrophilic nanoparticles and the nanoparticles are further conjugated with the cancer-targeting antibody, Herceptin. The specific binding properties of Herceptin against a HER2/neu receptor over-expressed from breast cancer cells lead to the successfully detection of breast cancer cells (SK-BR-3) hence gives a dark MR image.

Even though both T_1 and T_2 mapping are powerful techniques, single mode contrast agents are not always sufficient in modern diagnosis as they have certain drawbacks and limitations [149]. For example, the dark contrast produced by T_2 agents can also be generated from adjacent bones or vasculatures or there can be susceptibility artifacts due to the sharp change in magnetic field surrounding the contrast agent. Also, Gd-chelates (T_1 agent) have high mobility which shorten their presence in the vascular system and raise possible toxicity issues. Thus, there is a growing interest in developing complementary T_1–T_2 dual-modal contrast agents, combining the advantages of positive and negative contrasts to obtain high sensitivity and biocompatibility for improved diagnosis [150]. Two different approaches of integrating T_1 and T_2species have been reported recently [149]. One is constructed by labeling T_1 signaling elements (Gd species) on magnetic nanoparticles. In the study done by Bae et al [151],Gd-DTPA,a representative Gd chelate-based T_1 MRI contrast agent, is covalently attached to dopamine-coated iron oxide nanoparticles. Their results demonstrated that the composite not only had the ability to improve surrounding water proton signals on the T_1-weighted image, but also could induce significant signal reduction on the T_2-weighted image. In another study reported by Santra et al. [152], Gd-DTPA is encapsulated within the poly (acrylic acid) (PAA) polymer coated superparamagnetic iron oxide nanoparticle (IO-PAA) conjugated to folic acid which act as the targeting ligand for breast cancer cells (HeLa cells). When nanoparobes internalized within the cells, which is acidic, composite magnetic nanoprobe degraded resulting in an intracellular release of Gd-DTPA complex with subsequent T_1 activation which can be seen by MRI. Authors claim that thisT_1 nano-agent could be used for the detection of acidic tumors. The other type of conjugated system consists of T_1 paramagnetic elements embedded into T_2 magnetic nanoparticles. For example, Zhou et al [153] have synthesized Gd_2O_3-embedded iron

oxide nanoparticles with an overall size of 14 nm which can act as a T_1 –T_2 mutually enhanced dual-modal contrast agent for MR imaging of liver and hepatic tumor detection with great accuracy in mice. Xiao et al [154], have prepared PEGylated, Gd-doped iron oxide nanoparticles which is applicable as a T_1–T_2 dual-modal MRI contrast agent. Their in-vivo MRI results demonstrated the simultaneous contrast enhancements in T_1- and T_2-weighted MR images towards the glioma bearing mice.

Even though the multi-functionality of superparamagnetic Fe_3O_4 nanoparticles based nano systems for drug delivery and imaging modalities [141] has been investigated widely, the possibility of incorporating magnetic hyperthermia and MRI is not explored much. In addition to be used as a T_1 –T_2 dual-modal contrast agent for MR imaging, Gd doped Fe_3O_4nanoparticles has the potential to act as an effective MHT agent [155]. Gd (III) is known to oppose net magnetic moment of Fe (III)/Fe (II) in oxides, reducing magnetizations [156-158]. Therefore Gd doping may reduce the hyperthermia efficiency but by using the correct amount of doping we can always explore the possibility of using them as both MRI contrast agents and hyperthermia mediators. To the best of our knowledge, there are very few studies done on the magnetic hyperthermia efficiency of Gd doped Fe_3O_4nanoparticles [159,160]. Both the studies report higher SAR values for Gd doped (< 1%) Fe_3O_4nanoparticles compared to the reported values for undoped samples.

In this study, we synthesized Gd–Fe_3O_4 (2.5 at %) using co-precipitation technique, followed by the structural and magnetic characterizations. We found that the doping of Gd^{3+} ions into Fe_3O_4 spinel has significantly influenced the average crystallite size and the saturation magnetization. We conducted the magnetic hyperthermia experiments on the Gd doped $Fe_3O_4$and our detailed analysis demonstrate that the SAR value of the doped samples is similar to the

undoped Fe_3O_4despite the reduction of the magnetization upon doping. This study raises the possibility of using Gd–Fe_3O_4nanoparticles for multimodal contrast imaging and cancer treatment by hyperthermia.

5.2: Synthesis and Structural Characterization

Gd doped Fe_3O_4 nanoparticles were synthesized by a co-precipitation method, and coated with dextran according to the details explained in chapter 3. For a typical synthesis of 2.5 at% Gd–Fe_3O_4, aqueous solution of $FeCl_2.4H_2O$, $FeCl_3.6H_2O$ and $Gd(NO_3)_3$were prepared in a molar ratio of 1.00 : 1.925 : 0.075 in 25 ml volume followed by the addition of 250 ml of 1M NH_4OH. The concentration of the produced ferrofluid was adjusted to 12 mg/ml for further measurements. Figure 5.3 shows the XRD pattern of both the Gd doped and undoped Fe_3O_4 nanoparticles.

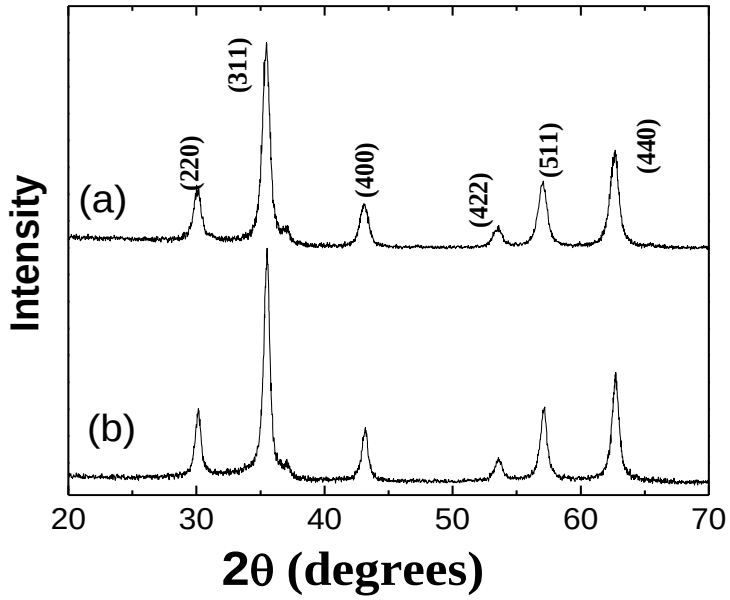

Figure 5.3: XRD spectra for (a) Fe_3O_4 nanoparticles (b) Gd-doped Fe_3O_4 nanoparticles

All the observed peaks in the XRD patterns can be indexed to the Fe_3O_4 crystal structure with no evidences for the presence of other crystalline impurity phases in significant amounts. According to the earlier studies Gd^{3+} ions tends to replace the Fe^{3+} ions of the octahedral sites in inverse spinel crystal structure [161]. From the XRD spectra, it is observed that Gd doping does

not disturb the Fe_3O_4crystal structure significantly. Using several intense XRD peak and the Debye-Scherer equation the crystallite sizes of the $Fe_3O_4$and Gd doped Fe_3O_4nanoparticles samples were determined to be 11.7±0.6 nm and 14.9±0.5 nm respectively. This increase in the crystalline size is consistent with the previous studies done on Gd doping on spinel structures [162]. TEM images of the two samples are shown in the Fig. 5.4. The undoped sample consists of roughly spherical nanoparticles with smaller polydispersitywhereas the Gd doped sample exhibits nanoparticles with rough edges with wider size distribution.

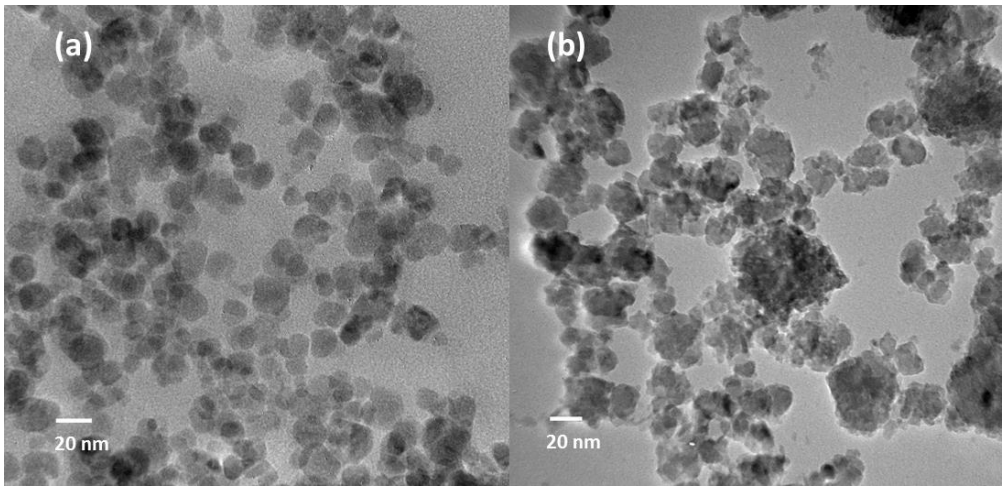

Figure 5.4: TEM images of (a) Fe_3O_4 and (b) Gd doped Fe_3O_4 nanoparticles

5.3: Magnetic Characterization

The M-H data for undoped and Gd-doped Fe_3O_4 ferrofluid samples, recorded at room temperature, are shown in Fig. 5.5. The sigmoidal shape of the M (H) curves with nearly zero hysteresis confirms the superparamagnetic nature of these nanoparticles at room temperature. The saturation magnetization of Fe_3O_4 nanoparticles is measured to be ~ 72 emu/g whereas that of Gd-doped Fe_3O_4 nanoparticles is reduced ~ 52emu/g. This reduction in saturation magnetization at room temperature agrees with the observations in other reported studies

[154,162] and can be attributed to the fact that magnetic Fe^{3+} ions are supposedly getting replaced by the Gd^{3+} ions in the octahedral sites of the inverse spinel structure.

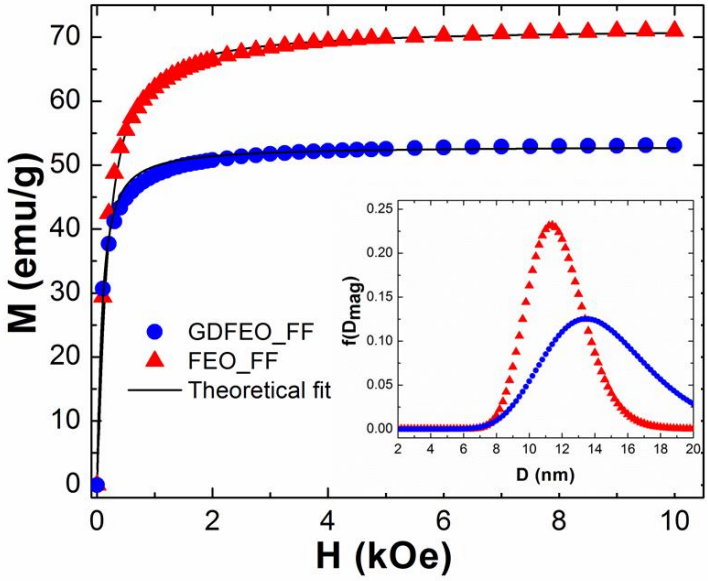

Figure 5.5: M vs H curves for two ferrofluid samples fitted with the particle size distribution incorporated langevin function. The inset shows the resulting particle size distribution of the two samples.

The black lines show the theoretical fit using a Langevin function for the magnetization as a function of *H* incorporating the particle size distribution and dipolar interactions using Eq. 2.11. The inset shows the magnetic core size distributions for two ferrofluid samples. The fitting parameters for the two samples are shown in Table 5.1.

Table 5.1: Fitting parameters obtained from the *M* (*H*) fitting with modified Langevin function

Ferrofluid Sample	**M_s(emu/g)**	**D_0 (nm)**	**λ**	**T^* (K)**	**D_{avg} (nm)**
Fe_3O_4	72	11.6	0.15	80	11.7±1.9
Gd -Fe_3O_4	52	14.2	0.23	100	14.6±3.7

According to the fitting parameters, Gd-doped Fe_3O_4 nanoparticles have a higher average magnetic core size with a larger size distribution (14.6±3.7 nm) compared to the undoped Fe_3O_4 nanoparticles (11.7±1.9 nm). Both the ferrofluid samples exhibit similar strength of magnetic dipolar interaction (T^* ~ 80-100 K).

5.4: Magnetic hyperthermia characterization

MHT measurements were carried out on the dextran coated Gd-doped and undoped Fe_3O_4ferrofluid samples at a field of 235 Oe and at a frequency of 375 kHz. The heating curves for two samples are shown in Fig. 5.6 (a) and from the plot it can be observed that the initial rates of heating for the two samples are roughly the same. From these heating curves the SAR values were obtained as a function of temperature taking into account of heat loss as described in the previous chapter.

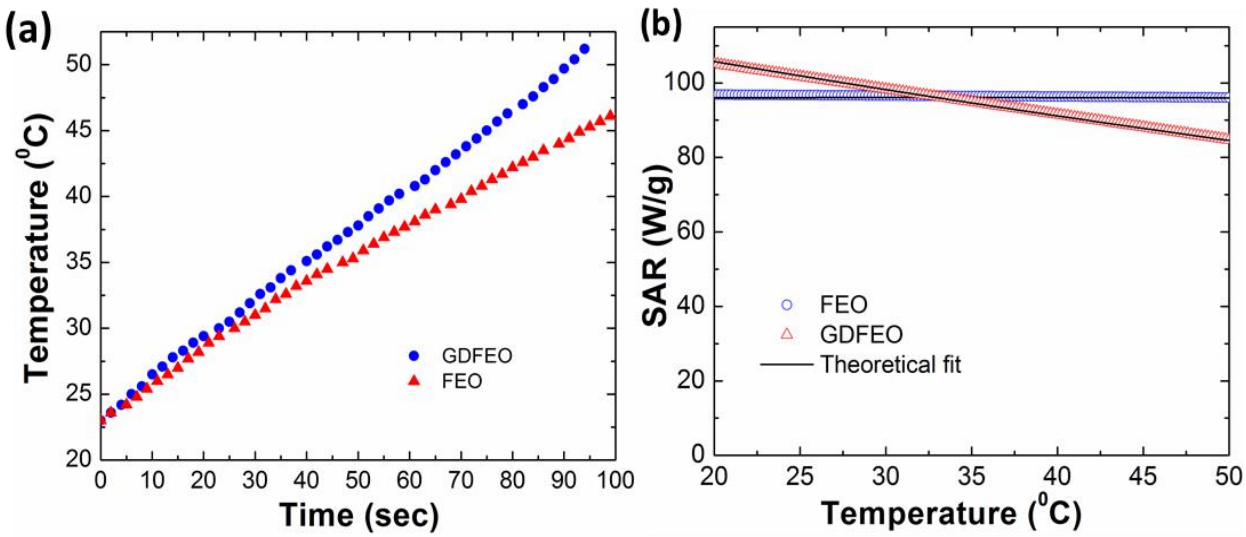

Figure 5.6: (a) Heating curves (Temperature vs time) for Fe_3O_4 and Gd-doped Fe_3O_4 ferrofluid samples under an *ac* magnetic field amplitude of 235 Oe and at a frequency 375 kHz. (b) The temperature dependence of net SAR for two ferrofluid samples. The black line shows the theoretical fitting of the experimental data with the linear response theory.

Figure 5.6 (b) presents the corrected experimental SAR data (symbols) as a function of temperature for both the undoped and Gd doped samples. Within the experimental error, the

room temperature SAR values for Gd-doped $Fe_3O_4$and undoped Fe_3O_4 ferrofluid are very similar. The temperature dependent SAR values were fitted to the linear response theory incorporated with the interactions and size distribution using the expression given in Chapter 2 (Eq. 2.23). The solid lines in Fig. 5(b) are the best fits to the experimental SAR data, using the particle size distribution parameters and T^* values given in Table 5.1and treating the anisotropy constant, *K*, as a fitting parameter. The SAR fitting yields a somewhat smaller anisotropy constant (~ 12 kJ/m^3) for Gd-doped ferrofluid compared to that of undoped ferrofluid (~ 21kJ/m^3).

Figure 5.7 shows SAR as a function of the magnetic core size (D_0) in an AC magnetic field of 235 Oe and a frequency of 375 kHz at 298 K using the fitted values of *Ms*, D_0, and λ obtained from our analysis of M-H (Table 5.1) and K values from MHT fitting of undoped $Fe_3O_4$and Gd-doped Fe_3O_4 ferrofluidsamples.

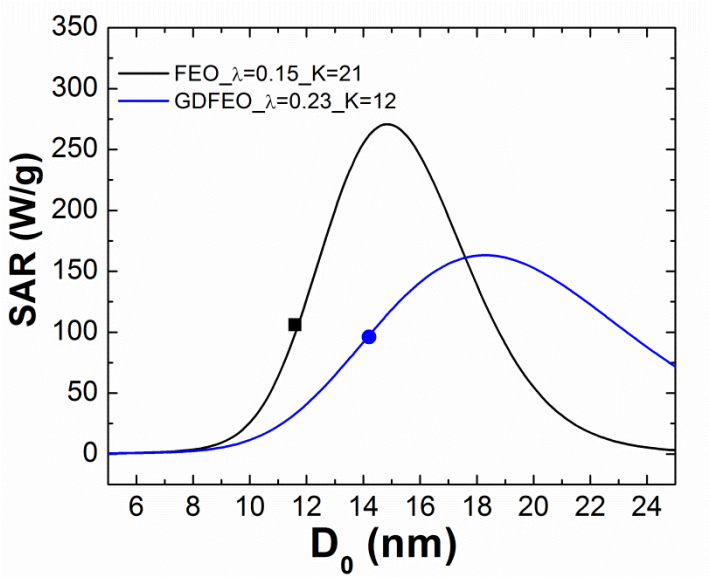

Figure 5.7: Simulated SAR as a function of particle size. The symbols correspond to the experimental data. The parameters used are T = 298 K, H = 235 Oe, f = 375 kHz and values listed Table 5.1.

For the simulation of SAR we used Eq. 4.3 that contains the dipolar interaction modification. The symbols correspond to the experimental SAR obtained for our two ferrofluid

samples. As explained in the previous chapter, SAR increases with D_0 until it reaches a maximum value at a critical size and decreases with further increase in D_0. The larger size distributions broaden the peak reducing the maximum SAR at the critical size. For both of our undoped and Gd-doped Fe_3O_4 samples, the particle size is below this critical size. It is seen here that, the critical sizes at which SAR is maximum shift to a lower value as K increases. Hence by reducing the amount of Gd doping amount it may be possible to obtain a Gd-doped Fe_3O_4 sample with a magnetic core size in between 12-14nm, magnetization and K higher than the values obtained for this Gd-doped Fe_3O_4 sample which will result in a higher SAR than the observed values.

5.5: Conclusions

Gd- doped iron oxide nanoparticles have been synthesized using the simple and widely used co-precipitation method and coated with dextran. The aim of the study was to understand the effect of the Gadolinium doping on the magnetic properties of nanoparticles and the associated magnetic hyperthermia response of the ferrofluids. Hence, the undoped iron oxide nanoparticles synthesized under the same experimental conditions were used as the control. The magnetization data reveals that the saturation magnetization decreases upon Gd doping. M vs H data were fitted with the langevin model incorporated with the log normal size distribution as well as dipolar interactions. Comparing the crystalline sizes (XRD) and magnetic core size distributions obtained from the langevin fitting of two samples, it is observed that Gd doping increases the magnetic core size and causes an increase in the polydispersity of the nanoparticles. Moreover, magnetic hyperthermia measurements were performed on dextran coated ferrofluids and the experimental SAR values (corrected for heat loss) were fitted using the linear response theory. It is evident from the analysis that the magnetocrystalline anisotropy (K) is decreased by

several units upon Gd doping. The reduction in the saturation magnetization and K would generally result in a decrease in SAR but here the increased particle size distribution compensates the negative effect on SAR. Therefore, the obtained SAR value of the Gd doped Fe_3O_4 nanoparticles is similar to that of undoped Fe_3O_4 ferrofluid. Both the samples exhibits the same strength of interactions according to our analysis hence does not exhibit a significant impact on SAR. To conclude, the Gd doping on the Fe_3O_4 nanoparticles affect the morphology and the magnetic properties of Fe_3O_4 nanoparticles considerably but the magnetic hyperthermia efficiency of the samples were about the same within the error limits. By fine tuning the composition of Gd doped Fe_3O_4 nanoparticles, we may achieve a higher SAR value. The possibility of using Gd doped Fe_3O_4 nanoparticles as a dual modal T_1-T_2 contrast agent is being currently explored by others and our magnetic hyperthermia results demonstrate that this material is a potential candidate for theronostics for multimodal contrast imaging and cancer treatment by hyperthermia.

CHAPTER 6 A COMPARATIVE STUDY OF MAGNETIC HYPERTHERMIA AND CYTOTOXITY OF DEXTRAN AND CITRIC ACID COATED Fe_3O_4 NANOPARTICLES

6.1: Introduction

In the design of magnetic nanoparticles for biomedical applications, surface coating plays an important role as it fulfills more than one function at a time. In general, the surface coating is important for three main reasons: First, it provides the colloidal stability of ferrofluids preventing the particle clustering (reducing particle interactions). Second, the coating provides the biocompatibility which is a crucial factor in clinical applications. It ensures a double-sided isolation, preventing any toxic ion leakage from magnetic core into the biological environment as well as shielding the magnetic core from oxidization and corrosion. Third, it serves as a base for conjugating various functional groups such as targeting ligands, therapeutic drugs according to desired application. All these aspects were described in details in Chapter 2. In addition to that, surface coating can endow the nano system with long circulation properties making them "stealth" systems. When nanoparticles are injected into the body during in vivo applications, they are often recognized by reticuloendothelial system (RES) that eliminates any foreign substance from blood stream [163]. In this process, nanoparticles are rapidly attacked by the plasma proteins from RES and shuttled out of circulation to the liver, spleen or kidney which then cleared out from the body. Also this RES accumulation often causes toxicity issues as well. The specific surface coatings can prevent the adsorption of these proteins, increasing the circulation time in blood hence maximize the possibility to reach target tissues [164]. For instance, it is well known that coating of hydrophilic polymers, mainly poly (ethylene glycol) (PEG), on the nanoparticles reduces nonspecific binding of the proteins resulting in stealth behavior.

The effect of the surface coating on magnetic properties and hence on the efficiency of the desired application is still not well understood. Therefore, fine tuning of surface coating materials is a major challenge in current research on the clinical applications of magnetic nanoparticles. During the surface coating on the nanoparticles, coatings molecules interact with the surface atoms of the magnetic core and may form a magnetically disordered layer. This can reduce the total amount of the magnetic phase. Different coatings exhibits different interactions with the magnetic core and therefore produce unique effective nonmagnetic layer thicknesses. However the discrimination between surface coating and finite size contribution is a difficult task especially in the smaller particles where the latter effect is dominant since the volume fraction of disordered surface spins are increased. There are many literature found on different surface coatings on different kind of magnetic cores and the surfactants effect on the magnetic properties [165-169]. In a study reported by Yuan et al. [168], effect of surfactant on magnetic properties was investigated using commercially available aqueous nanoparticle suspensions, FluidMAG-Amine, FluidMAG-UC/A, and FluidMAG-CMX, in parallel with oleic acid covered particles suspended in hexane and heptane. Their results reveal the reduction of magnetic phase in nanoparticles which varies with different coatings as well as with solvents. The magnetic reduction in different coatings was attributed to the different degree of surface spin disorder due to the absorbance of coatings and electric charge whereas the solvent dependent magnetic reduction was attributed to the difference in coating and the magnetic core interaction strengths in different solvents.

The saturation magnetization is a main factor that determines the magnetic hyperthermia efficiency hence the change on the magnetic properties from the surfactant should influence SAR as well. Therefore a useful approach to improve the magnetic hyperthermia performance is to

optimize the surface coating to maximize the SAR. As for now there are conflicting SAR values obtained for a certain sized nanoparticle makes it difficult to evaluate the exact contributions of surface coating on the SAR. The study done by Liu et al [170], reports the possibility of increasing SAR by decreasing the surface coating thickness using highly monodispersed Fe_3O_4 nanoparticles with different mPEG coating thickness. According to his explanation, a decrease in coating thickness lead to an increased Brownian loss, improved thermal conductivity as well as improved dispersibility resulting in increased in SAR. The optimized sample is further tested for magnetic hyperthermia in simulated physiological environments with protein (bovine serum albumin, BSA), blood sugar (dextrose), electrolytes (saline) and phosphate buffered saline (PBS). In another study reported by the same authors, superparamagnetic Fe_3O_4 nanoparticles after coating of Human-like collagen (HLC) show effective heat conduction under an AC magnetic field compared to uncoated sample despite of the slight reduction in saturation magnetization upon coating. According to Mohammad et al it is also found that inorganic coatings improve the SAR value [171]. They found that gold coating retains the superparamagnetic fraction of the superparamagnetic Fe_3O_4 nanoparticles much better than uncoated nanoparticles alone and leads to higher magnetocrystalline anisotropy. In another study done by Filippousi et al. [165], authors use three diverse (different molecule length, polar head group and charge) and widely used surfactants, cationic cetyltrimethylammonium bromide (CTAB) surfactant, the nonionic polyvinylpyrrolidone, K30 (PVP) surfactant, and the anionic sodium cholate (S.C.) surfactant to investigate their possible influence on the magnetic properties and the heating response. Their results show that CTAB coated sample yields a lower magnetization (29.8 Am^2 /kg) compared to the rest of the samples (~ 50 Am^2 /kg) due to its more prominent oxidation and shows the lowest SAR among all samples.

In our study presented in this chapter, we investigated the effect of surface coating on temperature dependent SAR using two biocompatible surfactants dextran and citric acid (CA). To compare the effect of coating, we used the same batch of Fe_3O_4nanoparticles for coating (post-synthesis coating) and studied the structural and magnetic properties as well as the colloidal stability of the dispersions. We also examined the influence of surface coating by systematically investigating the SAR of ferrofluids in slightly basic water solution as well as in simulated physiological environments with protein (bovine serum albumin, BSA).

6.2: Characterization of dextran and citric acid coated Fe_3O_4 ferrofluids

The Fe_3O_4 magnetic nanoparticles were synthesized using the chemical co-precipitation route, as described in Section 3.1.1. The synthesized nanoparticles were then coated with dextran and CA based on the procedure outlined in Section 3.2.1 and Section 3.2.2.The concentrations of both the ferrofluids were adjusted to 12 mg/mL. The schematic diagram of the surface coated nanoparticles is shown in the figure 6.1.

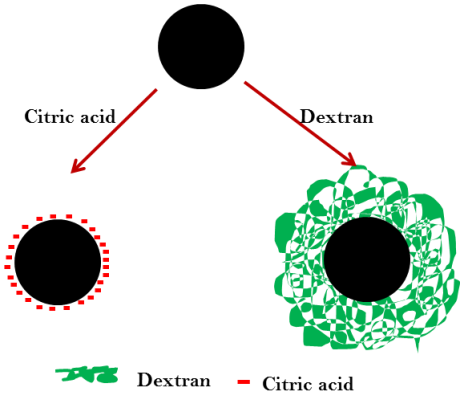

Figure 6.1: Schematic representation of dextran coated and citrate capped Fe_3O_4 magnetic nanoparticle

The phase purity Fe_3O_4 crystalline structure of the as-synthesized nanoparticles was confirmed by the x-ray diffraction and the crystalline size was estimated to be 11.7±0.6 nm from Debye-Scherer analysis (XRD pattern not shown). The morphology of these nanoparticles was

investigated and the particle size distribution was also determined to be 13.2±2.3 nm using TEM as shown in figure 6.2. These obtained values are very similar to that of previous samples prepared for our earlier studies which confirm the reproducibility of the synthesis method.

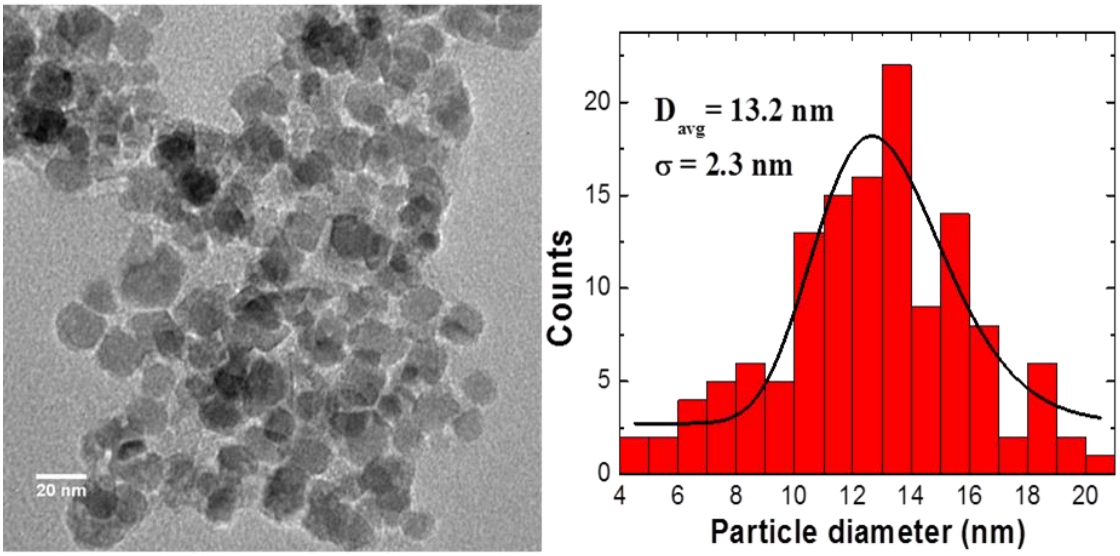

Figure 6.2: TEM images of as prepared $Fe_3O_4$and nanoparticles with the particle sizes fitted to log normal distribution.

The colloidal properties, zeta potential (ξ) and hydrodynamic size (D_H), of the two ferrofluids were characterized using DLS measurements. The hydrodynamic size of dextran coated and CA coated Fe_3O_4 ferrofluids in aqueous media at pH of 7.4 were estimated to be 100 ±25 nm and 30 ± 5 nm respectively. The pH dependent ξ values were measured as shown in the figure 6.3. Both the ferrofluids show negative surface charges indicating their stability over a wide range of pH and the ξ values at pH 7.4 are estimated to be around -17 mV for dextran coated Fe3O4 and -27 Mv for CA coated Fe_3O_4.The large/small value of ξ indicates a more/less electrostatic repulsion between the nanoparticles which opposes the magnetic attraction acting between the nanoparticles. Therefore, our data indicates that, CA provides a higher stability compared to the dextran coating for the whole range of pH.

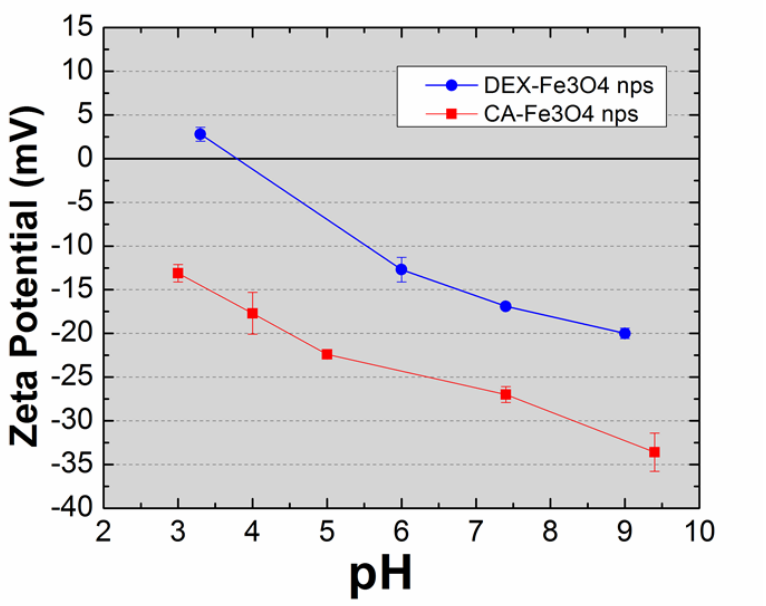

Figure 6.3.pH dependent zeta potentials of different surfactant coated Fe_3O_4 nanoparticles

6.3: Effect of surfactant coating on magnetic properties of Fe_3O_4 ferrofluids

The M (H) curves for both the dextran and CA coated Fe_3O_4 ferrofluids were obtained at 300 K as shown in the figure 6.4. The saturation magnetization of both the ferrofluid samples was similar to the value obtained for uncoated Fe_3O_4 (~ 72 emu/g, reported in Chapter 5) indicating that the surface coating did not affect the magnetization of the sample. However, the magnetic core size of the CA coated ferrofluid obtained from the interaction incorporated Langevin function fitting analysis is slightly lower with a larger size distribution compared to the values obtained for the dextran coated ferrofluid as listed in Table 6.1. Even though we used the same nanoparticles for coating, due to the different reaction conditions and the different coating materials used, the surface of the nanoparticles are modified differently. The interactions parameter, T^*, obtained for dextran and CA ferrofluids are in the range of 60-80K which indicates that both the coating provide excellent stabilityand reduce the inter-particle interactions producing a ferrofluid closer to ideal system.

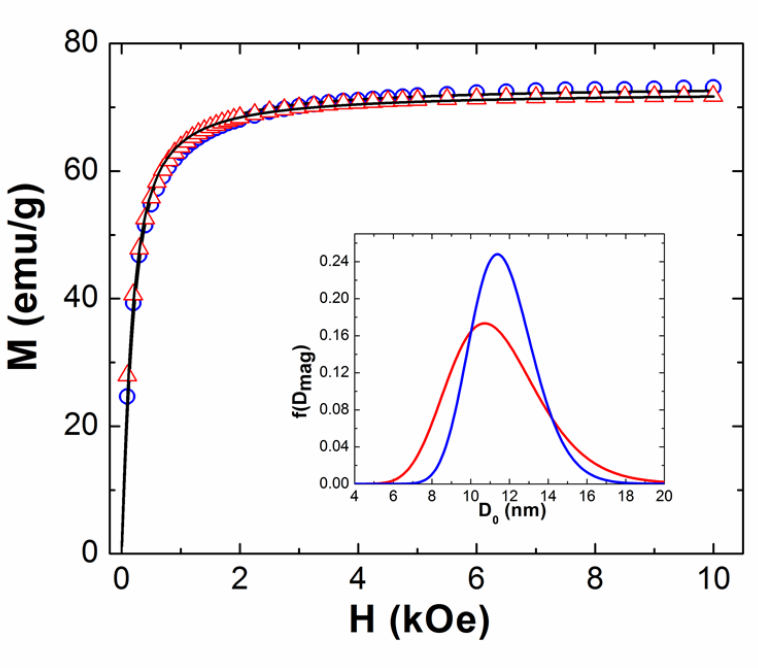

Figure 6.4: M vs H curves for two ferrofluid samples fitted with the modified Langevin function. The inset shows the resulting particle size distribution of the two samples. (red line represents CA coated sample, blue line represents Dextran coated sample)

Table 6.1: Fitting parameters for Dextran and CA coated Fe_3O_4 ferrofluid samples.

	M-H curve fitting				
Ferrofluid Sample	**Ms (emu/g)**	**D_0 (nm)**	**σ**	**T^* (K)**	**D_{avg}(nm)**
Dextran-Fe_3O_4	74	11.6	0.15	80	11.7±1.8
CA _Fe_3O_4	72	11.2	0.21	60	11.5±2.4

6.4: Magnetic hyperthermia of dextran and citric acid coated Fe_3O_4 ferrofluids

The magnetic hyperthermia measurements were made on ferrofluids samples, with 12 mg/ml concentration, using an ac magnetic field of amplitude of 235 Oe and frequency of 375 kHz in the temperature range of 25 - 50 ^oC, as described in earlier chapters. The heating curves and the corresponding plots of SAR as a function of temperature shown in Fig. 6.5 for both dextan and CA coated samples. The initial SAR values of the samples are very similar (105-110

W/g) within the experimental error limits, and it decreases with the increase of temperature. Dextran coated ferrofluid shows a higher decrease in SAR with temperature whereas this decrease is smaller in CA coated ferrofluid. This difference may due to the different size distributions as well as the thermal properties of the two ferrofluids. Using the parameters listed in Table 6.1, we fitted the temperature dependent SAR curves using modified linear response theory to obtain the values of K as a fitting parameter. Interestingly, both the samples yield very similar values 21-22 KJ/m^3.

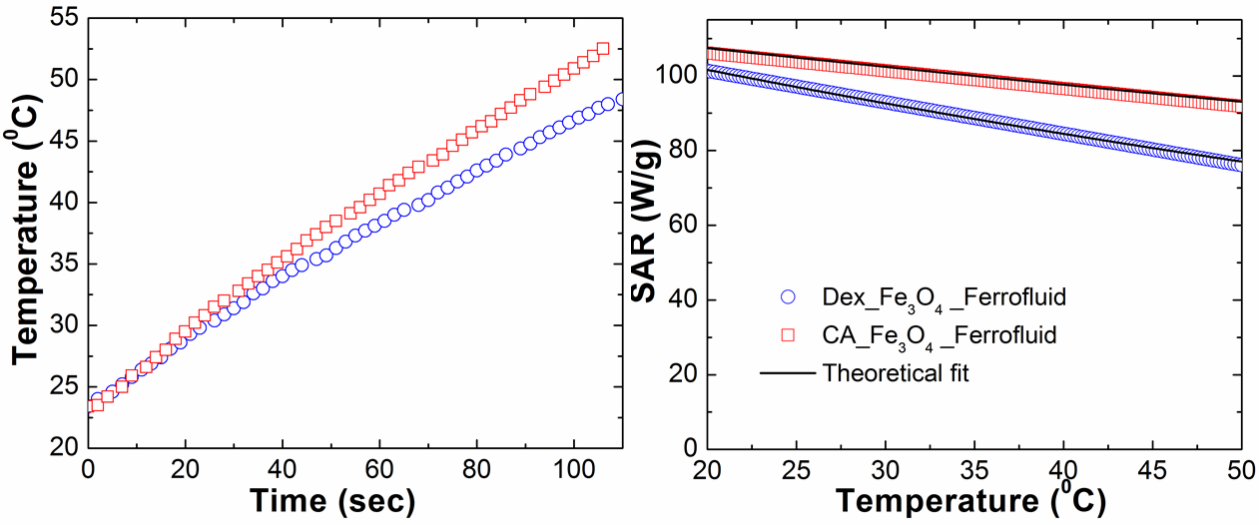

Figure 6.5: Left:Temperature vs time curves for dextran and CA coated Fe_3O_4 ferrofluid samples of 12mg/ml concentration at a frequency 375 kHz and under acmagnetic field amplitude of 235 Oe. Right: The temperature dependence of net SAR for two ferrofluid samples. The black line shows the theoretical fitting of the experimental data with the linear response theory.

6.4.1: Effect of Concentration on the magnetic hyperthermia efficiency

In order to understand the stability of the ferrofluids upon dilution and its effect on the magnetic hyperthermia efficiency, we conducted a series of experiments to measure the SAR at different concentrations. From the stock concentration of 25 mg/ml, we prepared dilute ferrofluids with concentration of 12mg/ml, 6 mg/ml and 3 mg/ml, using DI water as the solvent. The SAR values obtained for different concentrations of two ferrofluid samples at room

temperature are shown in the Fig. 6.6 (filled symbols). A decrease in SAR was observed upon dilution for both ferrofluids. In general, it has been observed that a decrease in concentration would result in an increase in the inter-particles distance, decreasing the dipolar interactions between particles which in turn results in an increase in SAR [172-174]. However the contradictory results obtained from our data may be due to the poor quality of the diluted samples containing clusters/aggregates formed upon dilution. Therefore, when diluting the samples, more precautions might be taken or we could try to dilute with a week base solution.

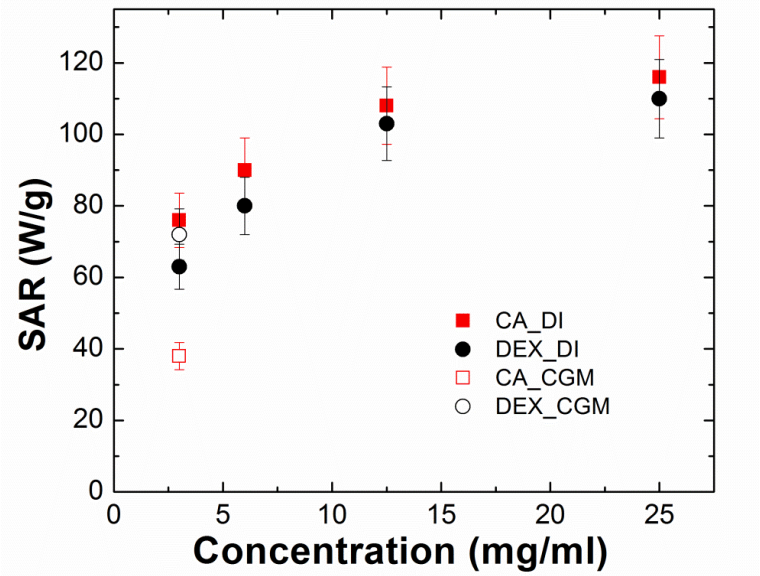

Figure 6.6: SAR values of dextran and CA coated Fe_3O_4 samples at different concentrations at 25 °C. All the data was obtained at a frequency of 375 kHz and ac magnetic field amplitude of 235 Oe.

6.4.2: Effect of the solvent media on the hyperthermia efficiency

Whenever nanoparticles encounter biological systems, interactions take place between their surfaces and biological components such proteins, membranes, phospholipids, DNA forming so called “protein corona” around the nanoparticles [175,176]. Upon the exposure, faster binder interacts with the nanoparticle surface forming the initial corona, however they eventually are replaced by proteins with the highest affinity to the surface (Vroman effect) [177]. The initial corona formed on short time scales (seconds to minutes) is called “soft” corona whereas the one

that forms in later times over period of hours is called “hard” corona. The adsorption of serum proteins on the nanoparticles surfaces in a biological system has been widely studied, often focusing on the effect on cell uptake and cytotoxicity of the particles [178-181]. The formation of corona depends on the surface properties of the particles [182,183] and can influence the aggregation behavior of nanoparticles in biological media, which in turn can affect their performance for desired applications. Therefore, apart from the optimization of the properties of the magnetic core and surface coating for high performance magnetic hyperthermia, it is necessary to ensure its performance in the physiological environments. In the work reported by Khandhar et al [184], authors use poly(maleic anhydride-alt-1-octadecene)-poly(ethylene glycol) (PMAO-PEG), an amphiphilic polymer coated Fe_3O_4nanoparticles of three different sizes, 13 nm, 14nm and 16 nm, to study the magnetic hyperthermia efficiency in cell growth medium (CGM) similar to biological environment. Their results show an increase in hydrodynamic sizes in all three samples upon exposure to CGM. SAR is reduced (30%) only in 16 nm size sample while other two samples did not exhibit any significant decrease in SAR. Authors suggest that the increase in hydrodynamic volume prolongs Brownian relaxation while Neel relaxation is unaffected. Hence in 13 and 14 nm samples where SAR is mainly due to Neel relaxation, SAR was not affected. But in 16 nm samples, in which there is a contribution from Brownian relaxation to heat dissipation, the SAR dropped due to the increase in Brownian relaxation.

We investigated the magnetic hyperthermia efficiency of dextran and CA coated Fe_3O_4i ferrofluids in cell growth medium which contains serum proteins similar to physiological environments. From the stock solutions (25 mg/ml), 3mg/ml concentration of dextran and CA coated ferrofluids samples were prepared using cell growth medium (CGM) and DI water. The ferrofluid samples were subjected to an alternating magnetic field of amplitude, 235 Oe and the

frequency of 375 kHz and the time dependent temperature was measured followed by the analysis described in the earlier chapter. The SAR of dextran coated samples in DI and CGM were estimated to be 63 W/g and 72 W/g respectively which indicate that their performance is not much affected by the medium if not enhanced. However, SAR values obtained for CA coated samples in DI and CGM, 78 W/g and 38 W/g, implies that their efficiency is heavily reduced when exposed to physiological environments. The summary of the results of solvent dependent SAR is shown in figure 6.6.

In order to explore the reason for this reduction of hyperthermia efficiency in CGM, we measured the hydrodynamic sizes of dextran and CA coated ferrofluids samples at different incubation times from few minutes to 24 hours upon exposure to CGM. As seen from the measured values, the hydrodynamic sizes of both the ferrofluids are increased, each at different rates (see Fig 6.7). The increase in the sizes can be attributed to the formation of protein corona upon the nanoparticle exposure to the serum proteins in CGM. Dextran and CA coating endow the nanoparticles surface with different surface chemistries. For example CA coating provides the more active carboxyl functional groups making the surface hydrophilic andincreasing the electrostatic repulsion between the particles. On the other hand, dextran coating has hydroxyl groups, and interactions between the particles are reduced mainly due to steric repulsion than electrostatic repulsion. When CA coated Fe_3O_4 is exposed to serum proteins, the proteins rapidly bind to their surface forming a protein corona. As a result its hydrodynamic size increases quickly and reaches to the maximum value within 5 hours. This in turn reduces the stability of the ferrofluid, leading the particles to form aggregates reducing the SAR value.

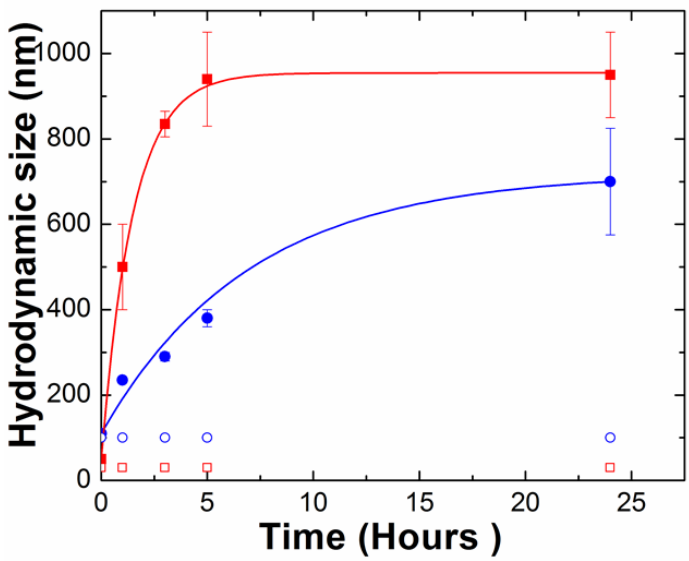

Figure 6.7: Hydrodynamic sizes of dextran and CA coated Fe_3O_4 samples at different times at 25 °C. Red symbols represent CA coated sample, blue symbols represent Dextran coated sample. Closed symbols are for ferrofluids diluted using CGM and open symbols are for ferrofluids diluted with DI.

Compared to CA coated particles, dextran coated nanoparticles show much stability at least during first 3 hours upon exposure to the serum proteins. The formation of the corona takes place at a slower rate which may due to the steric hindrance and the low activity of hydroxyl groups. Therefore its hyperthermia efficiency is not reduced as in CA coated Fe_3O_4 sample. A schematic representation of the protein corona formation is shown in Fig. 6.8. However, when analyzing the data obtained from hydrodynamic size measurements, it should also be noted that not only the protein corona but also free-protein clusters are likely to influence the results.

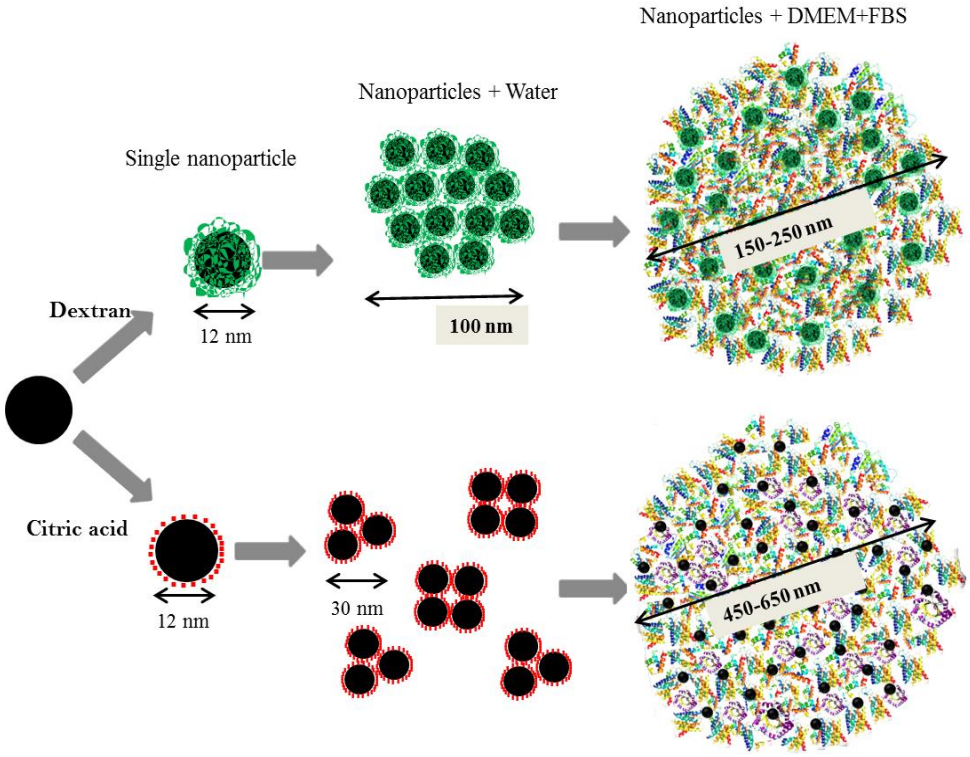

Figure 6.8: Sketched evolution of the nanoparticle agglomeration process when in contact with protein-rich medium such as DMEM + FBS

6.5: Cytotoxicity studies on human pancreatic cancer cells

As mentioned earlier, one of the basic and an important requirement that should be fulfilled by nanoparticles for them to be used for biomedical applications is the non-toxicity. We tested the cytotoxicity of dextran and CA coated Fe_3O_4 ferrofluids by performing trypan blue exclusion technique [185], an established cytotoxicity protocol, followed by cell counting using hemocytometer [186] on human pancreatic cancer cells, Mia PaCa 2. Same amount of MIA PaCa-2 cells were seeded in 100 mm dishes containing 10 ml of cell growth medium (10% fetal bovine serum,5% penicillin in Dulbecco's modified essential medium),and were incubated for 24 hours at 37 °C in a humidified 5% CO_2 atmosphere in order to make cells attached to the bottom of the culture plate. Then half of the medium was replaced with the fresh medium containing dextran and CA coated Fe_3O_4 ferrofluids of 200 µg/mL concertation which makes the final

concentration 100µg/mL in each dish. Fresh cell growth medium without nanoparticles were used for the control experiments. After incubating the cells with the nanoparticles coated with dextran and CA for 24 and 48 hours, the supernatant was taken out and stored in a corning flask. This supernatant contains any dead cells that are detached from the cell bottom. Then 2 ml trypsin was added, incubated for 3 minutes in the incubator followed by the addition of the cell growth medium. This cell solution was mixed with the corresponding supernatant that was stored previously. Now the cells were centrifuged at 1500 rpm for 3 minutes, supernatant was removed and the cell pellet was dissolved in 2ml of cell growth medium. Out of the concentrated cell suspension, 100 µL was taken and mixed with 100 µL of 0.4% trypan blue solution. Then 10 µL of the resultant solution was loaded on a hemacytometer and examined immediately under a microscope at low magnification. The cells that are dead or non-viable will take up trypan blue, result in blue color. The number of blue staining cells and the number of total cells were counted to estimate the cell viability using the Eq. 6.1. The experiments were done in triplicates.

$$\% \text{ viable cells } = \left[1 - \frac{\text{Number of blue cells}}{\text{Number of total cells}}\right] \times 100\% \qquad (6.1)$$

According to the results, both the cells that are exposed to dextran and CA coated Fe_3O_4 nanoparticles show the same viability as the normal cells that are not exposed to the nanoparticles. This indicates that at the concentrations of 100 µg/mL or lower, nanoparticles coated with dextran and CA do not show any toxic effect on the cells. The cytotoxicity results are shown in the Figure 6.9.

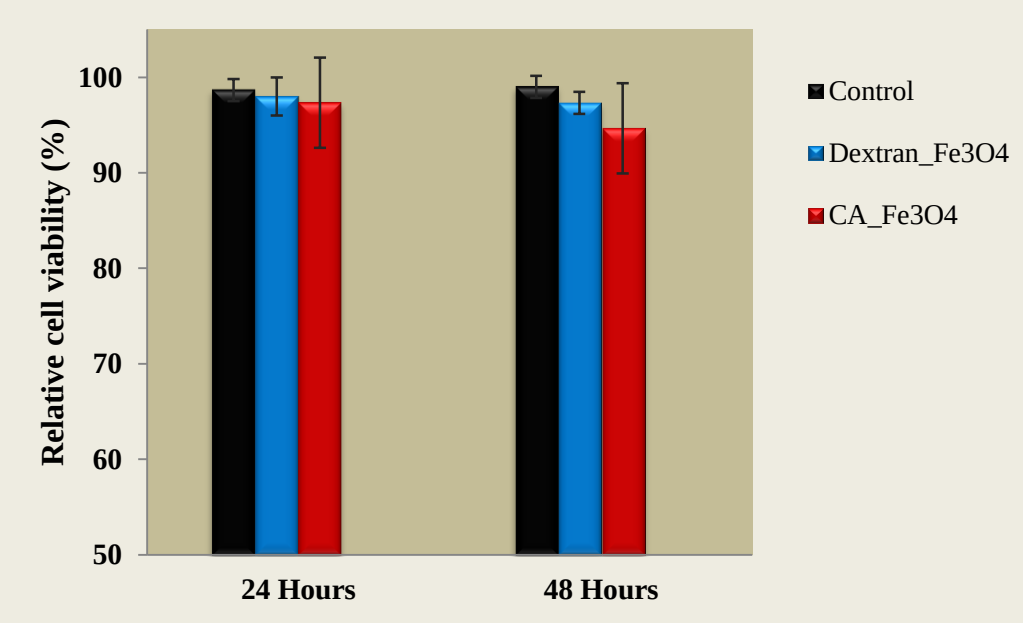

Figure 6.9: Cytotoxicity for dextran and CA coated Fe_3O_4 nanoparticles on Mia PaCa 2 cells as determined by counting live cells using Trypan Blue assay. Experiments were conducted in triplicate with n = 3. Error bars represent the standard deviation.

6.6: Conclusions

In this study we investigated the effect of two coatings, dextran and CA, on the colloidal and magnetic properties of Fe_3O_4nanoparticles as well as their impact on magnetic hyperthermia efficiency. Both the ferrofluids (dextran and CA coated) show similar magnetic properties, with same value of SAR in DI water. Our concentration dependent magnetic hyperthermia results indicate that the dilution of the sample should be done with extensive care as it may promotes cluster formation which in turn reduces the SAR value. Moreover, upon exposure to cell growth medium that mimics the physiological environment, formation of corona was observed for both dextran and CA coated nanoparticles as seen from the hydrodynamic size measurements. It was observed that in CA coated particles where, this protein corona forms faster, in several minutes to hours, that causes aggregations in solution which in turn reduce SAR by ~ 45%. But dextran coated nanoparticles show a better stability at least within first 3-6 hours upon exposure to the proteins in the cell growth medium exhibiting excellent performance in both water and simulated

physiological conditions. The cytotoxicity studies done on human pancreatic cancer cells indicate that both dextran and CA coated Fe_3O_4 ferrofluids are nontoxic to the cells at or below 100 µg/mL concentration. Though further in vivo study is necessary in the future, these results imply that the dextran coated Fe_3O_4 dispersion could maintain their high heating capacity in physiological environments while CA coating require further surface modification to reduce the non-specific protein adsorption.

CHAPTER 7 TIME-DEPENDENT CELLULAR UPTAKE AND DISTRIBUTION OF DEXTRAN-COATED IRON OXIDE NANOPARTICLES

7.1: Introduction

Aa mentioned in the earlier chapters, superparamagnetic Fe_3O_4nanoparticles (SPIO) are currently one of the most important and acceptable nanoparticles since they can be multi purposely used such as for imaging, targeted drug delivery, magnetic hyperthermia, and cell separation with external magnetic manipulation [49,187-189]. Fabricating a biocompatible, well dispersed, stable colloidal dispersion of the nanoparticles with good magnetic properties is crucial for clinical applications and intensive research continue to be carried out to further improve the biocompatibility and dispersibility. Nanoparticles in the range of 10-200nm are generally considered to be ideal for the biomedical applications since they are taken up by the liver and spleen for clearance from the body. The cellular uptake, bio distribution, molecular response and the potential toxicity of the SPIO nanoparticles are mostly based on the particles size, physical shape, and surface chemistry [190]. Importantly, these cellular responses also depend on the cell type [191].

Although, extensive studies have been carried out on the synthesis, biocompatibility, surface modifications [190,192-195], cytotoxicity [196-198], and the *in vivo* targeting of Fe_3O_4nanoparticles, a complete understanding of their interaction and subcellular distribution in cells is yet to be fully realized. In present study, we have determined the traffic, distribution, and the cytotoxic effects of the dextran coated Fe_3O_4 nanoparticles on Mia PaCa 2, human pancreatic cancer cells. The mass spectroscopy was used as the tool to investigate the time dependent distribution of the nanoparticles.

7.2: Synthesis and characterization of Fe_3O_4 nanoparticles

Fe_3O_4 nanoparticles were synthesized by the co-precipitation technique as described in section 3.1.1 with slight modifications. Here, the aqueous solution of Fe^{2+} / Fe^{3+} was kept under constant magnetic stirring at 800rpm and 125 ml of 2M NH_4OH solution was added drop wise into the mixture. The nanoparticles were isolated with a magnet and washed several times with deionized water until a neutral pH was reached. The portion of synthesized nanoparticles was air dried and the resulting powder was used for the structural and magnetic characterization. The XRD pattern for the bare Fe_3O_4 nanoparticles is shown in Fig 7.1.

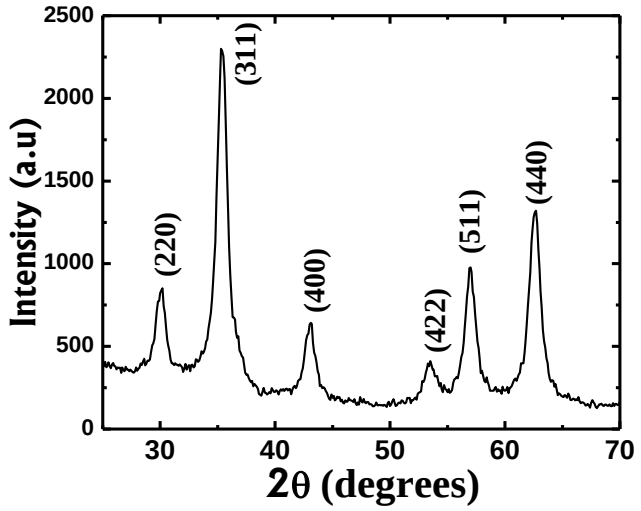

Figure 7.1: XRD pattern of synthesized 8 nm size Fe_3O_4 nanoparticles. Sample was deposited on a glass substrate from acetone dispersion. Diffraction pattern was collected on a Rigaku MiniFlex 600 X-ray diffractometer under CuKα radiation (λ = 1.5418 Å).

The peaks observed in this pattern were consistent with those of standard XRD pattern of Fe_3O_4 reported previously (reference JCPDS No. 82-1533) which confirms crystalline nature of the synthesized Fe_3O_4 nanoparticles with Face centered cubic structure. Also, the absence of any unknown peaks confirms that there are no secondary phases formed and there is no significant presence of crystalline impurities in the sample. The crystalline size of MNPs was estimated to

be 7.2±0.8 nm by the use of Debye-Scherer's equation. TEM images of the IONPs (Fig. 7.2) reveal that the nanoparticles are spherical with a narrow particle size distribution. To determine the particle size distribution, the sizes of the particles from multiple images were measured, and the obtained sizes were sorted into a histogram, and the histogram data was fitted to a log-normal distribution function as described in the earlier chapters. The histogram and the lognormal fits are shown in the inset of Fig. 2. The average particle size and the standard deviation of the distribution were estimated to be 7.7 nm and 1.7 nm respectively.

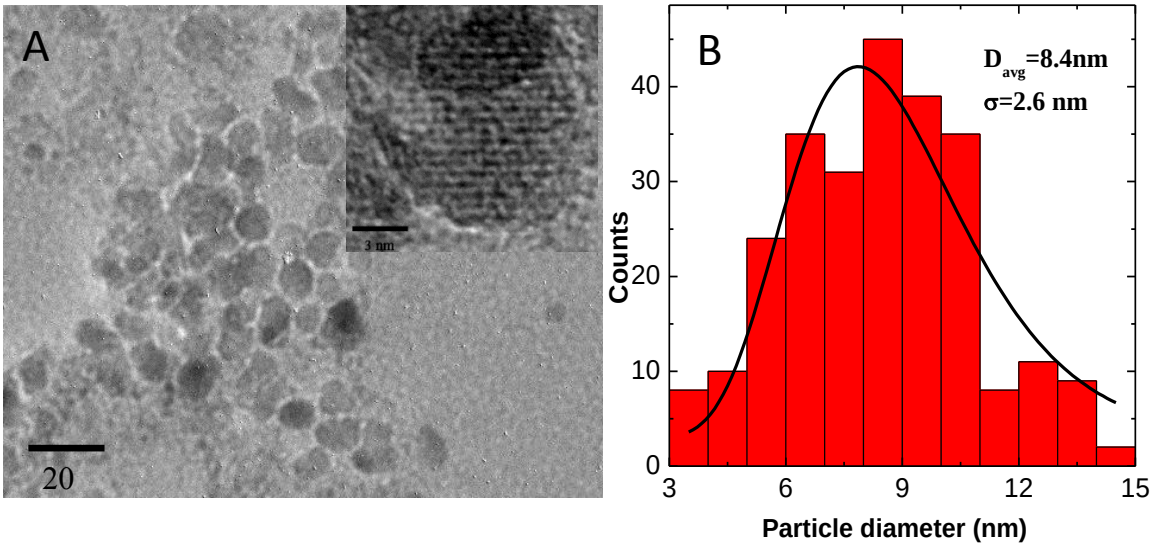

Figure 7.2: TEM Image of bare Fe_3O_4 nanoparticles (A), size distribution plot with log normal fitting (B).

M (H) curve shown in Fig. 7.3 demonstrate superparamagnetic behavior (no coercivity).

M (H) curve shown in Fig. 7.3 demonstrate superparamagnetic behavior (no coercivity).The saturation magnetization of the Fe_3O_4 nanoparticles at 300 K was found to be 61 emu/g with a maximum applied field of 10 kOe, which is lower than the reported values of bulk Fe_3O_4 (92 emu/g)[199]. The reduction in saturation magnetization may be attributed to the surface disorder or spin canting at the particles surface [139].

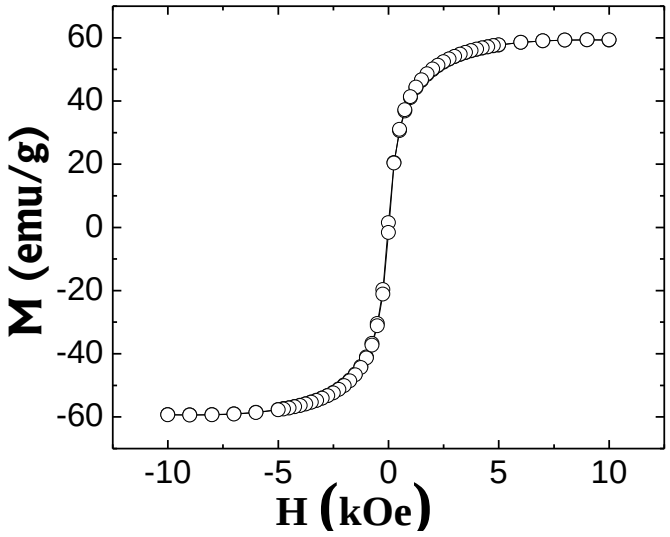

Figure 7.3: M (H) curve for 8 nm Fe_3O_4 nanoparticles at 300 K demonstrating the superparamagnetic behavior with saturation magnetization of 61emu/g.

7.3: Conjugation of FITC to dextran-functionalized Fe_3O_4 nanoparticles

The synthesized nanoparticles were then coated with dextran to obtain the well suspended ferrofluid and cross linked using epichhlrohydrin according to the detailed description presented in Section 3.2.1 and 3.2.3 respectively. Conjugation of FITC to dextran-functionalized nanoparticles was carried out using an established published procedure[200] , details of which is presented in Section 3.2.4.

7.4: MIA PaCa-2 cellular studies

To investigate the interaction between cells and the synthesized Dex-Fe_3O_4-FITC nanoparticles, MIA PaCa-2 cells were exposed to them and the cellular uptake, distribution, and cytotoxicity were evaluated as described here. MIA PaCa-2 human pancreatic cancer cells were grown on poly L-lysine-coated petri dishes in Dulbecco's modified essential medium (DMEM) containing 10% fetal bovine serum (FBS) and 5% Penicillin-Streptomycin. Approximately, 5×10^4 MIA PaCa-2 cells were seeded in 35 mm dishes containing 2 ml of DMEM-10% FBS-5% Penicillin-Streptomycin, were incubated for 24 hours at 37°C in a humidified 5% CO_2

atmosphere. After 24 hours, half the medium was removed, and replaced with fresh medium containing FITC labeled Dextran coated SPIO nanoparticles so that the final concentrations are 0, 5 µg/ml, 50 µg/ml, 125 µg/ml. Cells were imaged using an Olympus FSx100 fluorescence microscope in the green channel (excitation at 485 nm, emission at 530 nm). Fluorescence images of the cells were taken at different time intervals: 0 hour, 6 hours, 24 hours and 48 hours. After 48 hours, cells were washed three times with PBS solution to get rid of unbound nanoparticles, trypsinized, centrifuged, and 5×10^4 of cells were cultured in new 35 mm dishes. These cells, in which nanoparticles are internalized, were incubated at 37 °C in a humidified 5% CO_2 atmosphere for another 3 days. After 3 days, the old medium was replaced with fresh medium, followed by imaging. Experiments were performed in triplicates.

The fluorescence images taken at different time intervals such as at 0h, 24hour, 48 hours are shown in Fig. 7.4, and the increase in the fluorescent signals over time demonstrates increased accumulation of the FITC functionalized SPIO in cells. According to the images, the SPIO nanoparticles were internalized within cells during 48 hours of incubation at 37°C. The SPIO nanoparticles were shown to exhibit dose dependent cytotoxicity and shown to be safe up to the concentration level of 100 µg/ml on human cells [201]. Interestingly, even after 3 days of incubation (Fig. 7.5), nanoparticles were still present in the cells. The presence of the nanoparticles within the cells clearly indicates the inheritance of the nanoparticles from the parent cells during cell division. Also at this time point, the cells incubated with 125 µg/ml of SPIO show a significant decrease of cell number, which may be due to the inhibition of cell division caused by the prolonged accumulation of nanoparticles.

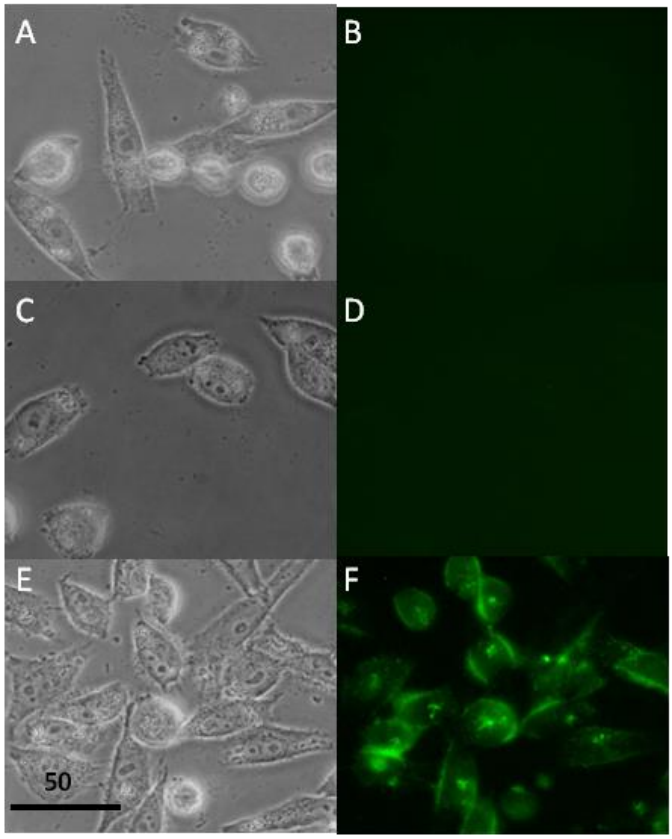

Figure 7.4: Images demonstrating the time-dependent binding and accumulation of FITC functionalized dextran coated SPIO nanoparticles with cultured MIAPaCa2 cells. Top to Bottom: 0h, 24h, and 48h. Phase images of cells (a), (c), (e), Left to right: corresponding fluorescent images. (b), (d), (f).

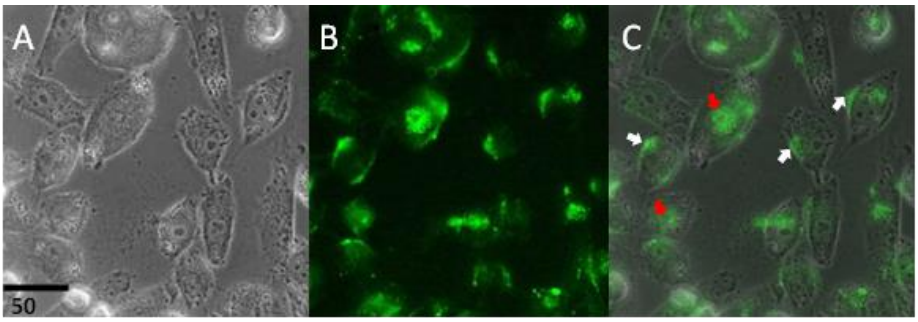

Figure 7.5: Phase image (a), fluorescent image (b), of cells showing the presence of FITC conjugated dextran coated SPIO nanoparticles within the cells after 3 days of accumulation indicating the inheritance of nanoparticles from parent cells to daughter cells during cell division. Overlaid image of phase and fluorescent images (c) demonstrate that most of the nanoparticles are at the membrane (white arrow heads) while small amount can be seen in the nuclei (red arrow heads).

In agreement with the literature, there was no evidence of cytotoxicity observed in our data during the first 48 hours as shown in Fig.7.6.

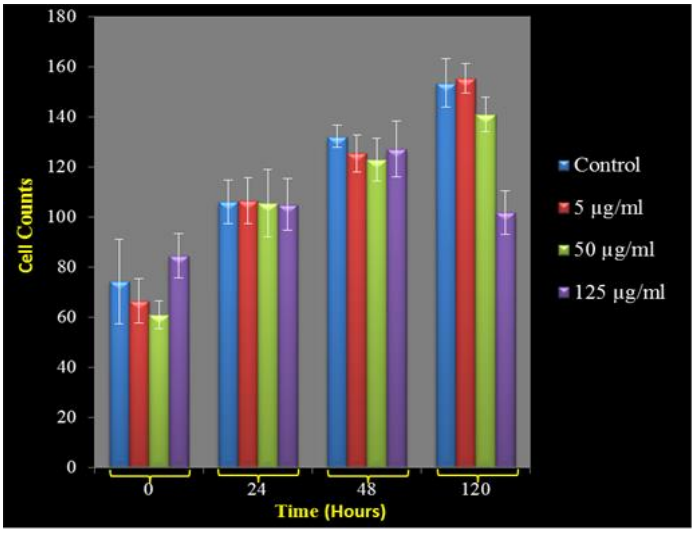

Figure 7.6: Cytoxicity results for dextran-FITC coated SPIO nanoparticles on MIA PaCa2 cells at three different concentrations. Note that cells were washed at 48 hours to remove unbound nanoparticles and were incubated for another 3 days.

7.5: SDS-Page

In order to study the time dependent binding of the specific proteins the experiments were carried out as following. Cells were lysed using 2% Triton, centrifuged for 1 minute at 1000rpm. The supernatant was removed and the pellet containing nanoparticles bound proteins was washed using PBS pH 7.4. The nanoparticle-associated proteins were resuspended in Laemmli [15] reducing sample preparation buffer, boiled for 2 min, and used for SDS-PAGE. SDS Polyacrylamide Gel Electrophoresis (SDS-PAGE) was run in order to separate nanoparticles bound proteins based upon their size. The gels were then stained using Coomassie Blue overnight, de-stained for 3-4 hours and imaged.

Assessment of the protein profile associated with the nanoparticles from SDS-PAGE, at different times following incubation with cells, demonstrates a time-dependent distribution and

association of the nanoparticles with different cellular compartments as reflected from their different protein profiles (Fig. 7.7).

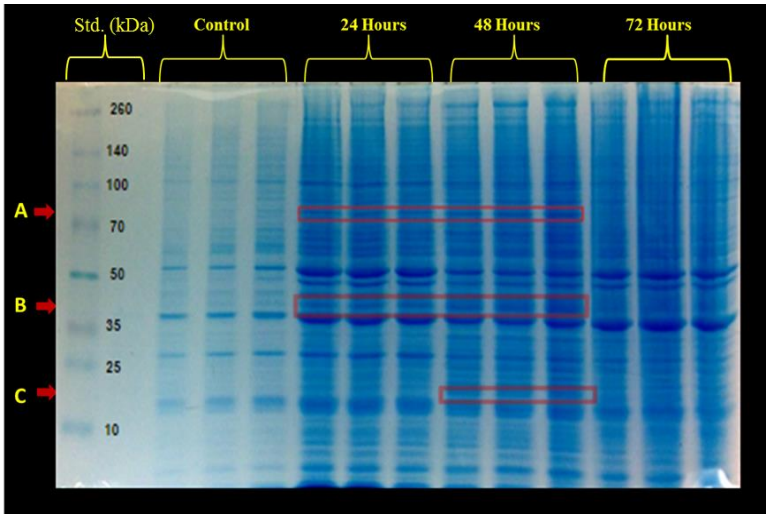

Figure 7.7: Coomassie stained SDS page gel image of protein bands associated with Fe_3O_4 nanoparticles at different time points.

The SDS-PAGE demonstrates differences in some of the protein bands which change with time, and are shown as A, B, C. The bands A and B are seen in 24 and 48 hours but not before or after thatwhereas the band C appears only at 48 hours, suggesting association of the nanoparticles with different subcellular compartments at different times following exposure to cells.

7.6: Mass Spectroscopy data

Mass spectrometry was performedto identify the proteins associated with thebands observed from SDS page gel. One of the gel bands (Band B in Figure 7.7) which showed different optical densities at different time points during 0-72 hour time interval was selected. The corresponding band of the control and the experimental samples at each time point was cut and prepared for mass spectroscopy measurements. The proteins associated with these gel bands were identified and the proteins present at different time points are listed in Table 1.

Table 7.1: List of proteins that are bound to the nanoparticles at different time points as identified by mass spectrometry. The sub cellular organelles associated with each protein are listed in the right column revealing the possible location/distribution of the nanoparticles after been exposed into the cells.

	Protein	Sub cellular organelle
24 hours	Flotillin-2	Cell membrane, Endosome
	Actin-like protein 6A	Nucleus
	Septin-7	Cytoplasm
	DnaJ homolog subfamily A member 1	Membrane, Nucleus, Cytoplasm
	Nucleoporin Nup43	Nucleus, Chromosome
48 hours	Glutamate receptor ionotropic, delta-2	Cell membrane
	Heterogeneous nuclear ribonucleoprotein H	Nucleus › nucleoplasm
	RuvB-like 2	Nucleus, cytoplasm, membrane
	Eukaryotic translation initiation factor 2 subunit 3	Cytoplasm
	Pigment epithelium-derived factor	Melanosome, Secreted
	Wnt inhibitory factor 1	Secreted
72 hours	Cytochrome b-c1 complex subunit 1, mitochondrial	Mitochondrion inner membrane
	Ubiquitin-60S ribosomal protein L40	Cytoplasm, Nucleus
	Actin, aortic smooth muscle	Cytoplasm › cytoskeleton
	Cathepsin D	Lysosome
24 & 48 hours	Protein DEK	Nucleus
	Polymerase delta-interacting protein 3	Nucleus. Nucleus speckle. Cytoplasm
	Cell growth-regulating nucleolar protein	Nucleus
	Protein MAK16 homolog	Nucleus › nucleolus
	Ribosome production factor 1	Nucleus › nucleolus
	DDB1- and CUL4-associated factor 13	Nucleus › nucleolus
	WD40 repeat-containing protein SMU1	Nucleus. Cytoplasm
	Core histone macro-H2A.1	Nucleus. Chromosome
	26S protease regulatory subunit 7	cytoplasm, Nucleus

Data reveals the possible entrance of nanoparticles through endocytosis and targeted to the cell nuclei within 48 hours. At 72 hours Cathepsin D , which is present in the lysosome, was identified which suggests that the clearance of the nanoparticles through the lysosome does not occurs immediately after the entrance, instead proves the prolong accumulation of the nanoparticles in the cells.

Also we determined the distribution of nanoparticles within cells at different time points from the protein data and shown in Figure 7.8. From that also it can be observed that nanoparticles are present in the nucleus within 24 hours and the clearing occurs only after 48 hours, since the relative percentage of proteins associated with nanoparticles has decreased at 72 hours.

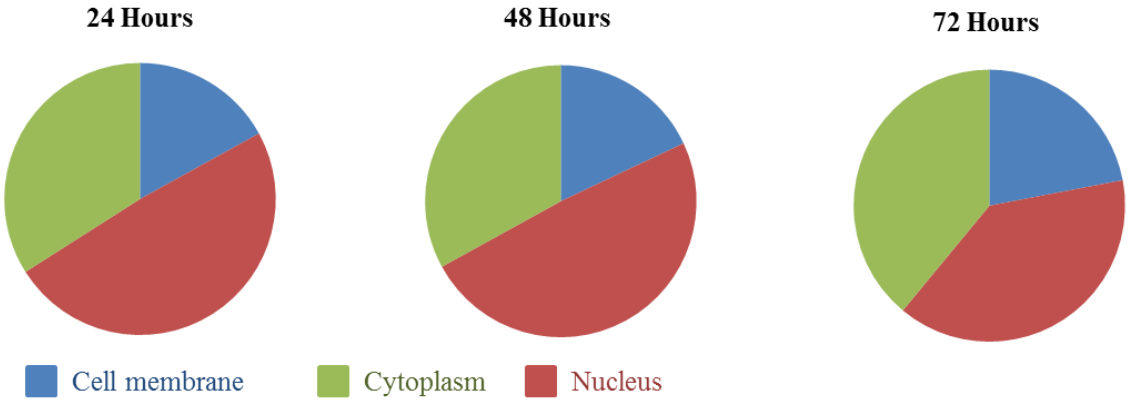

Figure 7.8: Schematic representation of distribution of Fe_3O_4 nanoparticles within cells at different time points estimated from the mass spectroscopy data.

7.7: Conclusions

In summary, the current study we have successfully functionalized nanoparticles for use in investigating their binding and distribution in Mia PaCa-2 human pancreatic cancer cells. We have investigated the traffic, distribution, and cytotoxicity, associated with these Fe_3O_4 nanoparticles, and demonstrated that there is a time-dependent distribution of these nanoparticles into different cellular compartments. Furthermore, immunocytochemistry using co-localization

of the nanoparticles with specific subcellular immune-markers is being carried out to further confirm results from mass spectrometry. Results from these studies promise optimized drug delivery and treatment of various diseases including cancers.

CHAPTER 8 SUPERPARAMAGNETIC IRON OXIDE NANOPARTICLES POTENTIATE CELLULAR ENTRY AND RELEASE OF CANCER DRUG

8.1: Introduction

The various properties of nanoparticles (NPs) have been extensively explored for they offer a broad spectrum of usage ranging from applications in electronic materials to medical therapy [202]. In the last decade, gold [203,204], silver [205,206] and magnetic nanoparticles [207] especially iron oxide emerged as potential candidates for the diagnosis and treatment of various forms of cancer. The interaction of these NPs with cancer cells is widely studied for careful understanding of several drug delivery and therapeutic approaches [208-210]. The Fe_3O_4 NPs [211] with their very unique superparamagnetic behavior play a prominent role in modernizing the field of nanomedicine [190,212-214]. Several modifications including surface functionalization of these Fe_3O_4NPswith anti-cancer drugs especially doxorubicin (Dox) have been conducted over the last few years to investigate their efficacy when it comes to cancer eradication [215]. Previous studies have reported that PEG (Polyethylene Glycol) functionalized porous silica shell onto doxorubicin-conjugated Fe_3O_4 nanoparticle cores [216], PAMAM (Poly(amidoamine)) coated Fe_3O_4 nanoparticles-doxorubicin complex [217], doxorubicin loaded Fe_3O_4 nanoparticles modified with PLGA-PEG copolymers [218] could potentially be very promising in therapeutic cancer treatment. Pancreatic cancer, a very devastating form of cancer, is one of the major causes of death in the United States [219]. Dox conjugated NPs have been extensively used for efficient drug delivery especially in human breast cancer cells. The anti-cancer drug Dox and the targeting ligand conjugated to the surface of a polymeric nanoparticle works effectively for drug delivery in the human breast cancer cells. However, interaction of nanoparticles with the human pancreatic cancer cell lines is not much explored. So a detailed

investigation to understand the interactions and the intracellular distribution of these nanoparticles into the human pancreatic cancer cells is very crucial.

In this chapter, we primarily present our work on the novel conjugation of Dox with a labeling dye (FITC) onto dextran coated Fe_3O_4 nanoparticles using existing EDC/NHS technique and their incorporation into the human pancreatic cancer cell line (MIA PaCa-2) for specific drug targeting. This unique drug-dye dual conjugation of Fe_3O_4 NPs after penetration through the cell membrane following *phagocytosis* [220], show a steady release of Dox into the nucleus of the malignant cells. Our studies demonstrate that association of Dox onto the surface of nanoparticles enhances its penetration into the cancer cells as compared to the unconjugated drug.

8.2: Experimental details

8.2.1: Synthesis and characterization

The superparamagnetic Fe_3O_4 nanoparticles were synthesized coated with dextran and cross linked following the exact procedure as described in Chapter 7.

8.2.2: Double labeling of dextran coated Fe_3O_4 nanoparticles with doxorubicin and FITC (Dex- Fe_3O_4-DOX/FITC)

The pH of the dispersion (10 ml) of crosslinked SPIO NPs having a concentration of 4mg/ml was adjusted to 11 using the NaOH base (0.1 M) under continuous stirring for 1 h at room temperature while purging with N_2 gas. 100mg of monochloroacetic acid (MCA) was then slowly added to the solution and the mixture was heated at 60˚C in a water bath and under N_2 atmosphere. The reaction mixture was then dialyzed against deionized water to obtain the CMD-SPIO. The DOX and FITC were attached to the CMD-SPIO NPs through EDC/NHS chemistry. 10 mg of EDC and 6 mg of NHS was added to 2.5 ml CMD-SPIO NPs suspension and stirred for 15 minutes at room temperature to activate the carboxyl groups. 1µmol of DOX was added to

this mixture and subjected to stirring for 10 minutes, followed by the addition of 1 ml Ethylene diamine hydrochloride (EDA). The resulting mixture was then dialyzed for 24 h to get rid of unbound drug and EDA. 1µmol of FITC solution was added to this amino functionalized CMD-SPIO NPs solution. After 2 h the mixture was subjected to short time interval frequent dialysis. The final concentration of the SPIO NPs in the resulting DOX/FITC conjugated CMD-SPIO NPs (Dex-SPIO-DOX/FITC) was estimated to be 2 mg/ml. All these experiments were carried out in the dark.

8.2.3 Estimation of drug/dye encapsulation efficiencies

The fluorescence (FL) intensity of the fluorescent dyes was estimated using a Hitachi F-2000 Fluorescence spectrophotometer. The calibration plots of fluorescence intensity versus the concentration of the drug/dye were initially obtained as follows. The different concentrations (1, 5, 10, 25, 50 µg/ml) of DOX and FITC solutions were prepared from a stock solution of 500 µg/ml. A drop (equivalent to 10 µl) of DOX and FITC solutions was then added on a glass slide at a time and the fluorescence images were taken at an optimized exposure time with the red channel and the green channel respectively under the 40X oil immersed objective lenses (n=4). For each concentration, the intensity plot profile was determined and the area under the curve was calculated which is a measure of the intensity. Using these intensities, the calibration curves were plotted as shown in the Figure S1. Adopting similar experimental procedure, the fluorescence intensities (red and green) of the conjugated nanoparticle samples were also determined.

8.2.4: Cellular studies

The intracellular distribution of surface functionalized NPs into the human pancreatic carcinoma cell lines was imaged with an optical microscope (Axiovert 200, Zeiss). Equivalent

amounts of MIA PaCa-2 cells were seeded in 35 mm poly L-lysine coated petri dishes with 2 ml of cell growth medium containing Dulbecco's modified essential medium (DMEM), 10% fetal bovine serum (FBS) and 5% penicillin. The cells were then incubated for 24 h at 37°C in a humidified 5% CO_2 atmosphere. Following 24 h of incubation, half the medium was extracted out and replaced with fresh medium containing 200 µg of Dex-SPIO-DOX/FITC. After 15 minutes of further incubation, the cells were washed three times with 1ml of PBS to remove any excess and unbound NPs. Then, cells were fixed with 4% glutaraldehyde in PBS at 25°C for 30 mins. The same procedure was followed with the cells incubated with free DOX and FITC. The concentrations of free DOX and FITC were kept approximately identical to that of the respective drug and dye, present in Dex-SPIO-DOX/FITC. The experiments were carried out in triplicates.

8.3: Results and Discussions

The structural and magnetic characterizations of the nanoparticles are shown in Chapter 7. The as-synthesized NPs were coated with dextran (Dex-Fe_3O_4) and subsequently crosslinked using epichlorohydrin (ECH). The crosslinked Fe_3O_4NPs were grafted with carboxylic groups using monochlroacetic (MCA) acid to obtain the carboxymethylated Fe_3O_4NPs (CMD- Fe_3O_4). The Dox and FITC were attached to the CMD- Fe_3O_4 NPs through EDC/NHS chemistry. EDC and NHS were added to CMD- Fe_3O_4 NPs suspension to activate the carboxyl groups. Dox was added to that mixture followed by the addition of Ethylene diamine hydrochloride (EDA) to react with the activated carboxyl groups which provide amine group (-NH_2) for further conjugation with FITC. The detailed procedure is explained in section 3.2.5 and schematic representation of the conjugation steps is shown in Fig. 8.1.

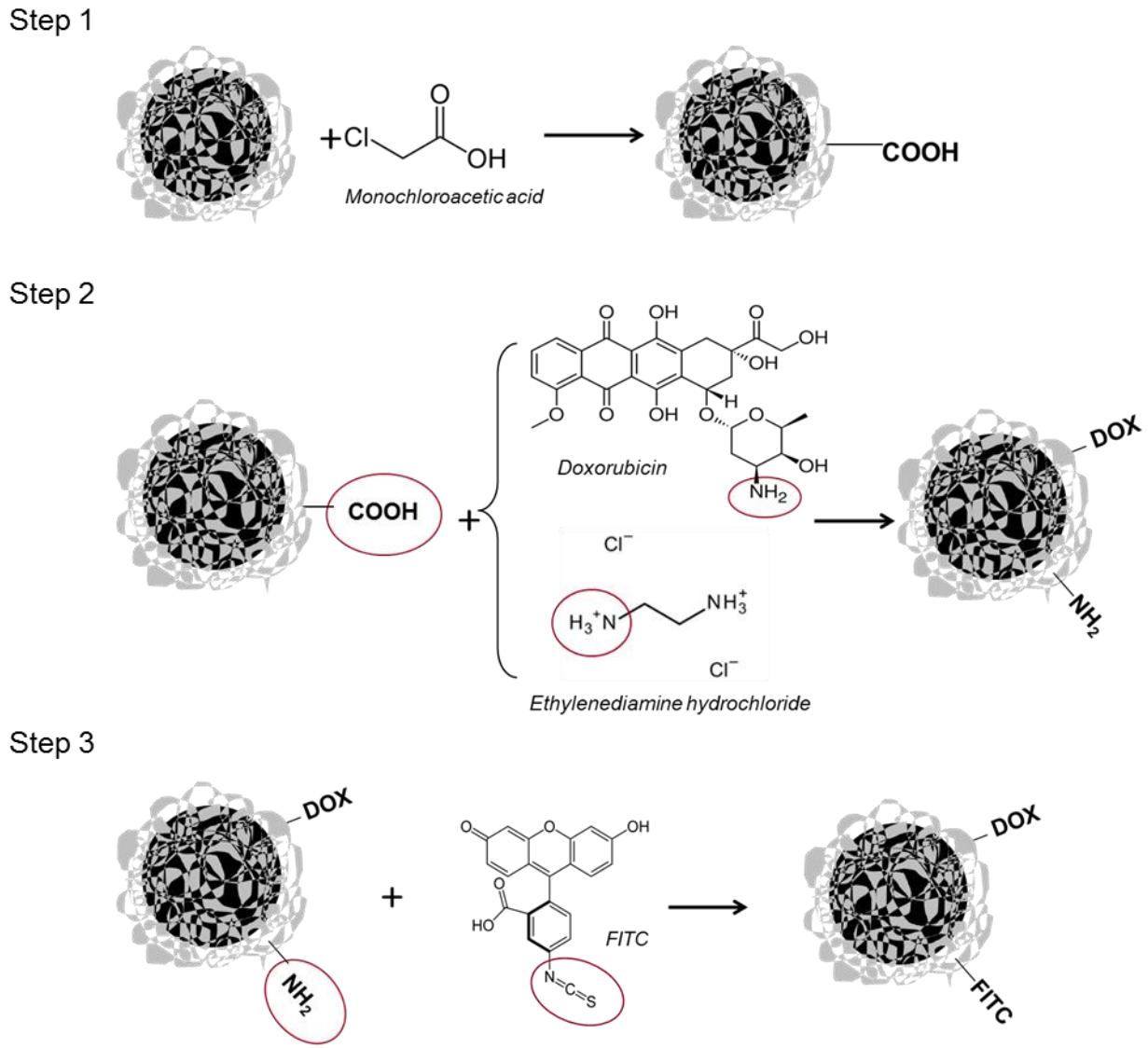

Figure 8.1: Schematic representation of the synthesis of the magnetic drug delivery system composed of Dextran coated Fe_3O_4 cores and DOX, FITC conjugations on the surface.

The hydrodynamic diameters of the Dex-SPIO and Dex-SPIO-DOX/FITC samples in water at 25°C and pH of 7.4 were found to be 100±25 nm and 143±40 nm respectively, whereas the respective zeta potential values are -17±3 mV and -9±1 mV. The changes in the size and the surface charge upon functionalizing the NPs with DOX/FITC further confirm the conjugation of the dye to the Dex-SPIO complex, besides the observation of the association of fluorescence.

Using these intensities, the calibration curves were plotted as shown in the Figure 8.2. Then following the same experimental procedure, the fluorescence intensities (red and green) of the conjugated sample were determined to be 10% and 1% for FITC and Dox respectively.

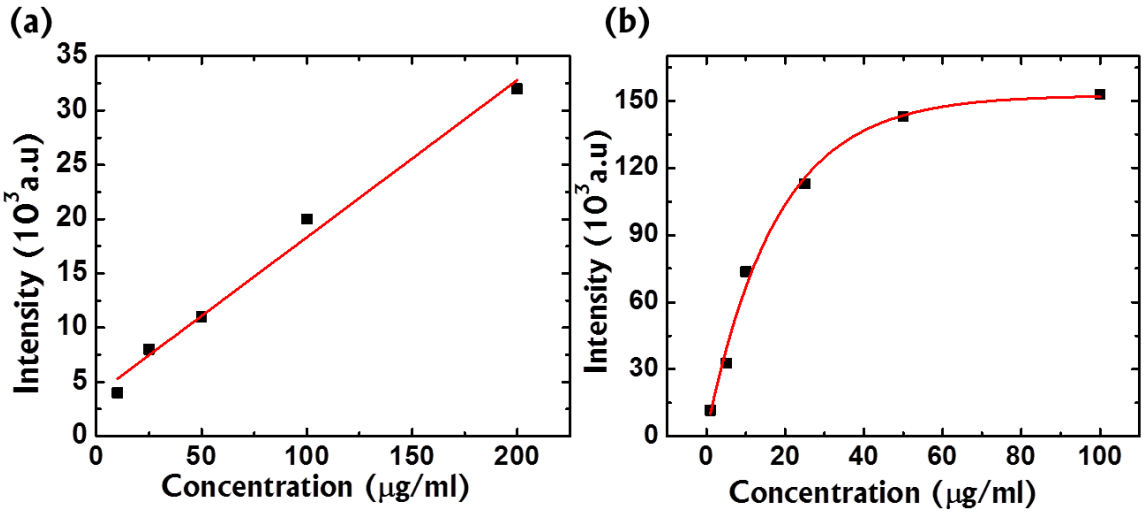

Figure 8.2: Calibration fits of (a) FITC and (b) doxorubicin to estimate the drug/dye quantification incorporated with Fe3O4 nanoparticles conjugate.

The calibration plots of fluorescence intensity versus the concentration of the free drug/dye are shown in Fig 8.2. From the plots, using the fluorescence intensities (red and green) of the conjugated sample the dye/drug loading efficiencies were determined to be 10% and 1% for FITC and Dox respectively. To examine the efficacy of DOX on human pancreatic carcinoma, experiments were conducted on the MIA PaCa 2 cells both in presence (experimental) and absence (control) of the drug. Images of the control and experimental at 6 h time point demonstrating the entry of the drug into the nucleus of the malignant cells are shown in Figure 4(a).

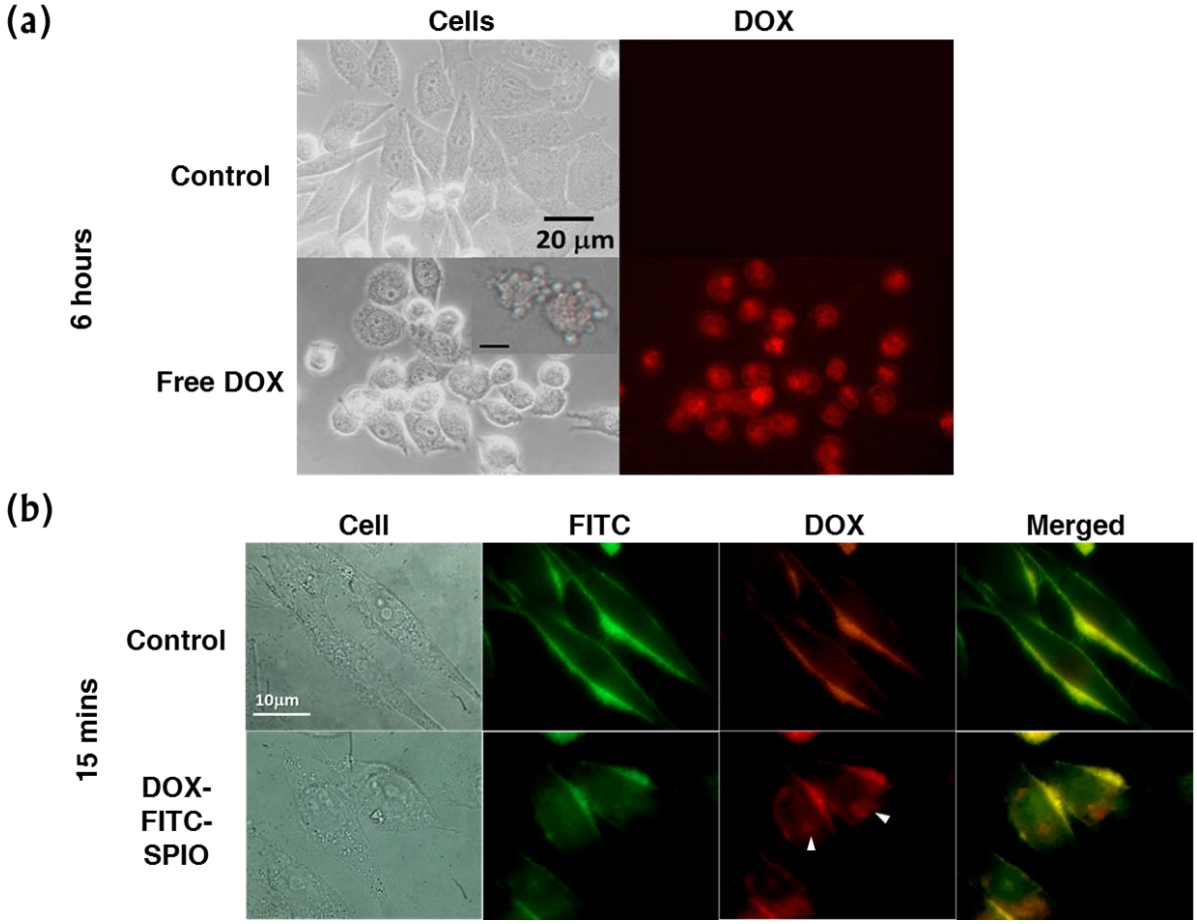

Figure 8.3: (a) The fluorescence microscopy images of MIA PaCa 2 cells incubated with DOX. Note cellular entry (especially into the nucleus) of the drug in the 6 h time point and cell rounding. The inset shows blebbing of the cells prior to cell death. (b) The fluorescence microscopy images of MIA PaCa 2 cells incubated with free DOX + free FITC (control) and DOX-FITC conjugated Fe_3O_4 NPs at 15 mins. Green and red fluorescence represent FITC and DOX respectively. Arrow heads indicates the DOX entry into the nucleus.

The images further demonstrate cell rounding and cell blebbing prior to their death, clearly indicating the role of DOX in apoptosis. To examine the cellular internalization of synthesized drug-dye-nano carrier conjugation, we conducted a series of fluorescence imaging experiments on MIA PaCa-2 cells, grown attached to the tissue culture plates. The inherent fluorescence of DOX (red) and FITC (green) were used to track their internalization. For comparative studies, control experiments were carried out using the unconjugated DOX and FITC. Figure 4(b) shows images collected at 15 minutes for control and experimental samples.

The cells exposed to unconjugated DOX/FITC and Dex-SPIO-DOX/FITC show high fluorescence intensities on the membrane indicating their strong binding. However, higher fluorescence intensities (both green and red) are observed within the cells that were exposed to the Dex-SPIO-DOX/FITC, as compared to the cells exposed to the unconjugated DOX/FITC. These results indicate a rapid entry of Dex-SPIO-DOX/FITC into the cell than free DOX/FITC which might be due to different entrance pathways. It has been well established that the free DOX is taken up by the cells only through Fickian diffusion [221,222] while the cellular uptake of Dex-SPIO-DOX/FITC is carried out most likely through endocytosis [223,224]. In this context, conjugation of the drug with NPs facilitated cellular uptake of DOX through endocytosis. For an efficient drug delivery system, not only the rapid uptake by the cancer cell is crucial but also the drug release within the cell is of great importance. From Figure 4(b), it is clearly observed that the distribution of DOX is very different upon NPs conjugation. In the control experiments, the fluorescence intensities on the cell membrane are much higher than in the cytoplasm implying that the unconjugated DOX as well as FITC are residing on the cell membrane. On the other hand, the distribution of red fluorescence within the cells exposed to conjugated DOX is different. The red and green fluorescence are partially separated and the red fluorescence seems to accumulate within the nucleus while green fluorescence stays outside of it indicating the release of DOX from the conjugation after entering the cells.

8.7: Conclusions

In summary, we were able to design and develop a drug delivery platform based on Fe_3O_4NPs as the vehicle for an anti-cancer drug (Dox), attached to a model dye (FITC) for their precise tracking. Employing the fluorescence microscopy, we were able to demonstrate that even in the absence of any targeting ligand, the internalization of the Dox-FITC-$Fe_3O_4$is much higher

as compared to the unconjugated Dox, enabling an efficient utilization of the anti-cancer drug. In addition to rapid uptake of these NPs by live cells, our results also suggest that upon entering the cells, Dox is cleaved from the conjugation, which might be due to the enzymatic reactions that occur within the cells, and tends to accumulate in the nuclei fulfilling the major requirement for an effective therapeutic system. We hypothesize that incorporation of targeting ligands into this system could further enhance its performance and accordingly remodel it to be used in different cell types.

CHAPTER 9 CONCLUSIONS AND FUTURE WORK

Magnetic nanoparticles (MNPs), especially superparamagnetic Fe_3O_4 nanoparticles, have attracted a great deal of attention due to their potential multimodal functionality in biomedical applications. The research presented in this thesis is focused on exploiting the functionality of Fe_3O_4 nanoparticles for two important biomedical applications; magnetic hyperthermia and drug delivery.

The first part of this thesis focuses on understanding and optimizing the properties of Fe_3O_4 nanoparticles for the maximum efficiency of heat generation. It is well known that the SAR, which measures the magnetic hyperthermia efficiency, depends on magnetic properties of the particles such as saturation magnetization, magnetic anisotropy, particle size distribution, magnetic dipolar interactions, and the rheological properties of the target medium. We synthesized Fe_3O_4 nanoparticles by two different methods, co-precipitation (CP) and the hydrothermal (HT) synthesis, exhibiting similar structural and magnetic properties. Despite having similar particle size (~ 12 nm) and saturation magnetization (~ 70 emu/g) they show drastically different heating rates (SAR) at room temperature ~ 110 W/g (CP sample) and ~ 40 W/g (HT sample). This observed reduction in SAR has been explained by taking into account the dipolar interactions using the so called T^* model. Our analysis reveals that HT ferrofluid shows a higher effective dipolar interaction and a wider distribution of magnetic core size of MNPs compared to that of CP ferrofluid leading to a decrease in SAR.

Through this study we have been able to determine the effect of particle size, polydispersity, magnetic anisotropy and dipolar interactions on the temperature dependent SAR, qualitatively and quantitatively, which allow us to design nanoparticles for optimized SAR. For example, nanoparticles of 14-15 nm size with a narrow size distribution and lower dipolar

interactions would show SAR more than 200 W/g. Furthermore our results show that although the HT method of synthesis leads to clustering of nanoparticles with strong dipolar interaction, it is very versatile method in tailoring the particle size and distribution and hence further research is necessary to figure out a suitable capping agent to avoid clustering of particles during the synthesis.

We have also investigated the effect of the Gd-doping on the magnetic properties of nanoparticles and the associated magnetic hyperthermia response of the ferrofluids. The possibility of using Gd doped Fe_3O_4 nanoparticles as a dual modal T_1-T_2 contrast agent is being currently explored by others. However, the possibility of using this doped system for magnetic hyperthermia is not explored well. Both Gd-doped and un-doped iron oxide nanoparticles were synthesized using co-precipitation method and coated with dextran. Our analysis on structural and magnetic characterization data reveals that Gd (2.5 wt. %)-doping of Fe_3O_4 nanoparticles leads to an increase in particle size and a reduced saturation magnetization. MHT experiments revels that Gd-doped Fe_3O_4 exhibits a similar SAR value as that of un-doped Fe_3O_4 ferrofluid. Our magnetic hyperthermia research demonstrates that this material is a potential candidate for theronostics for multimodal contrast imaging and cancer treatment by hyperthermia.

From the analysis of temperature dependent SAR curves of Gd-doped Fe_3O_4 ferrofluids, we found that the magnetocrystalline anisotropy (K) was found to decrease by 50% upon Gd-doping. Among the very little literature on SAR of Gd-doped Fe_3O_4 nanoparticles present, a recent study done by Douglas et. al [225] reports a SAR of 3.7±0.6 W/g_{Fe}^{-1} at H_0 = 3 kA/m and f =111 kHz for 2% Gd doping. The authors attribute this observed enhancement in SAR to an increase in magnetic anisotropy of Fe_3O_4 nanoparticles upon Gd doping, in contradiction to our observation of a decrease in K dut to Gd doping. Further research is necessary to resolve this

contradiction and further optimize the amount of Gd-doping to enhance SAR for cancer treatment, as well as for a dual modal T_1-T_2 contrast agent.

We have made a comparative study of two different biocompatible coatings, dextran and CA, on the colloidal and magnetic properties of Fe_3O_4nanoparticles as well as their impact on magnetic hyperthermia efficiency was studied. Both the ferrofluids show similar magnetic and hyperthermia properties, indicating that these surface modifications have no effect on their performance. However, our concentration dependent magnetic hyperthermia results indicate that the dilution of the sample should be done with extensive care as it may promote cluster formation which in turn reduces the SAR value.

Moreover, upon exposure to cell growth medium that mimics the physiological environment, formation of corona was observed for both dextran and CA coated nanoparticles as seen from the hydrodynamic size measurements. It was observed that in CA coated particles where, this protein corona forms faster, in several minutes to hours, causes aggregations in solution and reduces SAR by ~ 45%. Dextran coated nanoparticles show a better stability at least within first 3-6 hours upon exposure to the proteins in the cell growth medium exhibiting excellent performance in both water and simulated physiological conditions. Furthermore, the cytotoxicity studies done on human pancreatic cancer cells indicate that both dextran and CA coated Fe_3O_4 ferrofluids are nontoxic to the cells at or below 100 μg/mL concentration. Though further in vivo study is necessary in the future, these results imply that the dextran coated Fe_3O_4 dispersion could maintain their high heating capacity in physiological environments while CA coating require further surface modification to reduce the non-specific protein adsorption. However, the rapid formation of protein corona accelerates the endocytosis pathway leading to the rapid entry of the nanoparticles into the cells which is a crucial factor for applications such as

drug delivery and magnetic hyperthermia for cancer treatment [226-228]. Therefore it would be necessary to perform in-vitro hyperthermia for these different coatings to investigate the effect of the protein corona, which depends on the surface properties of the nanoparticles, on the hyperthermia efficiency.

We also have successfully functionalized dextran coated Fe_3O_4 nanoparticles with fluorescence dye, FITC, to investigate their binding and distribution in Mia PaCa-2 human pancreatic cancer cells. Our results done on investigating the traffic, distribution, and cytotoxicity, associated with these Fe_3O_4 nanoparticles, demonstrate that there is a time-dependent distribution of these nanoparticles into different cellular compartments. It will be interesting to explore the possibility of incorporating the magnetic hyperthermia with these nanoparticles, for an enhanced cellular uptake as the magnetic heating may influence the dynamics of nanoparticles through the cell membrane.

Furthermore, we were able to design and develop a drug delivery platform based on Fe_3O_4 NPs as the vehicle for an anti-cancer drug (Dox), attached to a model dye (FITC) for their precise tracking. Employing the fluorescence microscopy, we were able to demonstrate that even in the absence of any targeting ligand, the internalization of the Dox-FITC-$Fe_3O_4$is much higher as compared to the unconjugated Dox, enabling an efficient utilization of the anti-cancer drug. In addition to rapid uptake of these NPs by live cells, our results also suggest that upon entering the cells, Dox is cleaved from the conjugation, which might be due to the enzymatic reactions that occur within the cells, and tends to accumulate in the nuclei fulfilling the major requirement for an effective therapeutic system. We hypothesize that incorporation of targeting ligands into this system could further enhance its performance and accordingly remodel it to be used in different cell types.

REFERENCES

[1] N.T.K. Thanh, L.A.W. Green, Nano Today 5 (2010) 213.

[2] Z. Li, J.C. Barnes, A. Bosoy, J.F. Stoddart, J.I. Zink, Chemical Society Reviews 41 (2012) 2590.

[3] L. Dykman, N. Khlebtsov, Chemical Society Reviews 41 (2012) 2256.

[4] N. Sounderya, Y. Zhang, Recent Patents on Biomedical Engineering 1 (2008) 34.

[5] D.K. Chatterjee, M.K. Gnanasammandhan, Y. Zhang, Small 6 (2010) 2781.

[6] C. Corot, P. Robert, J.-M. Idée, M. Port, Advanced Drug Delivery Reviews 58 (2006) 1471.

[7] F.Q. Hu, L. Wei, Z. Zhou, Y.L. Ran, Z. Li, M.Y. Gao, Advanced Materials 18 (2006) 2553.

[8] Y.-X.J. Wang, Quantitative Imaging in Medicine and Surgery 1 (2011) 35.

[9] T. Neuberger, B. Schöpf, H. Hofmann, M. Hofmann, B. von Rechenberg, Journal of Magnetism and Magnetic Materials 293 (2005) 483.

[10] L.H. Reddy, J.L. Arias, J. Nicolas, P. Couvreur, Chemical Reviews 112 (2012) 5818.

[11] X. Yang, Y. Chen, R. Yuan, G. Chen, E. Blanco, J. Gao, X. Shuai, Polymer 49 (2008) 3477.

[12] J.-P. Fortin, C. Wilhelm, J. Servais, C. Ménager, J.-C. Bacri, F. Gazeau, Journal of the American Chemical Society 129 (2007) 2628.

[13] H. Rudolf, D. Silvio, M. Robert, Z. Matthias, Journal of Physics: Condensed Matter 18 (2006) S2919.

[14] A.E. Deatsch, B.A. Evans, Journal of Magnetism and Magnetic Materials 354 (2014) 163.

[15] R.S. Molday, D. MacKenzie, J Immunol Methods 52 (1982) 353.

[16] H. Xu, Z.P. Aguilar, L. Yang, M. Kuang, H. Duan, Y. Xiong, H. Wei, A. Wang, Biomaterials 32 (2011) 9758.

[17] S. Maenosono, S. Saita, IEEE Transactions on Magnetics 42 (2006) 1638.

[18] P. Wust, B. Hildebrandt, G. Sreenivasa, B. Rau, J. Gellermann, H. Riess, R. Felix, P.M. Schlag, The Lancet Oncology 3 (2002) 487.

[19] R.K. Gilchrist, R. Medal, W.D. Shorey, R.C. Hanselman, J.C. Parrott, C.B. Taylor, Annals of Surgery 146 (1957) 596.

[20] H. Zhu, targeted nanoparticle drug for magnetic hyperthermia treatment on malignant tumors. Google Patents, 2011.

[21] B. Polyak, G. Friedman, Expert Opinion on Drug Delivery 6 (2009) 53.

[22] F. Sonvico, S. Mornet, S. Vasseur, C. Dubernet, D. Jaillard, J. Degrouard, J. Hoebeke, E. Duguet, P. Colombo, P. Couvreur, Bioconjugate Chemistry 16 (2005) 1181.

[23] W.I. Choi, J.-Y. Kim, C. Kang, C.C. Byeon, Y.H. Kim, G. Tae, ACS Nano 5 (2011) 1995.

[24] G.v. Maltzahn, J.-H. Park, A. Agrawal, N.K. Bandaru, S.K. Das, M.J. Sailor, S.N. Bhatia, Cancer research 69 (2009) 3892.

[25] D.P. O'Neal, L.R. Hirsch, N.J. Halas, J.D. Payne, J.L. West, Cancer Letters 209 (2004) 171.

[26] C. Fong-Yu, C. Chen-Tai, Y. Chen-Sheng, Nanotechnology 20 (2009) 425104.

[27] N.W.S. Kam, M. O'Connell, J.A. Wisdom, H. Dai, Proceedings of the National Academy of Sciences of the United States of America 102 (2005) 11600.

[28] A.S. Biris, D. Boldor, J. Palmer, W.T. Monroe, M. Mahmood, E. Dervishi, Y. Xu, Z. Li, E.I. Galanzha, V.P. Zharov, Journal of biomedical optics 14 (2009) 021007.

[29] S.V. Torti, F. Byrne, O. Whelan, N. Levi, B. Ucer, M. Schmid, F.M. Torti, S. Akman, J. Liu, P.M. Ajayan, O. Nalamasu, D.L. Carroll, International Journal of Nanomedicine 2 (2007) 707.

[30] H.K. Moon, S.H. Lee, H.C. Choi, ACS Nano 3 (2009) 3707.

[31] A. Sahu, W.I. Choi, J.H. Lee, G. Tae, Biomaterials 34 (2013) 6239.

[32] E.S. Glazer, S.A. Curley, Cancer 116 (2010) 3285.

[33] M. Chu, X. Pan, D. Zhang, Q. Wu, J. Peng, W. Hai, Biomaterials 33 (2012) 7071.

[34] M. Jeun, S. Lee, J. Kyeong Kang, A. Tomitaka, K. Wook Kang, Y. Il Kim, Y. Takemura, K.-W. Chung, J. Kwak, S. Bae, Applied Physics Letters 100 (2012) 092406.

[35] R. Müller, S. Dutz, A. Neeb, A.C.B. Cato, M. Zeisberger, Journal of Magnetism and Magnetic Materials 328 (2013) 80.

[36] S. Laurent, S. Dutz, U.O. Häfeli, M. Mahmoudi, Advances in Colloid and Interface Science 166 (2011) 8.

[37] Z. Nemati, J. Alonso, L.M. Martinez, H. Khurshid, E. Garaio, J.A. Garcia, M.H. Phan, H. Srikanth, The Journal of Physical Chemistry C 120 (2016) 8370.

[38] A. Walter, C. Billotey, A. Garofalo, C. Ulhaq-Bouillet, C. Lefèvre, J. Taleb, S. Laurent, L. Vander Elst, R.N. Muller, L. Lartigue, F. Gazeau, D. Felder-Flesch, S. Begin-Colin, Chemistry of Materials 26 (2014) 5252.

[39] C. Martinez-Boubeta, K. Simeonidis, A. Makridis, M. Angelakeris, O. Iglesias, P. Guardia, A. Cabot, L. Yedra, S. Estradé, F. Peiró, Z. Saghi, P.A. Midgley, I. Conde-Leborán, D. Serantes, D. Baldomir, Scientific Reports 3 (2013) 1652.

[40] S. Larumbe, C. Gómez-Polo, J.I. Pérez-Landazábal, J.M. Pastor, Journal of Physics: Condensed Matter 24 (2012) 266007.

[41] H. Zeng, J. Li, Z.L. Wang, J.P. Liu, S. Sun, Nano Letters 4 (2004) 187.

[42] S.-C. Lee, C.-M. Fu, F.-H. Chang, Applied Physics Letters 103 (2013) 163104.

[43] I. Sharifi, H. Shokrollahi, S. Amiri, Journal of Magnetism and Magnetic Materials 324 (2012) 903.

[44] C. Pereira, A.M. Pereira, C. Fernandes, M. Rocha, R. Mendes, M.P. Fernández-García, A. Guedes, P.B. Tavares, J.-M. Grenèche, J.P. Araújo, C. Freire, Chemistry of Materials 24 (2012) 1496.

[45] X. Lasheras, M. Insausti, I. Gil de Muro, E. Garaio, F. Plazaola, M. Moros, L. De Matteis, J. M. de la Fuente, L. Lezama, The Journal of Physical Chemistry C 120 (2016) 3492.

[46] S. Vasseur, E. Duguet, J. Portier, G. Goglio, S. Mornet, E. Hadová, K. Knížek, M. Maryško, P. Veverka, E. Pollert, Journal of Magnetism and Magnetic Materials 302 (2006) 315.

[47] J.-t. Jang, H. Nah, J.-H. Lee, S.H. Moon, M.G. Kim, J. Cheon, Angewandte Chemie International Edition 48 (2009) 1234.

[48] K.J. Miller, M. Sofman, K. McNerny, M.E. McHenry, Journal of Applied Physics 107 (2010) 09A305.

[49] A. Ito, M. Shinkai, H. Honda, T. Kobayashi, Journal of Bioscience and Bioengineering 100 (2005) 1.

[50] S.C. McBain, H.H.P. Yiu, J. Dobson, International Journal of Nanomedicine 3 (2008) 169.

[51] S. Laurent, D. Forge, M. Port, A. Roch, C. Robic, L. Vander Elst, R.N. Muller, Chemical Reviews 108 (2008) 2064.

[52] J. Thevenot, H. Oliveira, O. Sandre, S. Lecommandoux, Chemical Society Reviews 42 (2013) 7099.

[53] M. Karimi, A. Ghasemi, P. Sahandi Zangabad, R. Rahighi, S.M. Moosavi Basri, H. Mirshekari, M. Amiri, Z. Shafaei Pishabad, A. Aslani, M. Bozorgomid, D. Ghosh, A. Beyzavi, A. Vaseghi, A.R. Aref, L. Haghani, S. Bahrami, M.R. Hamblin, Chemical Society Reviews 45 (2016) 1457.

[54] M. Bonini, D. Berti, P. Baglioni, Current Opinion in Colloid and Interface Science 18 (2013) 459.

[55] K. Hayashi, K. Ono, H. Suzuki, M. Sawada, M. Moriya, W. Sakamoto, T. Yogo, ACS Applied Materials & Interfaces 2 (2010) 1903.

[56] E. Munnier, S. Cohen-Jonathan, C. Linassier, L. Douziech-Eyrolles, H. Marchais, M. Soucé, K. Hervé, P. Dubois, I. Chourpa, International Journal of Pharmaceutics 363 (2008) 170.

[57] J. Gautier, E. Munnier, A. Paillard, K. Hervé, L. Douziech-Eyrolles, M. Soucé, P. Dubois, I. Chourpa, International Journal of Pharmaceutics 423 (2012) 16.

[58] X. He, X. Wu, X. Cai, S. Lin, M. Xie, X. Zhu, D. Yan, Langmuir 28 (2012) 11929.

[59] X.Y. Ying, Y.Z. Du, L.H. Hong, H. Yuan, F.Q. Hu, Journal of Magnetism and Magnetic Materials 323 (2011) 1088.

[60] X. He, X. Wu, X. Cai, S. Lin, M. Xie, X. Zhu, D. Yan, Langmuir 28 (2012) 11929.

[61] C. Liao, Q. Sun, B. Liang, J. Shen, X. Shuai, European Journal of Radiology 80 (2011) 699.

[62] Q. Quan, J. Xie, H. Gao, M. Yang, F. Zhang, G. Liu, X. Lin, A. Wang, H.S. Eden, S. Lee, G. Zhang, X. Chen, Molecular Pharmaceutics 8 (2011) 1669.

[63] Y.J. Gu, J. Cheng, C.W.Y. Man, W.T. Wong, S.H. Cheng, Nanomedicine: Nanotechnology, Biology, and Medicine 8 (2012) 204.

[64] M.Y. Hua, H.W. Yang, H.L. Liu, R.Y. Tsai, S.T. Pang, K.L. Chuang, Y.S. Chang, T.L. Hwang, Y.H. Chang, H.C. Chuang, C.K. Chuang, Biomaterials 32 (2011) 8999.

[65] R. Regmi, C. Black, C. Sudakar, P.H. Keyes, R. Naik, G. Lawes, P. Vaishnava, C. Rablau, D. Kahn, M. Lavoie, V.K. Garg, A.C. Oliveira, Journal of Applied Physics 106 (2009) 113902.

[66] Y. Sahoo, H. Pizem, T. Fried, D. Golodnitsky, L. Burstein, C.N. Sukenik, G. Markovich, Langmuir 17 (2001) 7907.

[67] Y. Sahoo, A. Goodarzi, M.T. Swihart, T.Y. Ohulchanskyy, N. Kaur, E.P. Furlani, P.N. Prasad, The Journal of Physical Chemistry B 109 (2005) 3879.

[68] M.H. Sousa, J.C. Rubim, P.G. Sobrinho, F.A. Tourinho, Journal of Magnetism and Magnetic Materials 225 (2001) 67.

[69] S.S. Banerjee, D.-H. Chen, Chemistry of Materials 19 (2007) 6345.

[70] G. Minigo, A. Scholzen, C.K. Tang, J.C. Hanley, M. Kalkanidis, G.A. Pietersz, V. Apostolopoulos, M. Plebanski, Vaccine 25 (2007) 1316.

[71] M. Lewin, N. Carlesso, C.-H. Tung, X.-W. Tang, D. Cory, D.T. Scadden, R. Weissleder, Nat Biotech 18 (2000) 410.

[72] M.J. Roberts, M.D. Bentley, J.M. Harris, Advanced Drug Delivery Reviews 54 (2002) 459.

[73] S. Liang, Y. Wang, J. Yu, C. Zhang, J. Xia, D. Yin, Journal of Materials Science: Materials in Medicine 18 (2007) 2297.

[74] Z. Chunfu, C. Jinquan, Y. Duanzhi, W. Yongxian, F. Yanlin, T. Jiajü, Applied Radiation and Isotopes 61 (2004) 1255.

[75] O. Veiseh, J. Gunn, M. Zhang, Advanced drug delivery reviews 62 (2010) 284.

[76] J.W.M. Bulte, L.D. Ma, R.L. Magin, R.L. Kamman, C.E. Hulstaert, K.G. Go, T.H. The, L. De Leij, Magnetic Resonance in Medicine 29 (1993) 32.

[77] S.P. Massia, J. Stark, D.S. Letbetter, Biomaterials 21 (2000) 2253.

[78] R. Weissleder, G. Elizondo, J. Wittenberg, A.S. Lee, L. Josephson, T.J. Brady, Radiology 175 (1990) 494.

[79] L. Josephson, C.-H. Tung, A. Moore, R. Weissleder, Bioconjugate Chemistry 10 (1999) 186.

[80] P. Wunderbaldinger, L. Josephson, R. Weissleder, Academic Radiology 9 S304.

[81] M. Mikhaylova, D.K. Kim, N. Bobrysheva, M. Osmolowsky, V. Semenov, T. Tsakalakos, M. Muhammed, Langmuir 20 (2004) 2472.

[82] D.K. Kim, M. Mikhaylova, F.H. Wang, J. Kehr, B. Bjelke, Y. Zhang, T. Tsakalakos, M. Muhammed, Chemistry of Materials 15 (2003) 4343.

[83] K. Donadel, M.D.V. Felisberto, V.T. Fávere, M. Rigoni, N.J. Batistela, M.C.M. Laranjeira, Materials Science and Engineering: C 28 (2008) 509.

[84] E.B. Denkbaş, E. Kiliçay, C. Birlikseven, E. Öztürk, Reactive and Functional Polymers 50 (2002) 225.

[85] E.H. Kim, Y. Ahn, H.S. Lee, Journal of Alloys and Compounds 434–435 (2007) 633.

[86] E. Khor, L.Y. Lim, Biomaterials 24 (2003) 2339.

[87] A.K. Gupta, S. Wells, IEEE Transactions on Nanobioscience 3 (2004) 66.

[88] Y. Zhang, N. Kohler, M. Zhang, Biomaterials 23 (2002) 1553.

[89] A.K. Gupta, A.S.G. Curtis, Journal of Materials Science: Materials in Medicine 15 (2004) 493.

[90] C. Sudakar, A. Dixit, R. Regmi, R. Naik, G. Lawes, V.M. Naik, P.P. Vaishnava, U. Toti, J. Panyam, IEEE Transactions on Magnetics 44 (2008) 2800.

[91] H.L. Ma, Y.F. Xu, X.R. Qi, Y. Maitani, T. Nagai, International Journal of Pharmaceutics 354 (2008) 217.

[92] M.A. Morales, P.V. Finotelli, J.A.H. Coaquira, M.H.M. Rocha-Leão, C. Diaz-Aguila, E.M. Baggio-Saitovitch, A.M. Rossi, Materials Science and Engineering: C 28 (2008) 253.

[93] H. Wang, W. Luo, J. Chen, Journal of Materials Science 47 (2012) 5918.

[94] G. Chen, A.S. Hoffman, Bioconjugate Chemistry 4 (1993) 509.

[95] R. Regmi, S.R. Bhattarai, C. Sudakar, A.S. Wani, R. Cunningham, P.P. Vaishnava, R. Naik, D. Oupicky, G. Lawes, Journal of Materials Chemistry 20 (2010) 6158.

[96] J. Fang, C. Wang, M. Cao, M. Cheng, J. Shi, Y. Jin, Materials Letters 96 (2013) 89.

[97] I.-K. Park, C.-P. Ng, J. Wang, B. Chu, C. Yuan, S. Zhang, S.H. Pun, Biomaterials 29 (2008) 724.

[98] M. Chorny, B. Polyak, I.S. Alferiev, K. Walsh, G. Friedman, R.J. Levy, The FASEB Journal 21 (2007) 2510.

[99] B. Steitz, H. Hofmann, S.W. Kamau, P.O. Hassa, M.O. Hottiger, B. von Rechenberg, M. Hofmann-Amtenbrink, A. Petri-Fink, Journal of Magnetism and Magnetic Materials 311 (2007) 300.

[100] S.C. McBain, H.H.P. Yiu, A. El Haj, J. Dobson, Journal of Materials Chemistry 17 (2007) 2561.

[101] P. Mulvaney, L.M. Liz-Marzan, M. Giersig, T. Ung, Journal of Materials Chemistry 10 (2000) 1259.

[102] P. Tartaj, T. González-Carreño, C.J. Serna, Langmuir 18 (2002) 4556.

[103] P. Tartaj, T. González-Carreño, C.J. Serna, Advanced Materials 13 (2001) 1620.

[104] J. Kim, H.S. Kim, N. Lee, T. Kim, H. Kim, T. Yu, I.C. Song, W.K. Moon, T. Hyeon, Angewandte Chemie International Edition 47 (2008) 8438.

[105] M. Mandal, S. Kundu, S.K. Ghosh, S. Panigrahi, T.K. Sau, S.M. Yusuf, T. Pal, Journal of Colloid and Interface Science 286 (2005) 187.

[106] W. Wei, H. Quanguo, C. Hong, T. Jianxin, N. Libo, Nanotechnology 18 (2007) 145609.

[107] H. Yu, M. Chen, P.M. Rice, S.X. Wang, R.L. White, S. Sun, Nano Letters 5 (2005) 379.

[108] Z. Wang, H. Guo, Y. Yu, N. He, Journal of Magnetism and Magnetic Materials 302 (2006) 397.

[109] G. Amoretti, J.M. Fournier, Journal of Magnetism and Magnetic Materials 43 (1984) L217.

[110] N.A. Spaldin, Magnetic materials: fundamentals and applications, Cambridge University Press, 2010.

[111] F. Bødker, S. Mørup, S. Linderoth, Physical Review Letters 72 (1994) 282.

[112] B.D. Plouffe, S.K. Murthy, L.H. Lewis, Reports on progress in physics. Physical Society (Great Britain) 78 (2015) 016601.

[113] S. Mørup, M.F. Hansen, C. Frandsen, Beilstein Journal of Nanotechnology 1 (2010) 182.

[114] J.M. Vargas, W.C. Nunes, L.M. Socolovsky, M. Knobel, D. Zanchet, Physical Review B 72 (2005) 184428.

[115] J.L. Dormann, L. Spinu, E. Tronc, J.P. Jolivet, F. Lucari, F. D'Orazio, D. Fiorani, Journal of Magnetism and Magnetic Materials 183 (1998) L255.

[116] E. Tronc, P. Prené, J.P. Jolivet, D. Fiorani, A.M. Testa, R. Cherkaoui, M. Nogues, J.L. Dormann, Nanostructured Materials 6 (1995) 945.

[117] J.L. Dormann, L. Bessais, D. Fiorani, Journal of Physics C: Solid State Physics 21 (1988) 2015.

[118] M. Hayashi, M. Susa, K. Nagata, Journal of Magnetism and Magnetic Materials 171 (1997) 170.

[119] S.H. Masunaga, R.F. Jardim, R.S. Freitas, J. Rivas, Applied Physics Letters 98 (2011) 013110.

[120] G.T. Landi, Journal of Applied Physics 113 (2013) 163908.

[121] P. Allia, M. Coisson, P. Tiberto, F. Vinai, M. Knobel, M. Novak, W. Nunes, Physical Review B 64 (2001) 144420.

[122] R.E. Rosensweig, Journal of Magnetism and Magnetic Materials 252 (2002) 370.

[123] S. Sun, H. Zeng, Journal of the American Chemical Society 124 (2002) 8204.

[124] N.R. Jana, Y. Chen, X. Peng, Chemistry of Materials 16 (2004) 3931.

[125] T. Hyeon, Chemical Communications (2003) 927.

[126] A.G. Roca, R. Costo, A.F. Rebolledo, S. Veintemillas-Verdaguer, P. Tartaj, T. González-Carreño, M.P. Morales, C.J. Serna, Journal of Physics D: Applied Physics 42 (2009) 224002.

[127] M. Mascolo, Y. Pei, T. Ring, Materials 6 (2013) 5549.

[128] A.H. Latham, M.E. Williams, Accounts of Chemical Research 41 (2008) 411.

[129] T.J. Daou, G. Pourroy, S. Bégin-Colin, J.M. Grenèche, C. Ulhaq-Bouillet, P. Legaré, P. Bernhardt, C. Leuvrey, G. Rogez, Hydrothermal Synthesis of Monodisperse Magnetite Nanoparticles, Chemistry of Materials. American Chemical Society, 2006, p. 4399.

[130] S. Ge, X. Shi, K. Sun, C. Li, C. Uher, J.R. Baker, M.M. Banaszak Holl, B.G. Orr, The Journal of Physical Chemistry C 113 (2009) 13593.

[131] A.B. Chin, I.I. Yaacob, Journal of Materials Processing Technology 191 (2007) 235.

[132] E. Cheraghipour, S. Javadpour, A.R. Mehdizadeh, Journal of Biomedical Science and Engineering Vol.05No.12 (2012) 5.

[133] D.F. Coral, P. Mendoza Zélis, M. Marciello, M.d.P. Morales, A. Craievich, F.H. Sánchez, M.B. Fernández van Raap, Langmuir 32 (2016) 1201.

[134] L.C. Branquinho, M.S. Carrião, A.S. Costa, N. Zufelato, M.H. Sousa, R. Miotto, R. Ivkov, A.F. Bakuzis, Scientific Reports 3 (2013) 2887.

[135] G.T. Landi, Physical Review B 89 (2014) 014403.

[136] M.E. Sadat, R. Patel, J. Sookoor, S.L. Bud'ko, R.C. Ewing, J. Zhang, H. Xu, Y. Wang, G.M. Pauletti, D.B. Mast, D. Shi, Materials Science and Engineering: C 42 (2014) 52.

[137] H. Nemala, J.S. Thakur, V.M. Naik, P.P. Vaishnava, G. Lawes, R. Naik, Journal of Applied Physics 116 (2014) 034309.

[138] M. Jamet, W. Wernsdorfer, C. Thirion, D. Mailly, V. Dupuis, P. Mélinon, A. Pérez, Physical Review Letters 86 (2001) 4676.

[139] C.-R. Lin, Y.-M. Chu, S.-C. Wang, Materials Letters 60 (2006) 447.

[140] M. Respaud, J.M. Broto, H. Rakoto, A.R. Fert, L. Thomas, B. Barbara, M. Verelst, E. Snoeck, P. Lecante, A. Mosset, J. Osuna, T.O. Ely, C. Amiens, B. Chaudret, Physical Review B 57 (1998) 2925.

[141] R. Thomas, I.-K. Park, Y. Jeong, International Journal of Molecular Sciences 14 (2013) 15910.

[142] H. Shokrollahi, Materials Science and Engineering: C 33 (2013) 4485.

[143] P. Caravan, J.J. Ellison, T.J. McMurry, R.B. Lauffer, Chemical Reviews 99 (1999) 2293.

[144] Y.-w. Jun, J.-s. Choi, J. Cheon, Chemical Communications (2007) 1203.

[145] N. Arsalani, H. Fattahi, M. Nazarpoor, Express Polym Lett 4 (2010) 329.

[146] D. Kim, Y. Zhang, J. Kehr, T. Klason, B. Bjelke, M. Muhammed, Journal of Magnetism and Magnetic Materials 225 (2001) 256.

[147] F. Hu, L. Wei, Z. Zhou, Y. Ran, Z. Li, M. Gao, Advanced Materials 18 (2006) 2553.

[148] Y.-w. Jun, Y.-M. Huh, J.-s. Choi, J.-H. Lee, H.-T. Song, KimKim, S. Yoon, K.-S. Kim, J.-S. Shin, J.-S. Suh, J. Cheon, Journal of the American Chemical Society 127 (2005) 5732.

[149] M. De, S.S. Chou, H.M. Joshi, V.P. Dravid, Advanced Drug Delivery Reviews 63 (2011) 1282.

[150] T.-H. Shin, Y. Choi, S. Kim, J. Cheon, Chemical Society Reviews 44 (2015) 4501.

[151] K.H. Bae, Y.B. Kim, Y. Lee, J. Hwang, H. Park, T.G. Park, Bioconjugate Chemistry 21 (2010) 505.

[152] S. Santra, S.D. Jativa, C. Kaittanis, G. Normand, J. Grimm, J.M. Perez, ACS nano 6 (2012) 7281.

[153] Z. Zhou, D. Huang, J. Bao, Q. Chen, G. Liu, Z. Chen, X. Chen, J. Gao, Advanced Materials 24 (2012) 6223.

[154] N. Xiao, W. Gu, H. Wang, Y. Deng, X. Shi, L. Ye, Journal of Colloid and Interface Science 417 (2014) 159.

[155] I. Hilger, W.A. Kaiser, Nanomedicine 7 (2012) 1443.

[156] R.M. Bozorth, H.J. Williams, D.E. Walsh, Physical Review 103 (1956) 572.

[157] G. Litsardakis, I. Manolakis, K. Efthimiadis, Journal of Alloys and Compounds 427 (2007) 194.

[158] R.N. Panda, J.C. Shih, T.S. Chin, Journal of Magnetism and Magnetic Materials 257 (2003) 79.

[159] P.-S. Jiang, P. Drake, H.-J. Cho, C.-H. Kao, K.-F. Lee, C.-H. Kuo, X.-Z. Lin, Y.-J. Lin, Journal of Nanoscience and Nanotechnology 12 (2012) 5076.

[160] P. Drake, H.-J. Cho, P.-S. Shih, C.-H. Kao, K.-F. Lee, C.-H. Kuo, X.-Z. Lin, Y.-J. Lin, Journal of Materials Chemistry 17 (2007) 4914.

[161] Y.I. Kim, W.B. Im, M.K. Jeon, Y.H. Lee, K.B. Kim, K.S. Ryul, J Nanosci Nanotechnol 11 (2011) 810.

[162] J. Peng, M. Hojamberdiev, Y. Xu, B. Cao, J. Wang, H. Wu, Journal of Magnetism and Magnetic Materials 323 (2011) 133.

[163] F. Alexis, E. Pridgen, L.K. Molnar, O.C. Farokhzad, Molecular Pharmaceutics 5 (2008) 505.

[164] K. Knop, R. Hoogenboom, D. Fischer, U.S. Schubert, Angewandte Chemie International Edition 49 (2010) 6288.

[165] M. Filippousi, M. Angelakeris, M. Katsikini, E. Paloura, I. Efthimiopoulos, Y. Wang, D. Zamboulis, G. Van Tendeloo, The Journal of Physical Chemistry C 118 (2014) 16209.

[166] T. Marín, P. Montoya, O. Arnache, J. Calderón, The Journal of Physical Chemistry B (2016).

[167] P.I.P. Soares, A.M.R. Alves, L.C.J. Pereira, J.T. Coutinho, I.M.M. Ferreira, C.M.M. Novo, J.P.M.R. Borges, Journal of Colloid and Interface Science 419 (2014) 46.

[168] Y. Yuan, D. Rende, C.L. Altan, S. Bucak, R. Ozisik, D.-A. Borca-Tasciuc, Langmuir 28 (2012) 13051.

[169] J. Salafranca, J. Gazquez, N. Pérez, A. Labarta, S.T. Pantelides, S.J. Pennycook, X. Batlle, M. Varela, Nano Letters 12 (2012) 2499.

[170] X.L. Liu, H.M. Fan, J.B. Yi, Y. Yang, E.S.G. Choo, J.M. Xue, D.D. Fan, J. Ding, Journal of Materials Chemistry 22 (2012) 8235.

[171] F. Mohammad, G. Balaji, A. Weber, R.M. Uppu, C.S.S.R. Kumar, The Journal of Physical Chemistry C 114 (2010) 19194.

[172] E. Peng, J. Ding, J.M. Xue, New Journal of Chemistry 38 (2014) 2312.

[173] A.A.M. Elsherbini, A. El-Shahawy, Journal of Nanomaterials 2013 (2013) 6.

[174] K.D. Bakoglidis, K. Simeonidis, D. Sakellari, G. Stefanou, M. Angelakeris, IEEE Transactions on Magnetics 48 (2012) 1320.

[175] T. Cedervall, I. Lynch, S. Lindman, T. Berggård, E. Thulin, H. Nilsson, K.A. Dawson, S. Linse, Proceedings of the National Academy of Sciences 104 (2007) 2050.

[176] J. Klein, Proceedings of the National Academy of Sciences of the United States of America 104 (2007) 2029.

[177] S.L. Hirsh, D.R. McKenzie, N.J. Nosworthy, J.A. Denman, O.U. Sezerman, M.M.M. Bilek, Colloids and Surfaces B: Biointerfaces 103 (2013) 395.

[178] L. Treuel, M. Malissek, J.S. Gebauer, R. Zellner, ChemPhysChem 11 (2010) 3093.

[179] Y.K. Lee, E.-J. Choi, T.J. Webster, S.-H. Kim, D. Khang, International Journal of Nanomedicine 10 (2015) 97.

[180] U. Sakulkhu, M. Mahmoudi, L. Maurizi, J. Salaklang, H. Hofmann, Scientific Reports 4 (2014) 5020.

[181] H.T.R. Wiogo, M. Lim, V. Bulmus, J. Yun, R. Amal, Langmuir 27 (2011) 843.

[182] S. Khan, A. Gupta, C.K. Nandi, The Journal of Physical Chemistry Letters 4 (2013) 3747.

[183] M.P. Calatayud, B. Sanz, V. Raffa, C. Riggio, M.R. Ibarra, G.F. Goya, Biomaterials 35 (2014) 6389.

[184] A.P. Khandhar, R.M. Ferguson, K.M. Krishnan, Journal of Applied Physics 109 (2011) 07B310.

[185] W. Strober, Current Protocols in Immunology, John Wiley & Sons, Inc., 2001.

[186] W. Strober, Current Protocols in Immunology, John Wiley & Sons, Inc., 2001.

[187] B.P. Jena, D.J. Taatjes, NanoCellBiology: Multimodal Imaging in Biology and Medicine, Pan Stanford, 2014.

[188] Y.-M. Huh, Y.-w. Jun, H.-T. Song, S. Kim, J.-s. Choi, J.-H. Lee, S. Yoon, K.-S. Kim, J.-S. Shin, J.-S. Suh, J. Cheon, Journal of the American Chemical Society 127 (2005) 12387.

[189] A. Jordan, P. Wust, H. Fähling, W. John, A. Hinz, R. Felix, International Journal of Hyperthermia 9 (1993) 51.

[190] A.K. Gupta, M. Gupta, Biomaterials 26 (2005) 3995.

[191] A. Petri-Fink, B. Steitz, A. Finka, J. Salaklang, H. Hofmann, European journal of pharmaceutics and biopharmaceutics : official journal of Arbeitsgemeinschaft fur Pharmazeutische Verfahrenstechnik e.V 68 (2008) 129.

[192] B. Ankamwar, T.C. Lai, J.H. Huang, R.S. Liu, M. Hsiao, C.H. Chen, Y.K. Hwu, Nanotechnology 21 (2010) 75102.

[193] J. Gao, H. Gu, B. Xu, Accounts of chemical research 42 (2009) 1097.

[194] P. Tartaj, M.d.P. Morales, S. Veintemillas-Verdaguer, T. González-Carreño, C.J. Serna, Journal of Physics D: Applied Physics 36 (2003) R182.

[195] W. Wu, Q. He, C. Jiang, Nanoscale Research Letters 3 (2008) 397.

[196] H.A. Jeng, J. Swanson, Journal of environmental science and health. Part A, Toxic/hazardous substances & environmental engineering 41 (2006) 2699.

[197] H.L. Karlsson, J. Gustafsson, P. Cronholm, L. Moller, Toxicology letters 188 (2009) 112.

[198] N. Lewinski, V. Colvin, R. Drezek, Small 4 (2008) 26.

[199] D.H. Han, J.P. Wang, H.L. Luo, Journal of Magnetism and Magnetic Materials 136 (1994) 176.

[200] P. Wunderbaldinger, L. Josephson, R. Weissleder, Bioconjugate Chemistry 13 (2002) 264.

[201] B. Ankamwar, T.C. Lai, J.H. Huang, R.S. Liu, M. Hsiao, C.H. Chen, Y.K. Hwu, Nanotechnology 21 (2010) 075102.

[202] M.E. Davis, D.M. Shin, Nature reviews Drug discovery 7 (2008) 771.

[203] B.D. Chithrani, A.A. Ghazani, W.C. Chan, Nano letters 6 (2006) 662.

[204] X. Huang, I.H. El-Sayed, W. Qian, M.A. El-Sayed, Journal of the American Chemical Society 128 (2006) 2115.

[205] R. Foldbjerg, D.A. Dang, H. Autrup, Archives of toxicology 85 (2011) 743.

[206] M. Jeyaraj, G. Sathishkumar, G. Sivanandhan, D. MubarakAli, M. Rajesh, R. Arun, G. Kapildev, M. Manickavasagam, N. Thajuddin, K. Premkumar, Colloids and surfaces B: Biointerfaces 106 (2013) 86.

[207] Q.A. Pankhurst, J. Connolly, S. Jones, J. Dobson, Journal of physics D: Applied physics 36 (2003) R167.

[208] A. Verma, F. Stellacci, Small 6 (2010) 12.

[209] D.H.M. Dam, J.H. Lee, P.N. Sisco, D.T. Co, M. Zhang, M.R. Wasielewski, T.W. Odom, ACS nano 6 (2012) 3318.

[210] O. Veiseh, J.W. Gunn, M. Zhang, Advanced drug delivery reviews 62 (2010) 284.

[211] H. Jin, K.A. Kang, Oxygen Transport to Tissue Xxviii, Springer, 2008, p. 45.

[212] A. Petri-Fink, M. Chastellain, L. Juillerat-Jeanneret, A. Ferrari, H. Hofmann, Biomaterials 26 (2005) 2685.

[213] D.L. Thorek, A.K. Chen, J. Czupryna, A. Tsourkas, Annals of biomedical engineering 34 (2006) 23.

[214] X.-H. Peng, X. Qian, H. Mao, A.Y. Wang, Z. Chen, S. Nie, D.M. Shin, Int J nanomedicine 3 (2008) 311.

[215] C.C. Berry, A.S. Curtis, Journal of physics D: Applied physics 36 (2003) R198.

[216] F.-H. Chen, L.-M. Zhang, Q.-T. Chen, Y. Zhang, Z.-J. Zhang, Chem. Commun. 46 (2010) 8633.

[217] S. Nigam, S. Chandra, D.F. Newgreen, D. Bahadur, Q. Chen, Langmuir 30 (2014) 1004.

[218] A. Akbarzadeh, M. Samiei, S.W. Joo, M. Anzaby, Y. Hanifehpour, H.T. Nasrabadi, S. Davaran, J Nanobiotechnology 10 (2012) 46.

[219] R.L. Siegel, K.D. Miller, A. Jemal, CA: A Cancer Journal for Clinicians 65 (2015) 5.

[220] I. Brigger, C. Dubernet, P. Couvreur, Advanced drug delivery reviews 64 (2012) 24.

[221] The Journal of General Physiology 78 (1981) 349.

[222] S. Dash, P.N. Murthy, L. Nath, P. Chowdhury, Acta Pol Pharm 67 (2010) 217.

[223] N. Oh, J.-H. Park, International Journal of Nanomedicine 9 (2014) 51.

[224] H.C. Arora, M.P. Jensen, Y. Yuan, A. Wu, S. Vogt, T. Paunesku, G.E. Woloschak, Cancer Research 72 (2012) 769.

[225] F.J. Douglas, D.A. MacLaren, N. Maclean, I. Andreu, F.J. Kettles, F. Tuna, C.C. Berry, M. Castro, M. Murrie, RSC Advances 6 (2016) 74500.

[226] X. Cheng, X. Tian, A. Wu, J. Li, J. Tian, Y. Chong, Z. Chai, Y. Zhao, C. Chen, C. Ge, ACS Applied Materials & Interfaces 7 (2015) 20568.

[227] M. Safi, J. Courtois, M. Seigneuret, H. Conjeaud, J.-F. Berret, Biomaterials 32 (2011) 9353.

[228] M. Catalayud, B. Sanz, V. Raffa, C. Riggio, M. Ibarra, G. Goya, arXiv preprint arXiv:1403.3889 (2014).

ABSTRACT

Fe_3O_4 NANOPARTICLES FOR MAGNETIC HYPERTHERMIA AND DRUG DELIVERY; SYNTHESIS, CHARACTERIZATION AND CELLULAR STUDIES

by

MAHESHIKA PALIHAWADANA ARACHCHIGE

August 2016

Advisors: Drs. Ratna Naik and Bhanu P. Jena

Major: Physics (Condensed Matter)

Degree: Doctor of Philosophy

In recent years, magnetic nanoparticles (MNPs), especially superparamagnetic Fe_3O_4nanoparticles, have attracted a great deal of attention because of their potential applications in biomedicine. Among the other applications, Magnetic hyperthermia (MHT), where localized heating is generated by means of relaxation processes in MNPs when subjected to a radio frequency magnetic field, has a great potential as a non-invasive cancer therapy treatment. Specific absorption rate (SAR), which measures the efficiency of heat generation, depends on magnetic properties of the particles such as saturation magnetization (M_s), magnetic anisotropy (K), particle size distribution, magnetic dipolar interactions, and the rheological properties of the target medium.We have investigated MHT in two Fe_3O_4 ferrofluids prepared by co-precipitation (CP) and hydrothermal (HT) synthesis methods showing similar physical particle size distribution and M_s, but very different SAR ~ 110 W/g and ~ 40 W/g at room temperature. This observed reduction in SAR has been explained by taking the dipolar interactions into account using the so called *T** model. Our analysis reveals that HT ferrofluid shows an order of magnitude higher effective dipolar interaction and a wider distribution of magnetic core size of MNPs compared to that of CP ferrofluid.

We have studied dextran coated Gd-doped Fe_3O_4 nanoparticles as a potential candidate in theronostics for multimodal contrast imaging and cancer treatment by hyperthermia. The effect of surfactant on the MHT efficiency and cytotoxicity on human pancreatic cancer cells was explored as well. Though further in vivo study is necessary in the future, these results imply that the dextran coated Fe_3O_4 dispersion could maintain their high heating capacity in physiological environments while citric acid coating require further surface modification to reduce the non-specific protein adsorption. We have also investigated the traffic, distribution, and cytotoxicity, associated with dextran functionalized FITC conjugated Fe_3O_4 nanoparticles, and our results demonstrate that there is a time-dependent distribution of these nanoparticles into different cellular compartments. Moreover, a novel conjugation of anti-cancer drug, Doxorubicin (Dox) with a labeling dye (FITC) onto dextran coated Fe_3O_4 nanoparticles was developed using existing EDC/NHS technique for specific drug targeting. The experiments on this unique drug-dye dual conjugation with human pancreatic cancer cell line (MIA PaCa-2) show that association of Dox onto the surface of nanoparticles enhances its penetration into the cancer cells as compared to the unconjugated drug while releasing Dox into the nucleus of the malignant cells.

AUTOBIOGRAPHICAL STATEMENT

EDUCATION

• Ph.D. (Physics), Wayne State University, August 2016
• M.Sc. (Physics), Wayne State University, May 2011
• B.Sc. (Honors) in Physics, University of Peradeniya, Sri Lanka, August 2008

AWARDS

- Summer Dissertation Fellowship, Wayne State University: Spring/Summer 2016.
- Knoller Physics Fellowship, Department of Physics, Wayne State University: 2014/15
- Excellent poster presentation awards: 2014 and 2015 Physics Graduate Research Day, Wayne State University

PROFESSIONAL EXPERIENCE

- Graduate Teaching Assistant: 2009 –2011, 2015-2016, Department of Physics and Astronomy, Wayne State University
- Graduate Research Assistant: 2011-2014, Department of Physics and Astronomy, Wayne State University

PUBLICATIONS

1. He Xie, Yu-Chung N. Cheng, Paul Kokeny, Saifeng Liu, Ching-Yi Hsieh, E. Mark Haacke, **Maheshika Palihawadana Arachchige**, Gavin Lawes; "A quantitative study of susceptibility and additional frequency shift of three common materials in MRI." Magnetic resonance in medicine, 2015 Oct 31. doi: 10.1002/mrm.26035
2. Hitihami-Mudiyanselage, A.; **Arachchige, M. P**.; Seda, T.; Lawes, G.; Brock, S. "Synthesis and Characterization of Discrete FexNi2-xP Nanocrystals ($0 < x < 2$): Compositional Effects on Magnetic Properties". Chem. Mater. 2015, 27, 6592−6600.
3. Li, Da, **Maheshika P. Arachchige**, Bogdan Kulikowski, Gavin Lawes, Takele Seda, and Stephanie L. Brock; "Control of Composition and Size in Discrete CoxFe2-xP Nanoparticles: Consequences for Magnetic Properties", Chemistry of Materials Article ASAP (2016),**DOI:** 10.1021/acs.chemmater.6b01185
4. **Maheshika P.Aracchchige,** Humeshkar Nemala, Vaman Naik, Ratna Naik; "Effect of dipolar interactions on temperature dependent magnetic hyperthermia in ferrofluids" (Submitted to Journal of Applied Physics***)***
5. **Maheshika P.Aracchchige**, Suvra S. Laha, Akshata Naik, Ratna Naik, Gavin Lawes, Bhanu P. Jena; "Functionalized Superparamagnetic iron oxide nanoparticles potentiate cellular entry and release of cancer Drug" (Manuscript ready for submission)
6. **Maheshika P. Aracchchige**, Xuequn Chen, Ratna Naik, Gavin Lawes, Bhanu P. Jena; "Exposure of Dextran-Coated Superparamagnetic Iron Oxide Nanoparticles Demonstrates Specific Time-Dependent Interactions with Proteins in Human Pancreatic Cancer Cells" (manuscript under preparation)
7. **Maheshika P.Aracchchige,** Vaman Naik, Ratna Naik; "Gd doped Fe_3O_4 nanoparticles for magnetic hyperthermia"(manuscript under preparation***)***